https://ntrs.nasa.gov/search.jsp?R=19880007636 2020-03-20T07:35:35+00:00Z

NASA Contractor Report 4119

AlGaAs Heterojunction Lasers

B. Goldstein, G. N. Pultz, D. B. Carlin,
S. E. Slavin, and M. Ettenberg

CONTRACT NAS1-17441
FEBRUARY 1988

(NASA-CR-4119) AlGaAs HETEROJUNCTION LASERS Final Report, 28 Jun. 1985 - 27 Jun. 1986 (RCA Labs.) 157 p CSCL 20E

N88-17020

Unclas
H1/36 0123009

NASA Contractor Report 4119

AlGaAs Heterojunction Lasers

B. Goldstein, G. N. Pultz, D. B. Carlin,
S. E. Slavin, and M. Ettenberg
RCA Laboratories
Princeton, New Jersey

Prepared for
Langley Research Center
under Contract NAS1-17441

National Aeronautics
and Space Administration

Scientific and Technical
Information Division

1988

PREFACE

This report describes work performed from 28 June 1985 to 27 June 1986 at RCA Laboratories in the Opto-electronics Laboratory, B. Hershenov, Director, under Contract No. NAS1-17441. M. Ettenberg was the Project Supervisor, and D.B. Carlin, G.N. Pultz, and B. Goldstein were Project Scientists. Other contributors to this research were J.K. Butler, G.A. Evans, N.A. Dinkel, F.R. Elia, M.G. Harvey, D.B. Gilbert, T.R. Stewart, J.J. Hughes, E. DePiano, D.P. Marinelli, D.T. Tarangioli, N.W. Carlson, D.J. Channin, V.J. Masin, S.E. Slavin, F.Z. Hawrylo, and A.R. Dholakia.

PRECEDING PAGE BLANK NOT FILMED

TABLE OF CONTENTS

PRECEDING PAGE BLANK NOT FILMED PAGE IV INTENTIONALLY BLANK

LIST OF ILLUSTRATIONS

LIST OF ILLUSTRATIONS

LIST OF ILLUSTRATIONS

SUMMARY

The characterization of 8300 Å lasers has been considerably broadened, especially in the area of beam quality, and results continue to fulfill our previously held high expectations. Modulation rates up to 2 Gbit/s at output powers of 20 mW were observed, waveform fidelity was fully adequate for low BER data transmission, and wavefront measurements showed that phase aberrations were less than $\lambda/50$.

Individually addressable arrays of up to ten contiguous diode lasers have been fabricated and tested. The individual lasers operate at powers up to 30 mW cw in single spatial mode and with a sufficiently narrow band of frequencies for recording and erasing purposes. The far-field beams have FWHMs $\approx 8.5°$ laterally and $\approx 30°$ perpendicularly, are non-astigmatic with wavefront aberrations less than $\approx \lambda/40$, and have modulation performance that satisfactorily follows a 2 GHz clock. Finally, we have developed a suitable metallized BeO submount and testing fixture that holds the arrays for automated probe testing of the relevant opto-electronic properties.

Shifting the operating wavelength of our basic CSP laser from 8300 Å to 8650 Å posed no special problems and was accomplished chiefly by the addition of Si to the active region after design inputs from our theoretical modeling effort. Output power has reached 100 mW single mode, with excellent far-field wave-front properties. Operating life is currently $\approx$ 1000 hours at 35 mW cw.

Laser reliability, for operation at both 8300 Å and 8650 Å, has profited significantly from several developments in our processing procedures. These include in situ low-energy ion-bombardment cleaning of mirror facets just prior to coating, improvements in photolithography techniques that decrease pinhole density in our SiO_2 films and laser surfaces, changing our Zn diffusion to prevent Zn contamination of our active layers, and instituting machine-assisted-die-bonding techniques for laser mounting. In addition, failure diagnosis has been developed which includes metallurgical examination, TEM microscopy, and cathodoluminescence. A lifetesting plan has been initiated that includes a set of criteria to be used in a pre-screening schedule.

SUMMARY (cont'd)

HIGHLIGHTS

8300 Å HIGH-POWER SINGLE-MODE LASER

- Modulation to 2 GHz.
- Wavefront abberation $<\lambda/25$ at >100 mW.
- 20,000 hours at 20 mW cw operation.
- 10-Diode individually addressed array with each diode at 30 mW cw.
- Probe testing for arrays.

8650 Å HIGH-POWER SINGLE-MODE LASER

- 100 mW single-mode operation.
- Single-mode operation at 35 mW cw.
- cw operation to 900 hours.
- Improved processing including facet mirror ion cleaning.

I. INTRODUCTION

The work described in the previous Annual Report [1] centered on the development of individual high power diode lasers operating at 8300 Å for potential use in areas such as space communications, optical recording and storage, and local area optical communication networks. Excellent progress was reported in growth and characterization techniques that culminated in our ability to reproducibly fabricate single-mode lasers in the 25-50 mW cw range (and occasionally higher) with beam qualities more than adequate for such applications.

This report describes the research and development efforts that have carried these results to the next logical steps, i.e., their application to specific areas of optical recording and intersatellite communications and a reliability assessment and improvement program. The areas that have received most attention during this past year are: (1) individually addressed arrays for optical recording, (2) the expansion of fundamental diode laser work to include operation at 8650 Å -- both using the CSP laser as basic structure -- and (3) the development of reliability and life testing programs shaped by the NASA Advanced Communications Test Satellite (ACTS) Program requirements [2].

II. LASER PERFORMANCE AT 8300 Å

We have considerably broadened our evaluation and characterization of high power 8300-Å single-spatial-mode lasers. Excellent operational properties have been measured in the areas of high data-rate modulation, phase-front quality, reliability and life. In addition, significant advances in theoretical modeling and analysis have been recorded.

For reference purposes, we begin with a schematic diagram of the basic CSP laser structure together with profiles of some of the relevant waveguiding parameters in Fig. 1(a), and typical optoelectronic performance at 50 mW cw (yields ≈ 5%-15%) in Fig. 1(b).

A. HIGH DATA RATE MODULATION

One of the most important properties of a laser used in either space communications or optical recording is its ability to handle information at high data rates, especially at high power. The digital modulation characteristics of CSP lasers developed during this program were measured and evaluated, and the devices showed excellent performance for the applications mentioned.

Modulation rates up to 2 Gbits/s at output powers of 20 mW were observed (with power being limited only by the current capabilities of the drive circuit.) At 1 Gbit/s (Fig. 2b), the modulated power was as high as 60 mW. In both cases, waveform fidelity was fully adequate for low BER data transmission in optical links, as indicated in the figure. Note especially the absence of significant tailing and ringing (Figs. 2d-f) in response to the square wave input typified by that shown in Fig. 2c. We attribute the excellent modulation performance of these lasers to design features that were incorporated after extensive experimental and theoretical studies of the high frequency characteristics of our high power laser structures.

To the best of our knowledge, these results represent the highest power bandwidth product demonstrated for any laser diode to date. These modulation studies revealed that lateral carrier diffusion in the active layer was the source of serious degradation in digital waveform fidelity of earlier device types (CDH-LOCs and early CSPs) at data rates above 500 Mbits/s. Computer simulation of the pulse response of these devices showed that carrier diffusion depended on the degree of confinement of injected current to the lateral

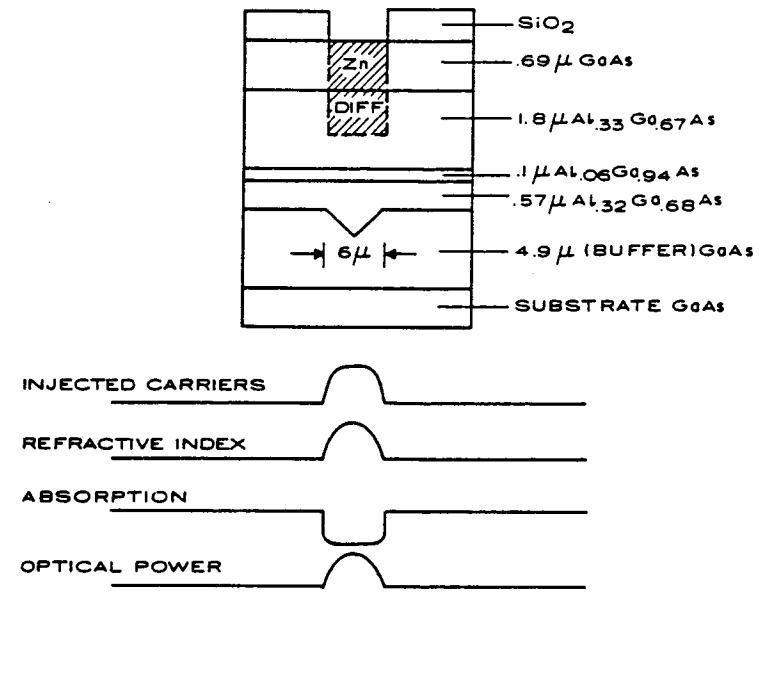

(a)

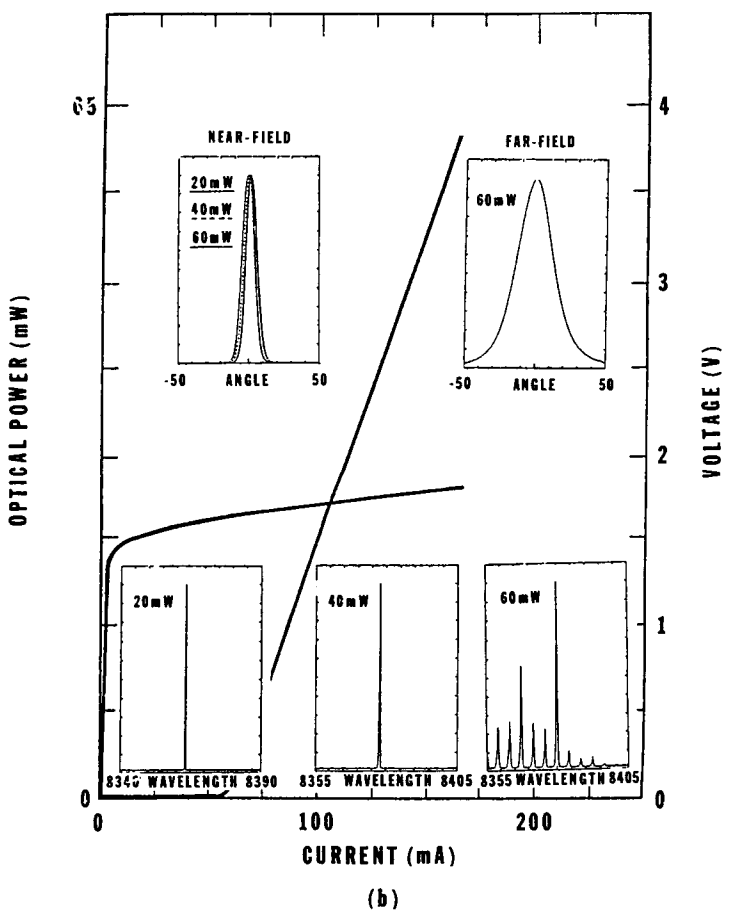

(b)

Figure 1. (a) Basic CSP laser structure. Note the Zn diffusion for current confinement, and the dielectric profiles that determine the waveguiding. (b) Typical optoelectronic performance at 50 mW cw. (Yield ≈ 5%-15%).

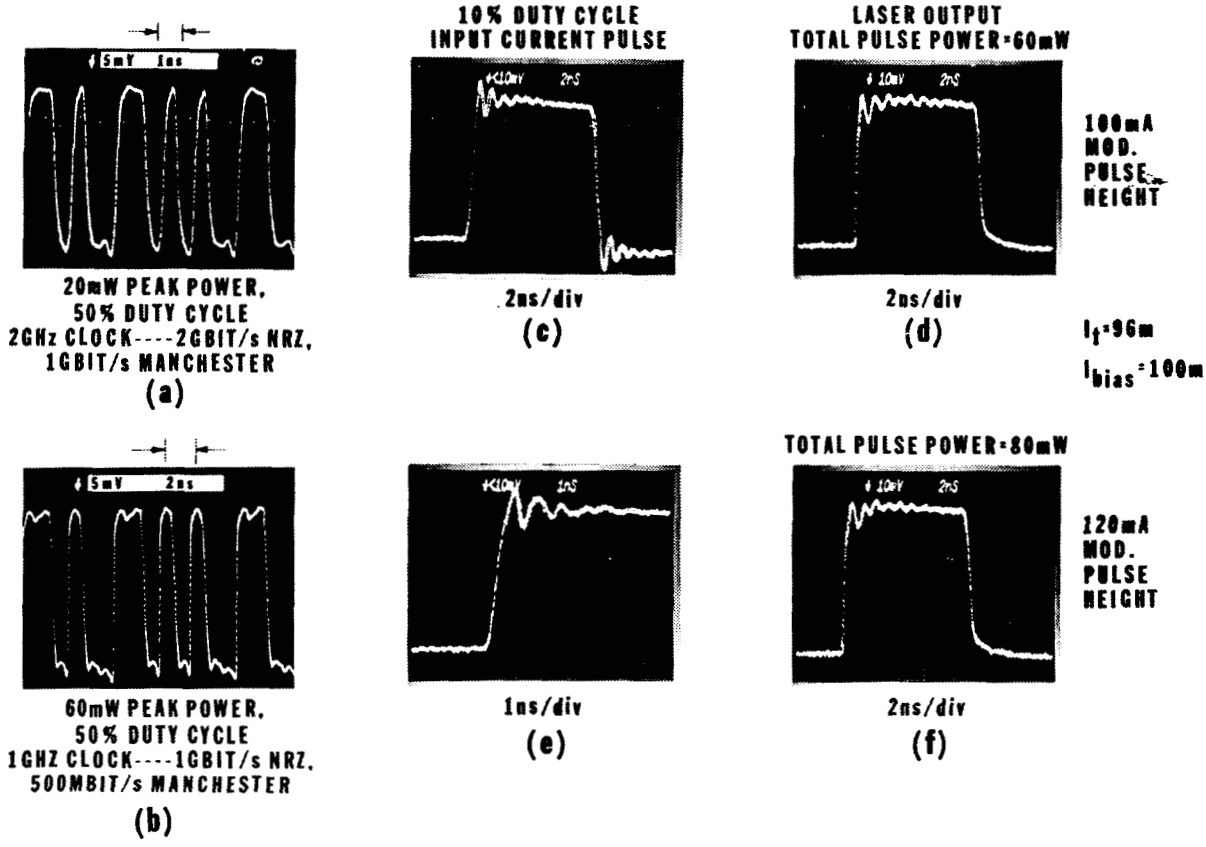

Figure 2. The modulation response of a CSP laser showing: laser output of pseudo-random bit trains at 20 mW peak power at 2 Gbits/s NRZ (a) and 60 mW peak power at 1 Gbit/s NRZ (b); typical electrical input waveworms used for these studies (c); and laser output response at 60 mW (d) and 80 mW (e and f) peak power.

dimensions of the optical mode. This problem was solved by careful tailoring of the injection current distribution through the use of diffused-Zn current confinement contacts as shown in Fig. 1a. The new devices produced in the present program show excellent agreement between theoretically predicted and observed pulse response, and have correspondingly improved digital modulation characteristics, especially at their current high levels.

B. WAVE-FRONT PROPERTIES

Phase aberrations in the laser output cause a reduction in the on-axis intensity of a refocused spot or the far-field pattern, and thus will have a significant detrimental effect on a diffraction limited optical system, such as

ORIGINAL PAGE IS
OF POOR QUALITY

intersatellite communications and optical recording. Phase aberrations of laser wave fronts occur primarily because of the gain-guiding effect of the injected carriers which usually gives rise to an astigmatic wave-front. Therefore strongly index-guided diode lasers are very much preferred for diffraction-limited systems.

The CSP laser structure is one that can provide sufficiently strong index guiding to overcome the effects of gain guiding. This has been confirmed by measuring the far-field phase aberrations of many CSP lasers (and some gain-guided lasers) under a variety of operating conditions. Figure 3(a) shows perspective plots of the measured phase aberrations of a CSP laser output under both pulsed and CW conditions up to 90 mW output power. The axes indicate directions parallel and perpendicular to the p/n junction, while the variation in the phase front are indicated by the heights of the mesas. Clearly, the wave fronts show very little aberration, $\approx \lambda/25$, and, equally important, they do not change significantly with power output.

To more graphically illustrate the wave-front behavior between our CSP lasers and gain-guided lasers, Fig. 3(b) shows the phase aberrations of two types of Spectra Diode Laboratories gain-guided lasers which have aberrations 5 to 10 times larger than those found in Fig. 3(a), especially at high power. Included also in Fig. 3(b) is a typical example of Hitachi's commercially available CSP laser. Again, to our knowledge, these are the first careful measurements of the wavefront quality of laser diode sources and confirm for the first time the fact that at least for our high-power CSP lasers, the wavefront quality is as good as, if not better than, the available optics for optical recording.

C. ADVANCES IN DEVICE MODELING

Figure 4 shows the basic elements of theoretical laser simulation [3]. Starting with the basic laser structure (Fig.1), the various "building blocks" of laser operation are sequentially incorporated into the modeling. The crucial iterations at the "Error satisfied" and "Threshold satisfied" points are performed until self-consistency is attained within the error limits imposed.

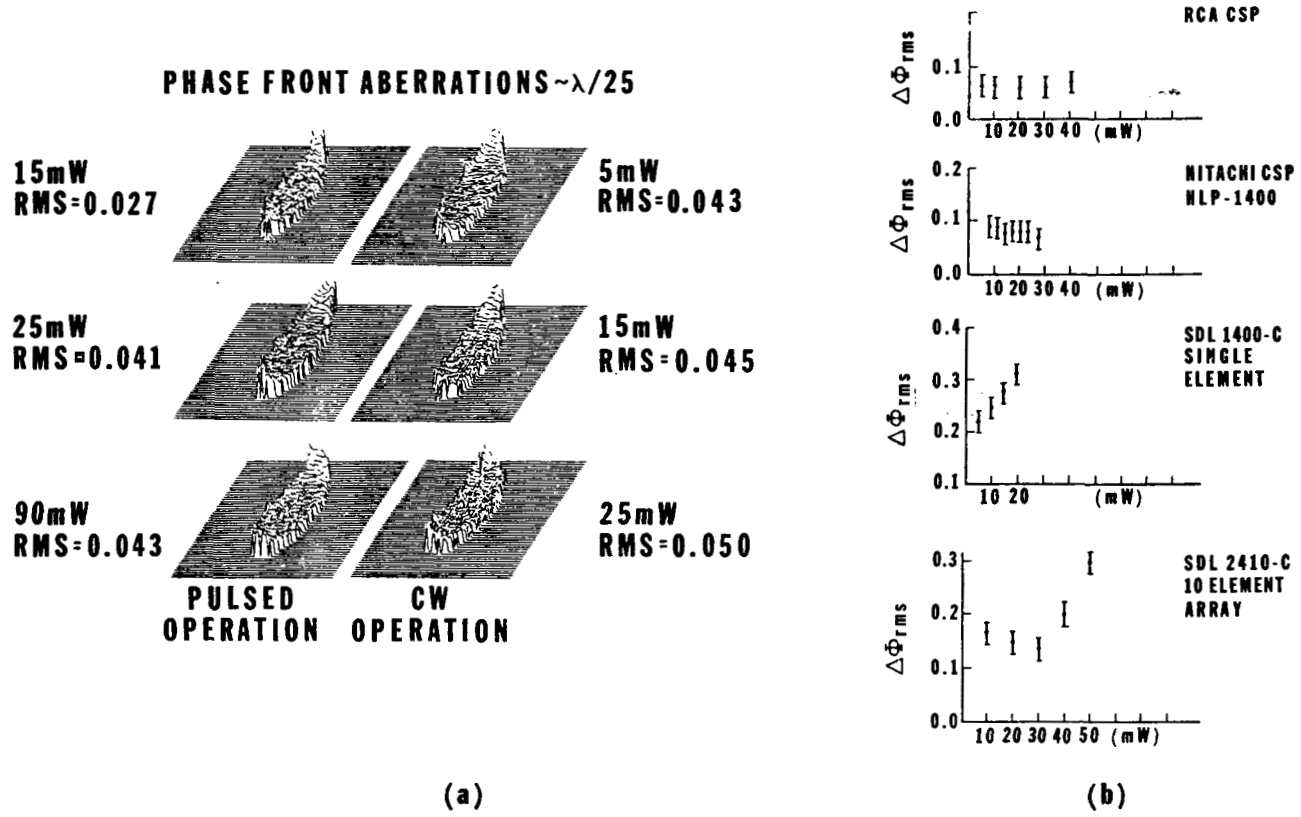

Figure 3. Experimental phase front measurement using a LADITE [11,12] interferometer showing the aberrations in the output of a CSP diode laser under pulsed (left) and cw (right) operating conditions. The rms aberrations for each output power measured are shown next to the corresponding data. (b) The rms phase front aberrations of CSP lasers from RCA and Hitachi and gain-guided lasers and arrays plotted as a function of output power.

In the previous Annual Report [1] the effect of channel asymmetry on laser characteristics was discussed. In our current modeling, perhaps the two most significant findings center on the injected current profile. In the first of these, the spreading of the injected current profile reaching the active layer was calculated as a function of the Zn diffusion depth and Zn stripe width. The results are shown in Fig. 5 in the form of a set of normalized injected current profiles for a 4-μ wide Zn stripe.

The distance of the Zn diffusion front from the active region (in microns) is given on the curve, where it can be seen that there is only little difference in the spreading of the injected current whether the diffusion front is 0.5 μ or 0.75 μ from the active layer. (This will have increased significance in the discussion on reliability.) Furthermore, the results are

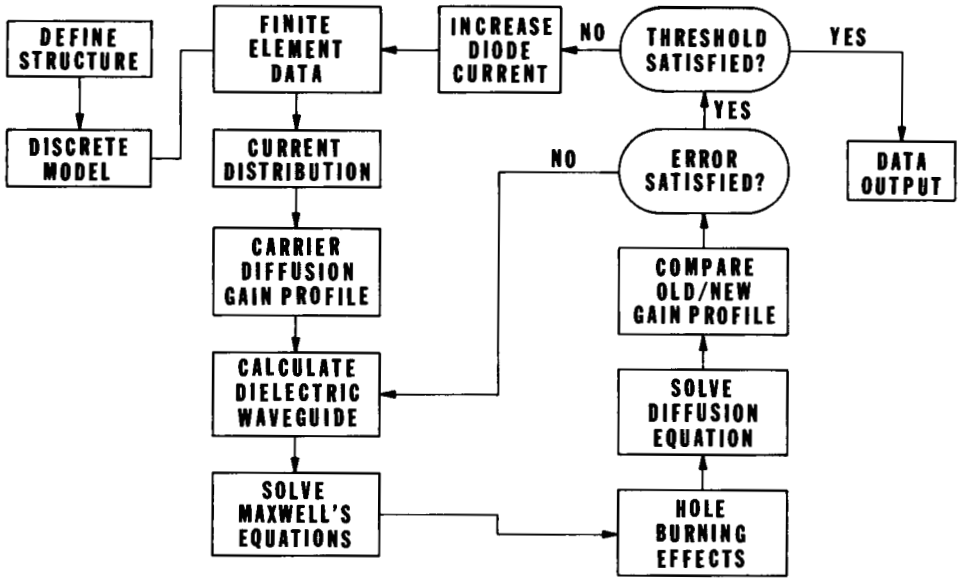

Figure 4. Flow diagram of laser simulation. Modeling proceeds (iterates) until self-consistency is attained.

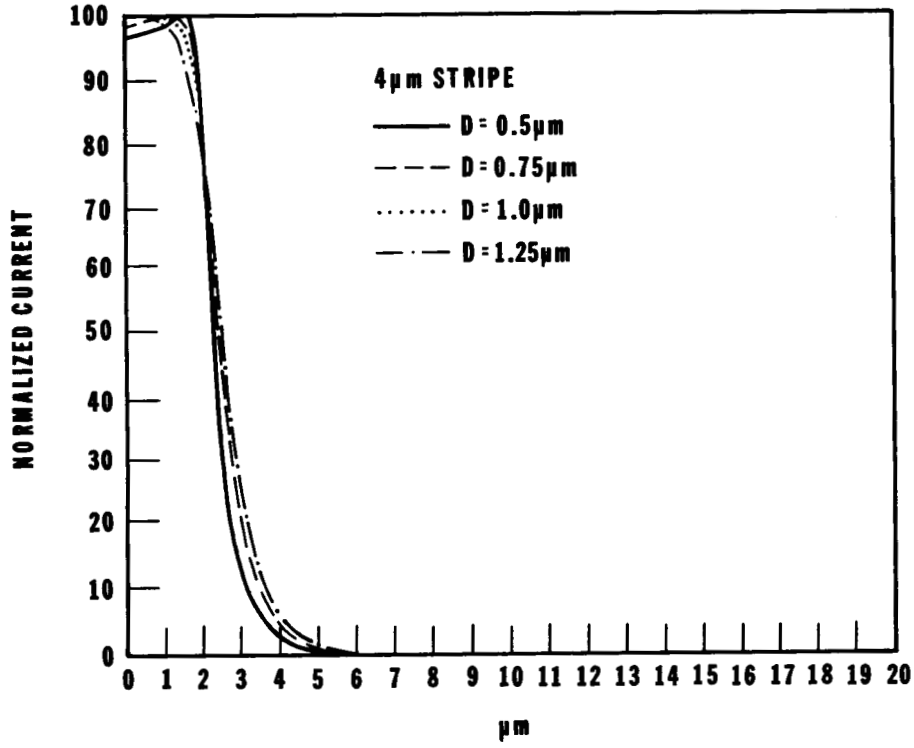

Figure 5. Injection current profiles for a 4-μ wide Zn diffusion whose front is at varying distances from the active layer. Differences between curves are very small.

essentially the same for wider or narrower stripes except that the total width of the diffusion front changes accordingly.

The second result, however, carries with it more worrisome implications. Here, we have calculated the effect of a small misalignment ($\approx 0.5\mu$) between the Zn contact stripe and its substrate channel in an otherwise perfectly symmetrical CSP structure. The results indicate that even this small misalignment can produce profound effects. In Fig. 6 we show the structure and P-I curve (a), the gain curve (b), the index profile (c), and the near-field pattern (d) for a $\approx 0.5\mu$ misalignment of a 5μ-wide Zn stripe as drawn in curve (a).

Note especially the power saturation in (a), the gain peaking 2 μ off-center in (b), and the near field shifting by almost 1 μ in (d). The consequences of this behavior are: (1) the laser would not operate in single mode much over 30-40 mW, (2) there would be serious phase-front distortions, (3) the far-field pattern would shift several degrees, and (4) strongly asymmetric thermal effects would be present in the laser. This work goes far in possibly explaining some of our observations of erratic behavior, and points up the absolute necessity for good structural geometry to achieve high power, good beam quality lasers. This research work will continue to help understand laser behavior and to develop new, more optimized structures that are more insensitive to growth or processing variations.

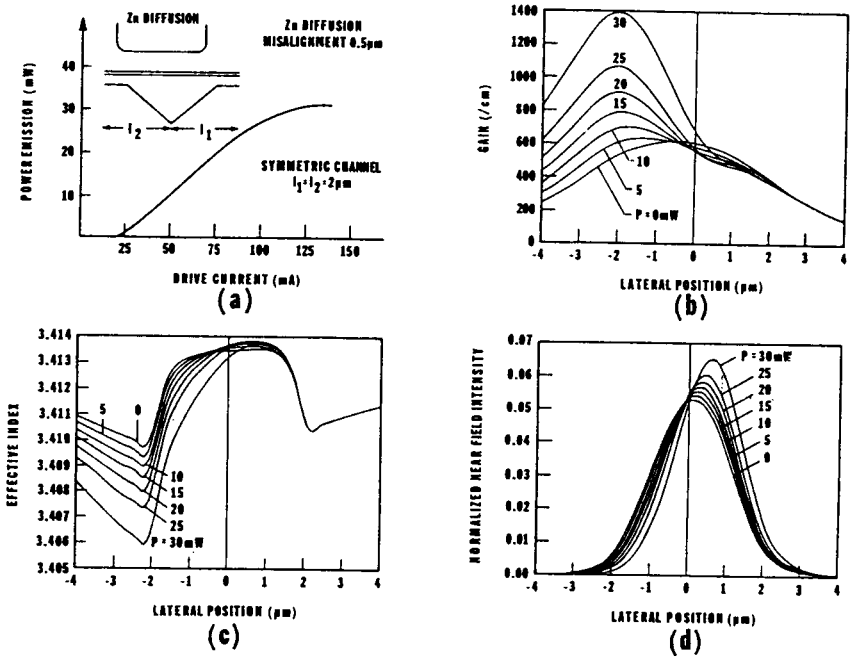

Figure 6. Effects of 0.5 μ misalignment of a 5-μ wide Zn stripe on P-I curve, gain, effective index, and near-field. Note power saturation in curve.

III. INDIVIDUALLY ADDRESSED ARRAYS OF CSP DIODE LASERS

Monolithic arrays of individually addressable high power diode lasers are being developed specifically as sources for multiple channel, high data rate optical memories. The simultaneous storage of independent data streams on multiple, parallel tracks allows commensurately multiplied transfer rates for both data recording and retrieval, a necessary attribute for some high performance systems.

Previously, we have reported three-channel data storage [4] using an array of CDH-LOC (constricted double heterojunction, large optical cavity) devices [5] focused on an archival recording media. These lasers emitted up to 20 mW cw and 40 mw 50% duty cycle in a single spatial mode.

The recent emergence of erasable magneto-optic recording media, however, has imposed additional output power demands on the diode lasers used in recording systems. To achieve complete erasure in a single pass, the laser must emit continuously at roughly the same power as is normally required in a 50% duty-cycle pulsed mode of operation for recording. In addition, many applications under consideration require an increased number of contiguous diode lasers to achieve data transfer rates of hundreds of Mbits/s. We have, therefore, concentrated our recent efforts on arrays of CSP (Channeled Substrate Planar) AlGaAs diode lasers with higher cw output power in a single spatial mode as well as improved device-to-device uniformity (compared to the CDH-LOC device) for use in such high performance multichannel optical recording systems.

This CSP superiority is based on the demonstrable facts that (1) increased output power performance was observed from individual CSP lasers grown by liquid phase epitaxy [6], and (2) the planarity of the CSP structure produced greater growth uniformity and, consequently, a higher yield of contiguous, high performance lasers in the arrays. For optical recording, the most important output power level is that which can be generated in a single fundamental mode. This is the power that can be subsequently focused to a diffraction limited spot on the recording surface. The CSP laser output was more than double that of the CDH-LOC under these conditions. This is particularly important for magneto-optic erasable materials, which impose much greater power demands on the laser for erasure.

A schematic view of a monolithic array on a BeO submount is shown in Fig. 7. The arrays are fabricated by standard multi-bin liquid phase epitaxy techniques as ten-diode units of individual CSP lasers (Fig. 7). Light is generated in

a thin (≈ 800 Å thick) active layer of undoped $Al_{.06}Ga_{.94}As$ sandwiched between cladding layers of p-doped and n-doped $Al_{.33}Ga_{.67}As$, typically 1.8 and 0.5 μm thick, respectively, as indicated in Fig. 8.

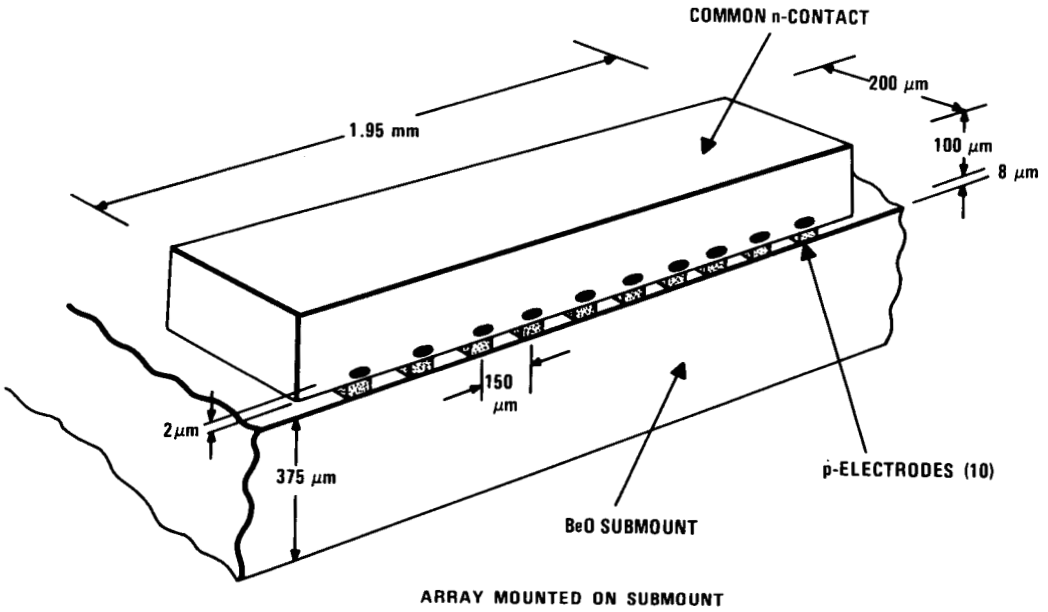

Figure 7. Schematic drawing of a monolithic ten-element array mounted on a metallized beryllia submount.

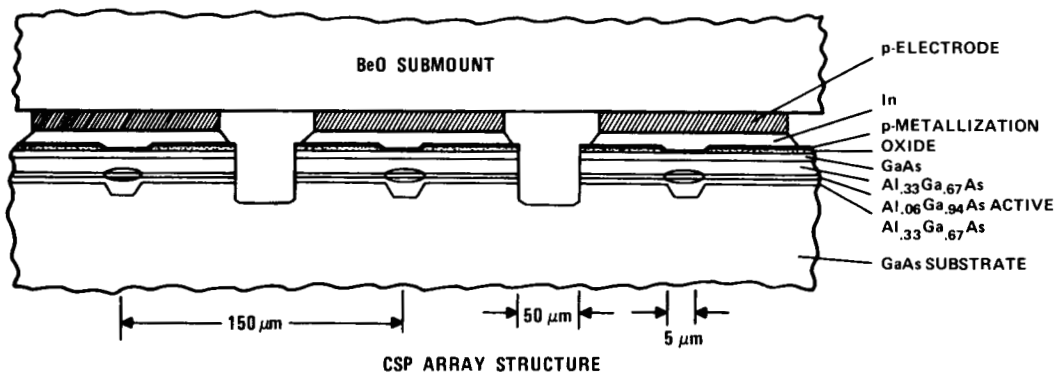

Figure 8. Schematic drawing of three elements of an individually addressable multidiode CSP array bonded to metallized electrodes on a beryllia submount.

The injection current is confined both by a narrow contact stripe in the p-side metallization, defined by openings in an SiO_2 insulation film deposited on the GaAs cap layer, and by the diffusion of a zinc finger partially through the p-cladding layer (Fig. 1). The lasers are separated by 150 μm, a distance that is photolithographically defined by the mask pattern used to etch the channels and contact stripes. (Masks were generated by the MEBES facility at the RCA Solid State Division.) This distance is a compromise between the desire to pack as many lasers as possible into the field-of-view of the optical recording system and the need to minimize crosstalk between the diode elements. Three elements of the array structure are shown in Fig. 8.

Electrical crosstalk between elements is eliminated by the formation of 50-μm wide channels between the elements. These channels are ion milled through the p-contact metallization (comprised of Ti-Pt-Au) and the active layer of the CSP structure. Each array is 1.95 mm in width and 100 μm in thickness, and is cleaved to have a cavity length of 200 μm, and coated to produce 90% reflectivity on the back facet and 10% reflectivity on the front or emitting facet. The array is attached to a thermoelectrically cooled submount that provides individual electrical contact to each of the lasers while maintaining the device in a suitable mechanical and thermal environment. The p-side of the chip is soldered to a metallized electrode pattern deposited on a beryllia substrate.

Twenty-five arrays from the first wafer growth of CSP array material were cleaved, facet coated (with 90% and 10% reflectivity coatings), probe tested, and mounted on metallized BeO submounts. Test results of those arrays having three or more adjacent elements operating at 30 mW cw or greater output power in a fundamental spatial mode are shown in Table I. The last lot of eight arrays processed from this wafer had argon ion-beam-sputter cleaned facets resulting from improved results on individual lasers being fabricated concurrently.

These results are interesting in several respects. Most noteworthy is the relatively good yield of useful arrays, albeit based on a very small sample size. Also, the variation of the CSP far-field FWHM is roughly a factor of two less than for CDH-LOC array far-fields. The greater uniformity of the CSP far-fields should result in more efficient matching of the ouput light to the optical systems required for recording systems.

TABLE I. MULTIDIODE CSP LASER ARRAY

Preliminary Test Results
Wafer NBC-8

Array	Number of Contiguous Single Spatial Mode Lasers Operating at 30 mW cw
2	3
3	3
6	4
11	4
14	3
15	6
16	6
18	9
21	10
22	3
23	9
24	8
25	7

Figure 9 shows the optical output power-versus-input current (P-I) characteristics for array #21, our best device with each laser operating to at least 30 mW cw. Threshold currents range from 76 to 92 mA and differential quantum efficiencies are 38 to 56% for the lasers in this array.

Figure 10 shows the lateral far-field intensity profiles for each of the ten lasers at 30 mW cw [7]. These show single-lobed fundamental spatial mode operation, necessary for use in diffraction limited systems used in high performance optical recorders. The full-widths at half-maximum (FWHM) of the far-fields are also reasonably uniform, ranging from 7.8 to 9.5°; FWHMs of the transverse far-fields are about 30°.

For optical data recording applications, the longitudinal mode spectrum is not particularly critical as the lasers are used as a highly localized source of heat. The operating wavelengths must, however, fall within the wavelength bandwidth of the optics. The cw spectra of each of the ten lasers -- operating individually -- in this particular array are shown in Fig. 11. The mean output wavelength is 8340 Å. Array elements 1 and 2 are characterized by substantial

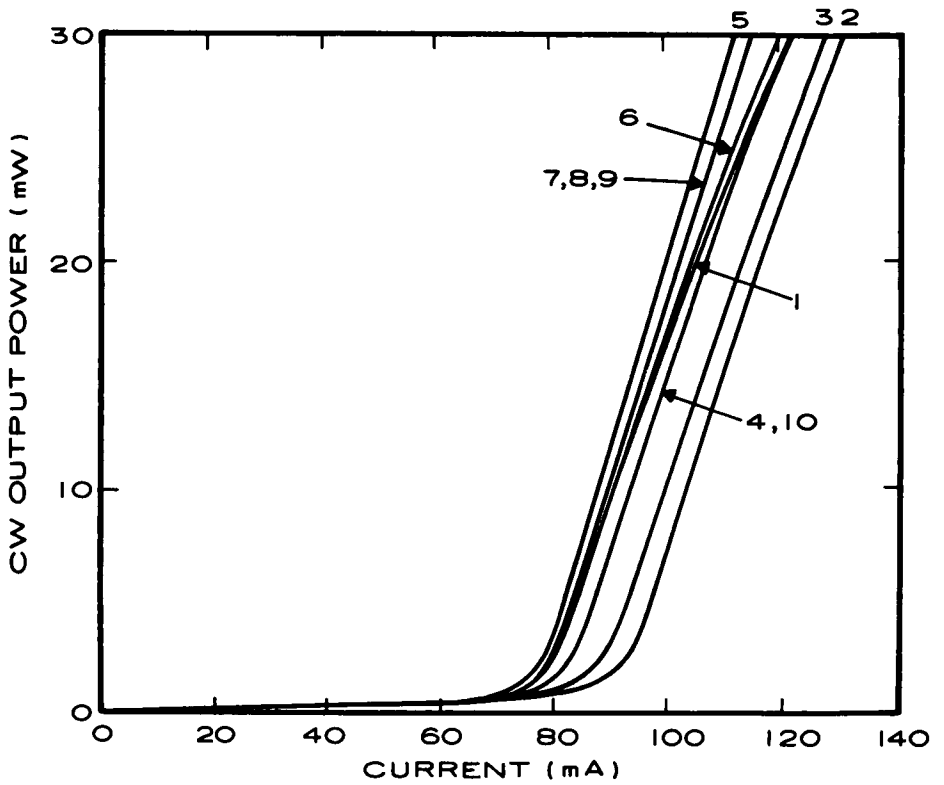

Figure 9. P-I characteristics of the lasers in a ten-element array.

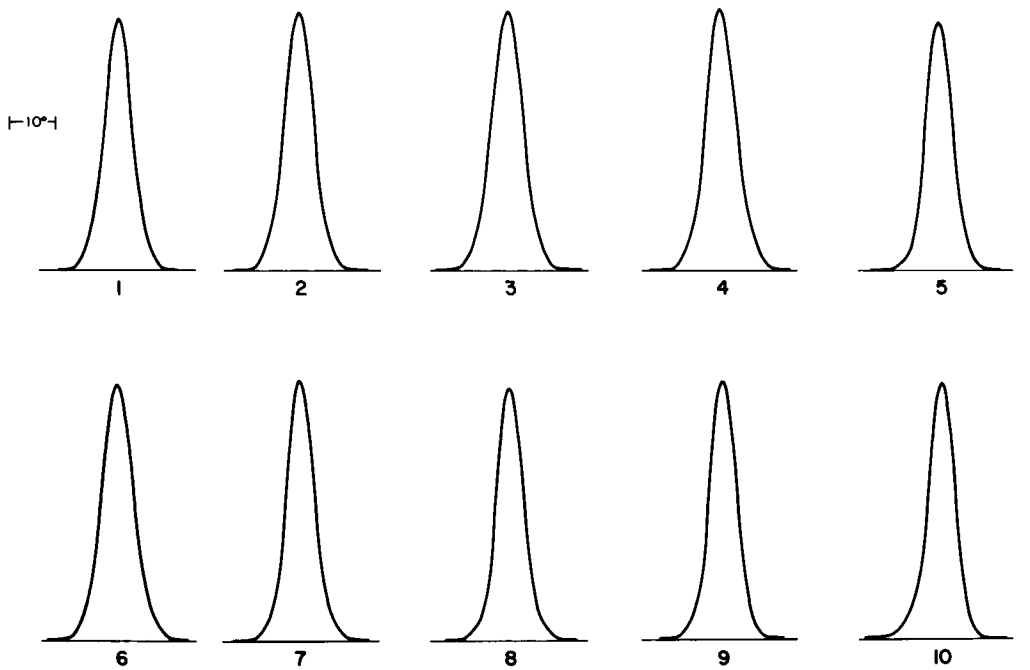

Figure 10. Lateral far-field intensity profiles of a ten-element array, with each laser operating at 30 mW cw.

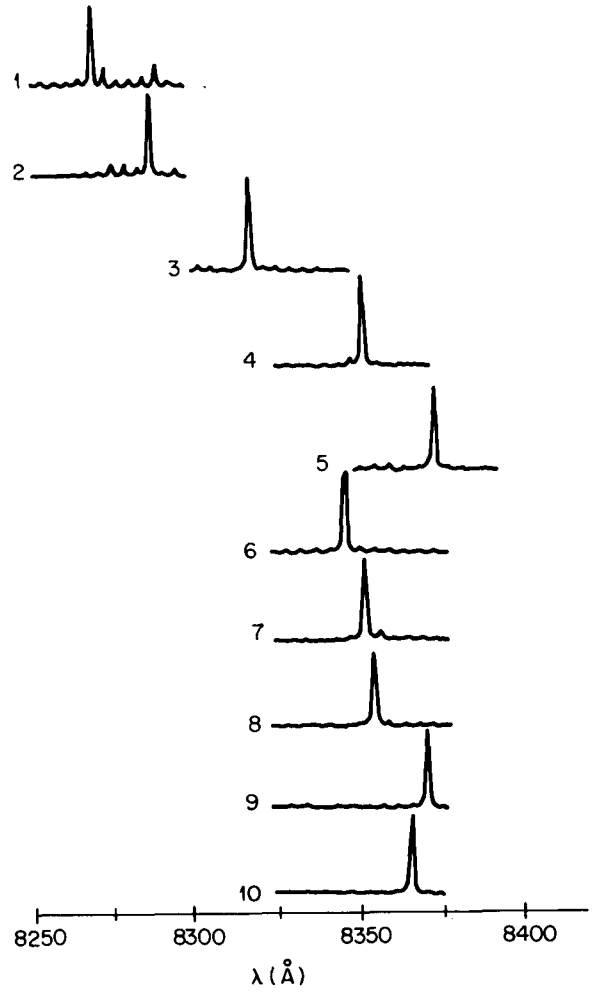

Figure 11. Spectra (cw) of array elements of 1 (top) through 10 (bottom).

emission in several Fabry-Perot modes, while elements 3 through 10 each emit predominantly in a single longitudinal mode. The variations in output spectra are probably due both to nonuniform thermal contact between the p-side of the chip and the substrate, and inhomogeneities in the the composition of the LPE grown material.

Arrays of this type will eventually be required in greater numbers than RCA Laboratories can reasonably supply, both for RCA's own Aerospace and Defense optical recording programs as well as for use as sources in other optical recording, signal processing, printing, and scanning applications as well as for optically interconnecting electronic circuits.

For these reasons, the RCA Electro-Optics organization in Montreal, Canada, is taking steps to transfer the array fabrication technology to its mass production facilities, a process that will result in the incorporation of the multidiode array into its product line. Certain of the processes involved in the fabrication of the arrays, while appropriate for laboratory prototypes, must be made more efficient for economic manufacture of such a product.

Three particular processes have been targeted for improvement in this regard: probe testing of unmounted array chips, mounting of the chips to submounts, and full characterization of the optical output of each of the mounted array elements. We investigated the first two issues during this past year.

Due to the time and cost involved in mounting and testing the arrays, the chips are probe-tested to eliminate substandard devices. This is especially important for arrays, as the device yield should be relatively low, compared to individual laser units, because of the number of adjacent lasers which all must exceed specifications simultaneously. At present, the array chips are manually probe-tested to obtain low duty-cycle lasing threshold currents for each of the ten lasers in the array chip.

We have developed a fixture to hold the array chip in an automated probe-tester, which will yield both full power-versus-current characteristics and far-field intensity profiles at low duty-cycle. The chip is placed in the vacuum chuck of the fixture (Fig. 12), and aligned in the center of the field of view of a high-power microscope objective mounted on a turret (Fig. 13). Diode laser elements are addressed under low duty cycle drive conditions (to minimize thermal load on the unmounted chip) by a single circuit routed through a coaxial switching tree.

The micropscope objective projects an image of the near-field of the array element under test onto a vidicon. The light distribution pattern is then shown on the lower monitor at the right of Fig. 14, a photograph of the optical system of the automated probe tester. Visual examination of the near-field facilitates alignment and also provides a quick way to eliminate diodes not operating in the fundamental spatial mode. The other, lower power microscope objective shown in Fig. 13 on the turret projects an image of the far-field of the array element under test to a second vidicon. This image is viewed on the upper monitor of Fig. 14.

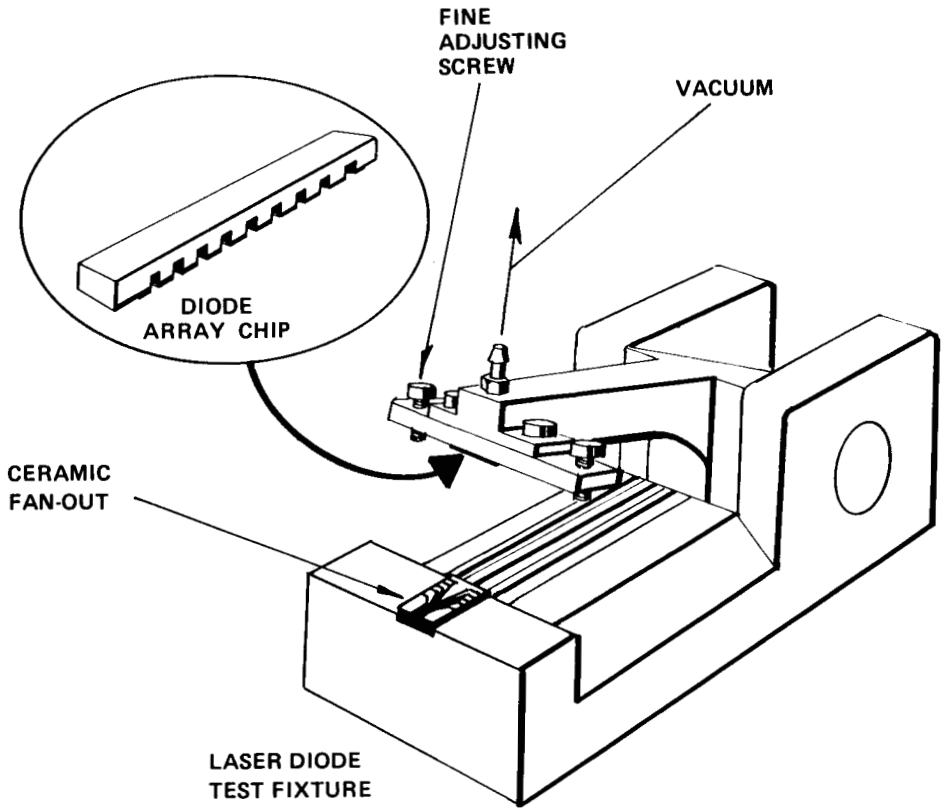

Figure 12. Schematic view of the array holding fixture of the semi-automated probe tester.

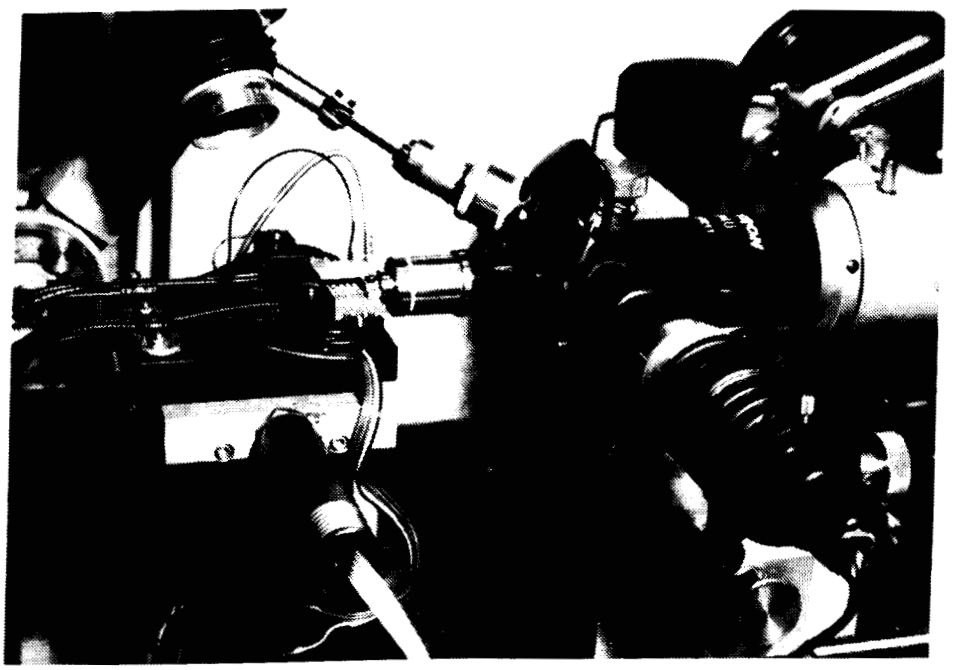

Figure 13. Photo of the array-holding fixture, lateral translation stage, and microscope objective turret of the probe test system.

ORIGINAL PAGE IS
OF POOR QUALITY

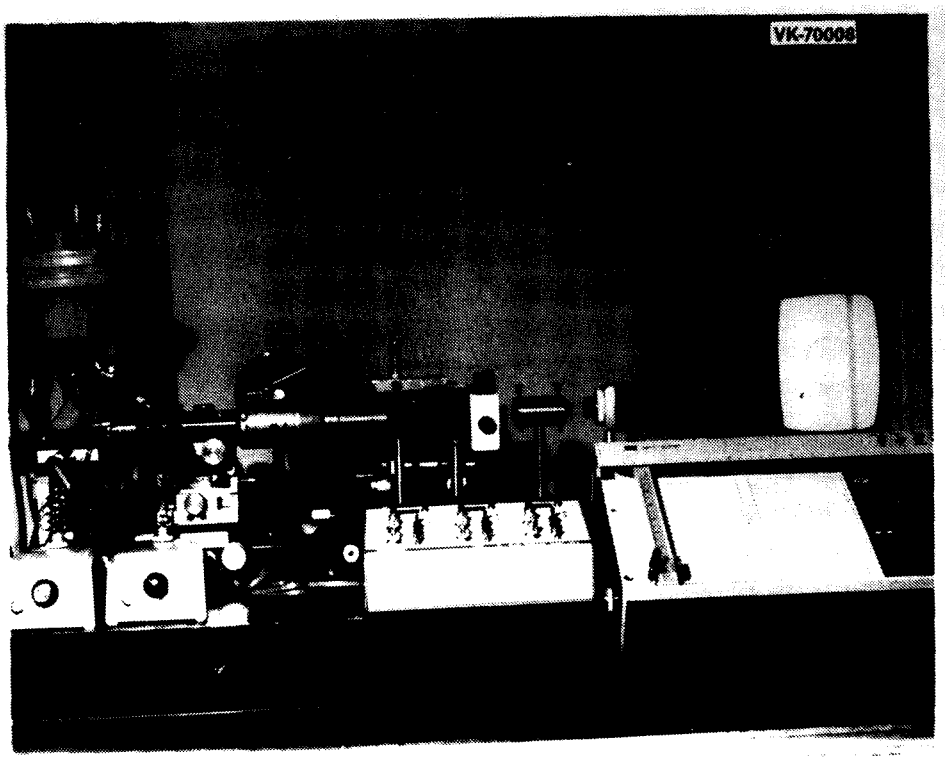

ORIGINAL PAGE IS
OF POOR QUALITY

Figure 14. Optical benchtop of the array probe tester, showing array-holding fixture, optical system, near- and far-field monitors, and plotter.

For hard-copy plots of the P-I characteristic of each element, part of the beam is directed to an APD as the current is ramped up. The lateral far-field intensity profile, sampled by a translating slit, is also measured by use of the the same detector and graphed by the plotter in Fig. 14. Each element of the array is successively brought to the center of the field of view of the optical system by motorized lateral translation of the array holding fixture in calibrated steps of 150 μm. The probe tester has been calibrated and is fully operational.

Bonding the array chip to the metallized beryllia submount has been a manual operation to date. This is a slow process and requires exceptional skill. As such, it is not well suited to mass production of arrays. Consequently, we have been investigating machine bonding techniques as well as compatible bond metallurgies compatible. Most of the work described has been tested initially on individual diode lasers, but the results should apply to array chips as well.

Machine mounting of individual CSP lasers to L-mounts has been very successful. The technique involves plating a submount with tin solder and then

holding the diode chip, submount, and package (L-mount) in fixtures while the assembly is heated in a Tokyo Sokuhan bonding machine. The thermal resistances of devices mounted in this manner are only slightly higher (statistically insignificant) than those mounted by hand using indium solder (42°C for machine fluxfree hard solder mounting vs 36°C for In flux hand mounting). Fixtures have recently been fabricated to align and hold the BeO submount for the array and ten-diode array chip in this automated bonding apparatus, and sample, substandard chips have been designated for initial machine mounting tests.

IV. LASER PERFORMANCE AT 8650 Å

In time, this report covers approximately the first half of the 8650 Å laser development program. This 8650 Å part of the overall program is aimed at the development of lasers at 8650 Å comparable in performance to those at 8300 Å for use in intersatellite communications applications and specifically the NASA Advanced Communications Test Satellite (ACTS) [2,8]. In this section we will treat only modeling, growth and performance, and in the next section, the reliability issues.

A. DEVICE MODELING

Previous work on high power AlGaAs lasers had centered on 8300 Å, or shorter, wavelength devices. Thus, the complex effective index curves had to be recalculated for wavelengths near 8600 Å. The effective index technique is extensively used to calculate the mode properties of CSP lasers and a physical explanation of the lateral guiding mechanism in CSP lasers appears in Reference 9, appended to this report. The complex effective index is defined as:

$$n^* = \lambda/k_o = \beta/k_o + j\alpha/k_o$$

where $\lambda = \beta + j\alpha$ is the longitudinal propagation constant of the mode.

The real and imaginary parts of the complex effective index are shown in Figs. 15a and b. While there is a noticeable shift in the magnitude of the real part of the effective index as the wavelength changes from 8300 Å to 8600 Å, the lateral effective index step is essentially unchanged. The lateral effective index step Δn in a CSP laser is defined by:

$$\Delta n = \beta/k_o \text{ (inside the channel)} - \beta/k_o \text{(outside the channel)}$$

The standard n-clad thicknesses for 8300 Å wavelength CSP lasers is 0.3 μm outside the channel and 1.8 μm inside the channel, resulting in a lateral effective index of about 3×10^{-3} to 7×10^{-3} as the active layer thickness is varied from 1000 Å to 600 Å. From Fig. 15a, it can be seen that this same range in lateral effective index step is obtained at 8600 Å for the same n-clad and active layer thicknesses.

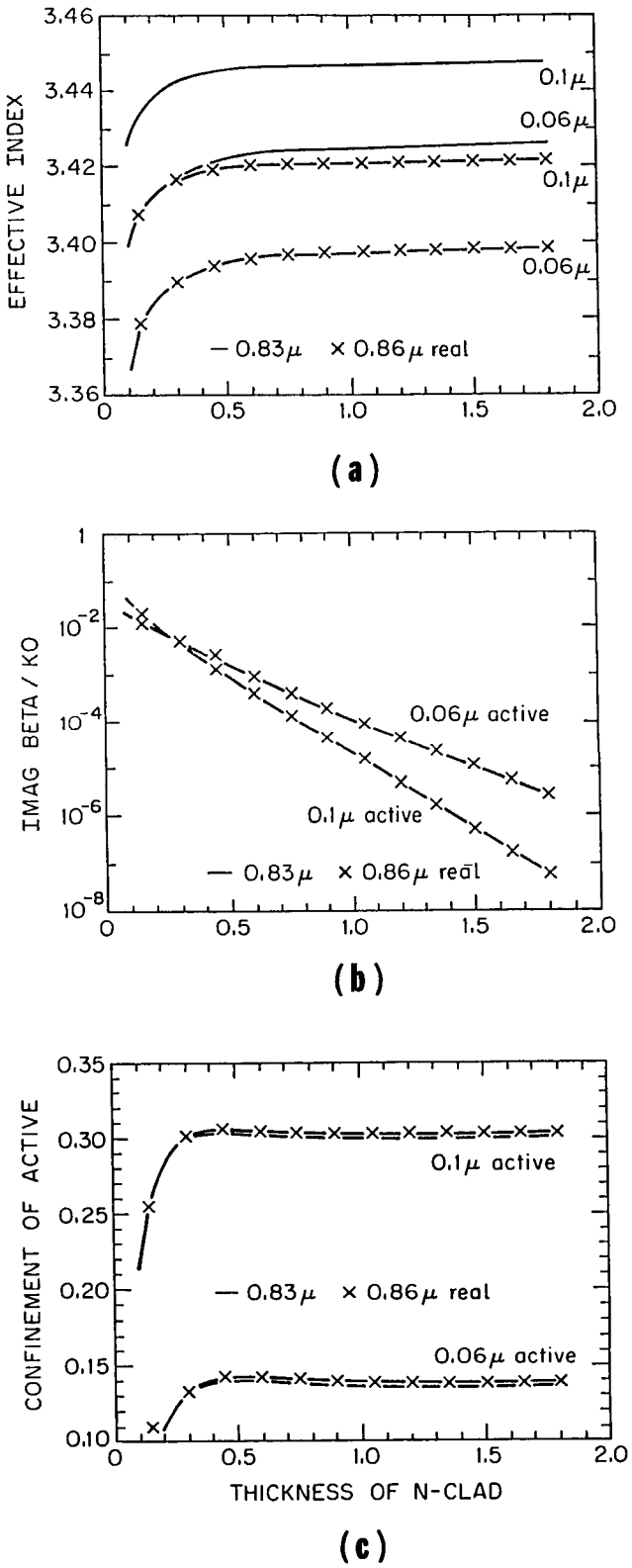

Figure 15. Real (a) and imaginary (b) parts of the effective index, and active region confinement factor (c) vs N-layer thickness for 8300 Å and 8650 Å at different active layer thicknesses.

On the scale shown in Fig. 15b, the difference in the imaginary part of the effective index $\Delta\alpha/k_o$ as a function of n-clad thickness is not distinguishable. The difference in the imaginary part of the effective index is the imaginary part of the complex effective index step and is defined as

$$\mathrm{Im}[\Delta n^*] = \alpha/k_o \text{ (inside the channel)} - \alpha/k_o \text{(outside the channel)}$$

As a general rule, the imaginary part of the effective index step is approximately the same as the real part of the effective index step for CSP lasers.

Thus, despite a relatively large change in the lasing wavelength from 8300 Å to 8600 Å, there are insignificant changes in the lateral complex effective index step and the active layer confinement factor (Fig. 15c) for the two wavelengths. This behavior is explained by two compensating processes: 1) For a fixed active layer thickness, as the wavelength increases more of the mode intensity is outside the active layer. This process increases the lateral complex effective index step. 2) Because of dispersion in GaAs and AlGaAs, as the wavelength increases the index of refraction of the material decreases, tending to decrease the lateral complex effective index step.

Thus, the parameters (material composition, layer thicknesses, and geometry) that are optimum for CSP lasers at 8300 Å are also optimum for CSP lasers at 8600 Å.

B. LPE GROWTH TECHNIQUES

The first 8650 Å units made contained no intentionally added Al in the active region (only trace amounts carried over from the previous bin in the LPE boat). However, this was considered undesirable for the long run because the presence of Al in the active region made for better lattice matching with the cladding layers and minimized internal strain. Our solution to this dilemma was to have about 5% Al in the active layer but then to add at the same time sufficient Si to bring the wavelength to the desired value. It is interesting to note that there may be some side benefits to adding Si; it is used in commercial high-efficiency LEDs, and we also employed it in our very long lived (10^5-10^6 hours) oxide-stripe gain-guided laser diodes.

We also introduced the use of a semi-automatic LPE growth system to increase the overall device yield of our growths and to improve uniformity and reproducibility. As a result, growth parameters and yield improved significantly. Table II shows statistics from a single grown wafer, in which we

note especially the 25% yield on CSP lasers at 8650 Å exhibiting single-mode operation.

TABLE II. PERFORMANCE TEST DATA FOR WAFER L-437

Number of diodes mounted = 41
Number of diodes reaching 20 mW cw = 37
Number of diodes reaching 40 mW cw = 15
Number of diodes single longitudinal mode (40 mW cw) = 9
Number of diodes single longitudinal mode (40 mW, 50% dc) = 10
Average λ = 8680 ± 50 Å (25 lasers)
Average CW threshold: 64 ± 13 mA (41 lasers)
Lasers for lifetest = 10
Efficiency for lasers on lifetest = 23.6 ± 7.8%

C. LASER DIODE PROCESSING AND MOUNTING

We have developed several improvements in our laser processing that involve photolithography, contacting, mounting, and facet coating, but since they apply to 8300 Å devices as well as 8650 Å devices, and also bear generally on the question of reliability, we will present these results in the next sections on reliability and lifetesting.

D. OPTOELECTRONIC PROPERTIES AND CHARACTERIZATION

We have fabricated lasers operating at 8650 Å to 8700 Å that have attained powers of 100 mW, 50% duty cycle, while maintaining their single-mode character. The data are shown in Fig. 16, which presents the P-I curve, the spectral content and the far-field pattern of a unit at 100 mW. Yield is low, however, and we are continually upgrading both the growth technique and the processing-mounting operation as described above and in the next section, in order to improve matters.

Diode lasers are becoming the preferred source for many types of diffraction-limited optical applications, including optical data storage and free-space communications [10,11]. The efficiency of such optical systems is limited by the losses between the transmitting laser and the detector. Aberrations in the output wavefront of the diode laser may have a significant deleterious effect on system performance, depending on the size and nature of the aberrations and

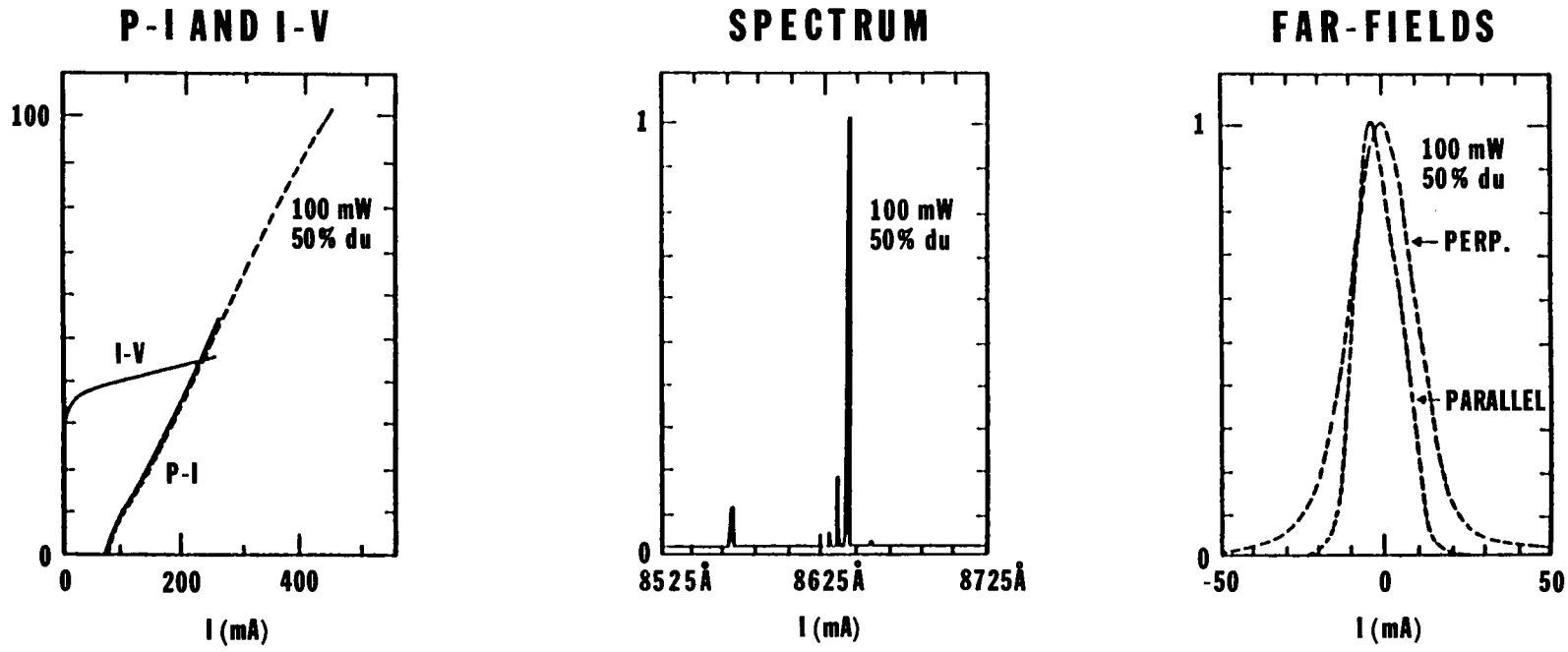

Figure 16. Power curve, spectrum, and far-field pattern for high power 8650 Å laser.

the particular system under consideration. Therefore it is important to characterize the aberrations of the output wavefront fully in order to predict system performance.

In addition, an understanding of the nature of the aberrations present may allow modifications of the laser structure designed to improve output beam quality.

A LADITE [12,13] computer-controlled Mach-Zehnder interferometer, manufactured by the Wyko Corporation, was used to measure the output wavefront from a variety of AlGaAs diode lasers emitting in the 0.81- to 0.87-μm regime. This device measures the properties of a collimated beam. The aberrations of the collimation optics must therefore be neglible compared with those of the diode. In fact, the wavefronts of the collimating optics used in these investigations were independently measured to be $\leq \lambda/13$ rms. In addition, a differential measurement technique [14] was employed in which changes in the wavefront as a function of operation conditions was determined. The computer subtracts the phase fronts of the diode laser measured at two different output powers; the difference represents the power-dependent component of the phase front. The use of this technique can detect changes as small as $\lambda/50$.

Of the applications currently envisioned, the needs of free-space communications place some of the most formidable requirements on diode laser characteristics and are, therefore, driving the development of the technology. For this application, the device emit extremely high output power ($\geq$ 100 mW) in a stable, single-lobed aberration-free beam. Figure 17 shows the phase fronts of a CSP diode laser operating near 8650 Å at 1, 20, 60, and 100 mW cw. The rms phase front aberrations for this device were better than 0.037λ for all cases. Collimation of the output was effected by an objective of 0.615 NA.

Similar studies of the phase fronts of the emission from gain-guided double-heterojunction lasers show abberations of $\approx \lambda/7$, primarily due to astigmatism. Use of the latter would clearly degrade the performance of a system incorporating diffraction-limited optics. Detailed studies of CSP devices have shown negligible wavefront aberrations at cw output powers up to 100 mW and pulsed operation to 120 mW [8].

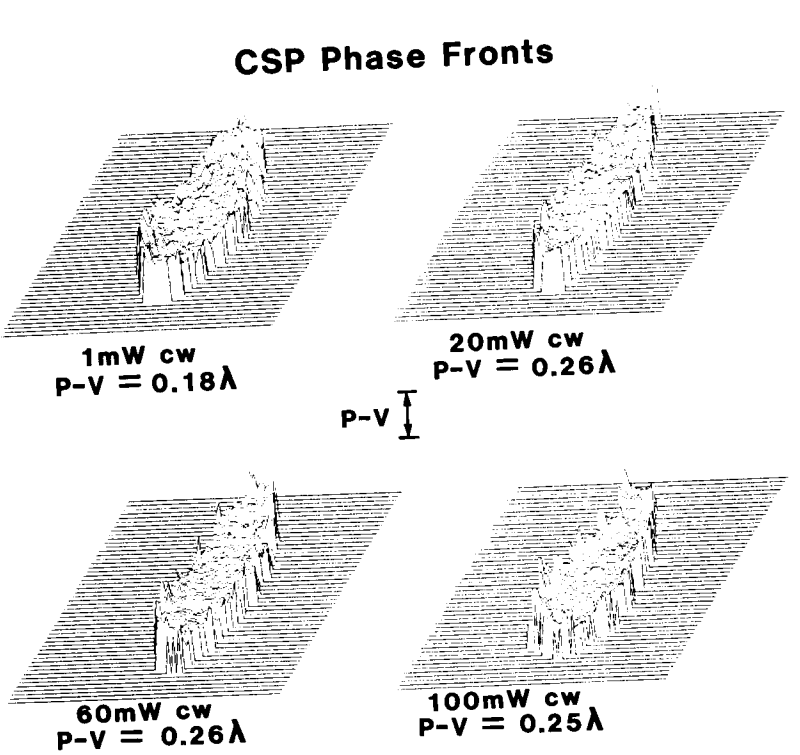

Figure 17. Phase fronts of the output beam from a CSP diode laser operating near 8650 Å showing the peak-to-valley aberrations as a functional output power. The rms aberrations were 0.025, 0.029, 0.029, and 0.037, respectively, for 1, 20, 60, and 100 mW cw output.

V. RELIABILITY

While laser life and reliability studies have been present in several NASA funded programs, they have generally tended to be peripheral to other issues. Recently, however, it has begun to receive the active attention it deserves -- especially in view of specific reliability requirements of the NASA ACTS program. Sections V and VI discuss those developments that have affected (or could affect) reliability and life. Most of the discussion is applicable to operation at both 8300 Å and 8650 Å, but it will be noted where they pertain principally to one or the other.

A. IMPROVED FACET COATING

It is now standard practice for us to clean the mirror facets before coating by an in situ ion bombardment. A 3-cm source of the Kaufman design is employed for this purpose. During ion bombardment, the system pressure is increased to 10^{-4} torr (from a base level of 10^{-7} torr) by the introduction of ultrapure argon, which is the ion source gas. Energies and times are kept low (<200 V for 5 minutes) to avoid or minimize damage while still removing essentially all the carbon and much of the oxygen (as measured by Auger Analysis). From its inception, this procedure produced facet coatings with very much improved adherence annd structural integrity. Perhaps more importantly, indications were observed that life may be improved.

Figure 18 shows two sets of aging curves of individual lasers from the same grown wafer whose only difference in processing was the low energy ion cleaning mentioned above. Without facet cleaning, (a), all units showed immediate degradation (rising bias current) and failed (with one exception) in less than 1000 hours. With facet cleaning, (b), the test units continued operating with bias current changes of less than 10%. We speculate that facet cleaning not only removes contamination so that the films are more adherent, but may, in addition, change the electronic nature of the surface states so as to decrease optical absorption and, hence, facet temperature. Also, a cleaner surface may decrease the mobility of surface atoms and prevent their participation in bulk degradation processes.

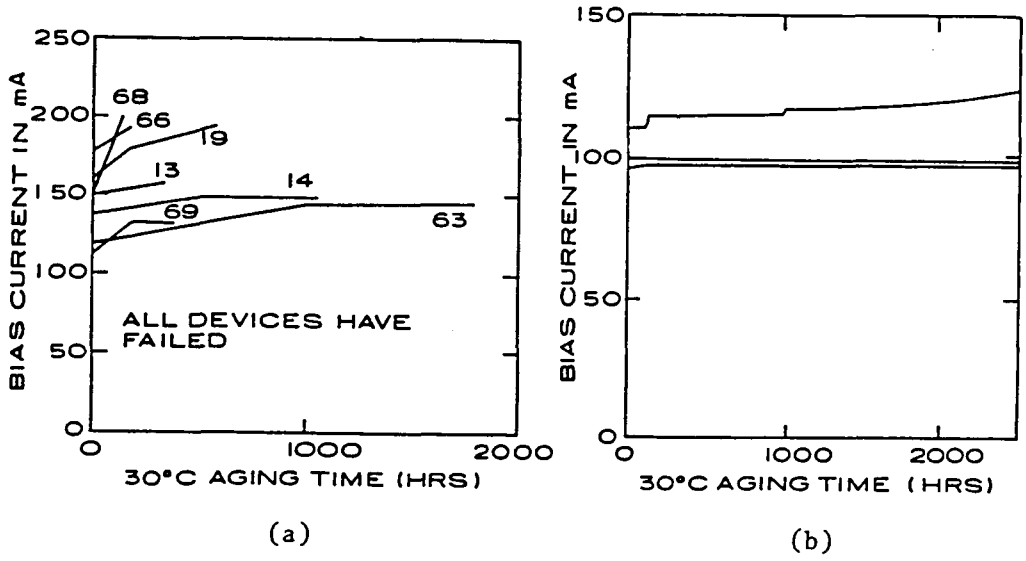

Figure 18. Aging time vs bias current for lasers from the same wafer; (a) without improved facet treatment and, (b) with improved facet treatment. Units in (b) fare comparatively much better.

As part of our process-upgrading program we have recently acquired, and are in the course of calibrating, a plasma deposition system capable of depositing both SiO_2 and Si_3N_4 films. Uniformity is running 5% or better within one deposition and from film to film, with very good confinement of lateral Zn diffusion. It is also expected that these films will ultimately have a lower pinhole density than the CVD films.

B. MECHANICAL BONDING

The use of indium, with its fluxes and cleaning solvents, low softening point, and tendency to creep, portends long term stability problems for its use for high power devices. We have developed a mechanically assisted fluxless bonding process using electroplated tin (as opposed to manually applied In) on copper heat-sinks. The mounting is performed on a Tokyo Sokuhon die mounter specifically designed to mount GaAs devices using very low mounting forces down to a few grams.

A vacuum collet is used to pick up, place, and align the laser die onto the heat sink, while a programmed cycle of preset temperature and specified time then attaches the die in an atmosphere of forming gas which obviates the need for flux. The connection to the other side of the die is made by

ultrasonic wedge-bonding with gold wire. (A laser die so mounted is shown in Fig. 19). Thermal resistances are averaging about 42°C/W (as compared to 36°C/W for hand mounted units), there seems to be no deterioration in other optoelectronic properties, and lasers are currently being routinely mounted in this fashion.

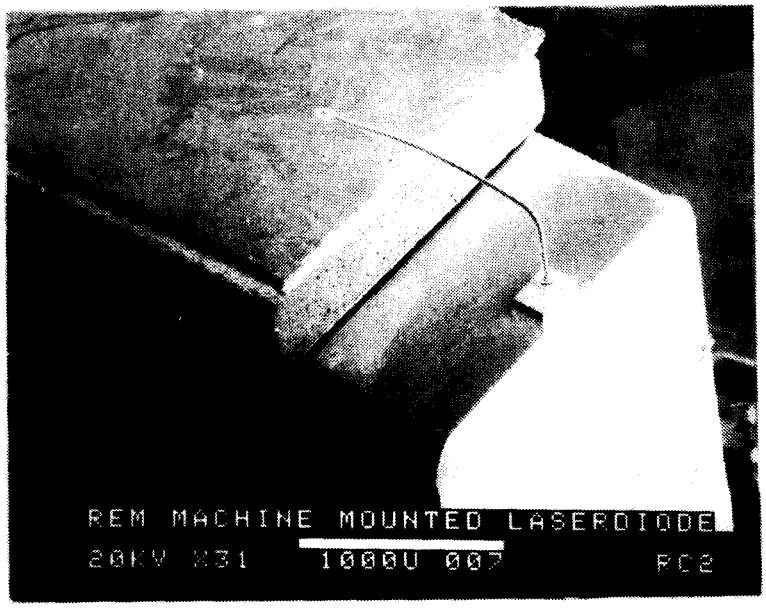

Figure 19. Laser diode mounted by a Sokuhon die-bonding machine.

C. MULTI-MODE OPERATION AND LIFE

A correlation between the presence of multi-spectral modes and a shorter laser life has been found. Figure 20(a) shows aging time vs percent failures for unselected and non-optimized (all our lifetests of research grade units) single-spectral-mode units and multi-spectral-mode lasers. The single-mode lasers clearly have significantly better performance (regardless of mounting solder), with MTBF of greater than 5000 hours at 20 mW and 30°C ambient. Furthermore, the onset and growth of sideband power in subsidiary spectral modes after a unit has been put on lifetest seems to be a harbinger of failure, even though no other change in operating properties has been observed.

Figure 20(b) shows a lasing spectrum that is increasing in side modes with aging for a unit in which failure occurred at just over 4000 hours. The spectrum change leading up to failure is clear. We can offer no really sound speculation for this observation; however, the data indicate that even though

ORIGINAL PAGE IS
OF POOR QUALITY

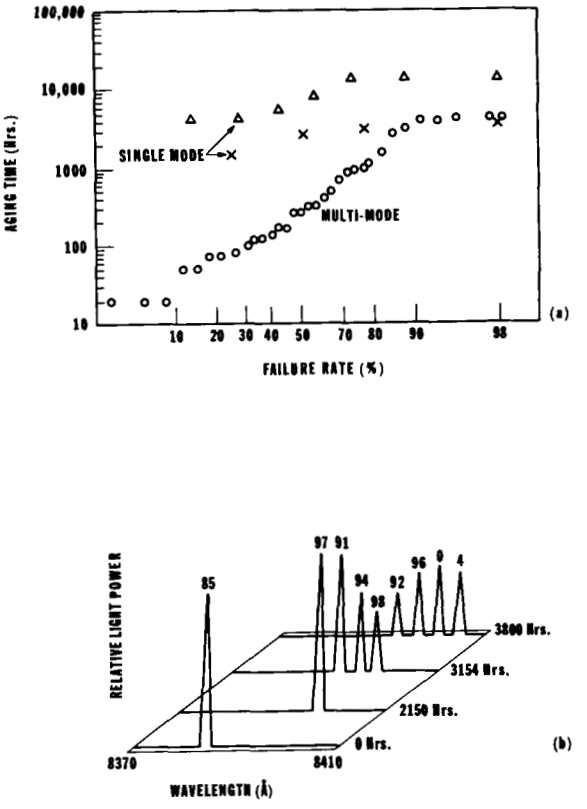

Figure 20. Data relating multi-longitudinal-mode behavior with degradation. (a) single-mode units have clearly superior life; (b) onset of spectral sidebands is a harbinger of impending failure.

the failure mode remains abrupt after apparently stable operation, there actually may be changes going on in the laser associated with degradation that are not readily visible in either power or spatial mode behavior.

D. FAILURE ANALYSIS

Failure analysis is an important part of any reliability program. During the period covered by this report, we have established a research effort dedicated to developing and adapting state-of-the-art analytical techniques for use in diode laser failure analysis. The various techniques have already pointed up several faults in our devices or processing that may be causing instabilities or early failures. One degree angle-lapping, a polishing technique that produces a 57 times magnification of the epilayer structure in the direction perpendicular to layer growth, followed by appropriate staining, has led to observations of zinc penetration into the active layer (Fig. 21),

non-planar growth profiles (Fig. 22), and active layer thickness variations in failed devices.

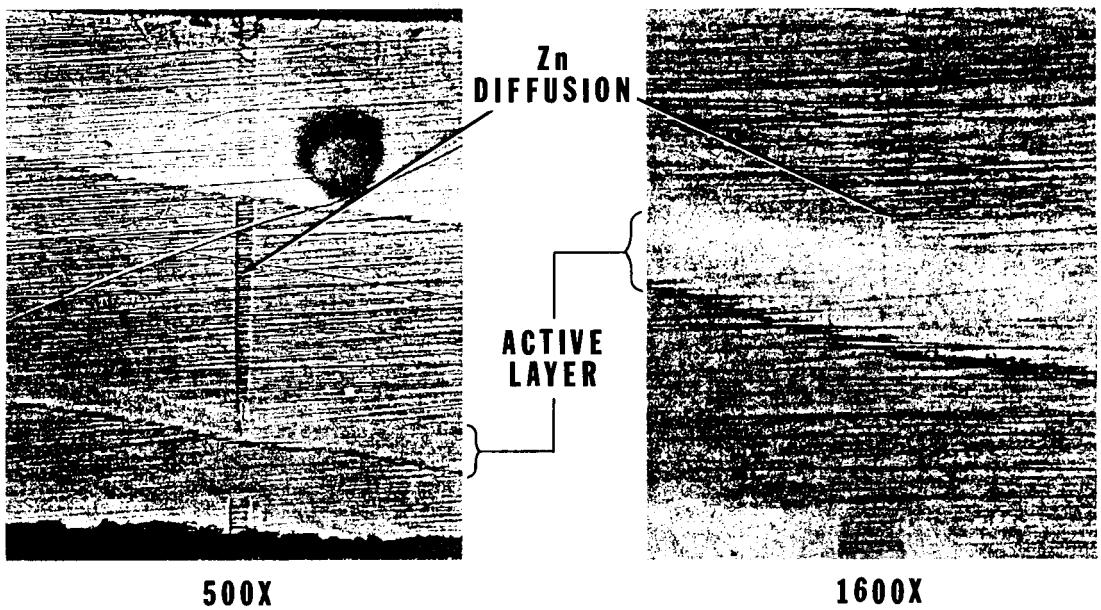

Figure 21. Angle-lap at 1° of CSP cross-section showing Zn penetration into the active layer.

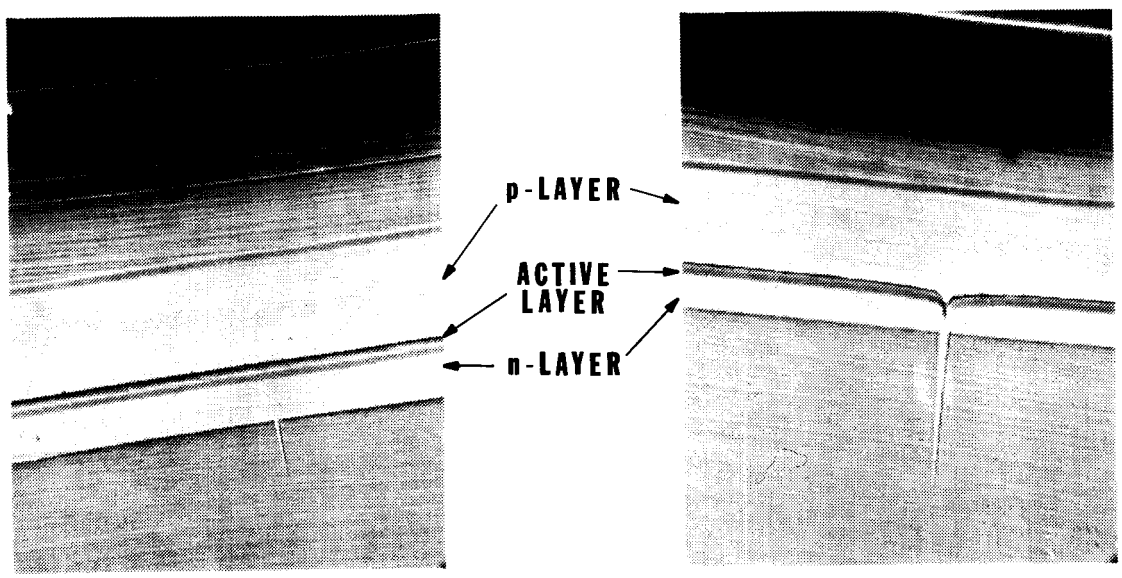

Figure 22. 1° angle-lap cross-sections showing (a) nonplanar and (b) planar active layers.

Reductions in diffusion times have essentially eliminated the first of these problems by keeping the Zn diffusion front more than 0.5 μ from the active layer (this has negligible effect on laser operation as indicated by the

ORIGINAL PAGE IS
OF POOR QUALITY

modeling data in Fig. 5), while the second and third have been corrected by changes in LPE growth procedures. A sample preparation technique that enables the production of thin sections of individual diode lasers suitable for examination by transmission electron microscopy (TEM) has been developed. TEM is now being used to examine problems such as solder voids and lapping damage. It has also been used to take the first photos at high magnification of the CSP structure in the vicinity of the V groove (Fig. 23).

ORIGINAL PAGE IS
OF POOR QUALITY

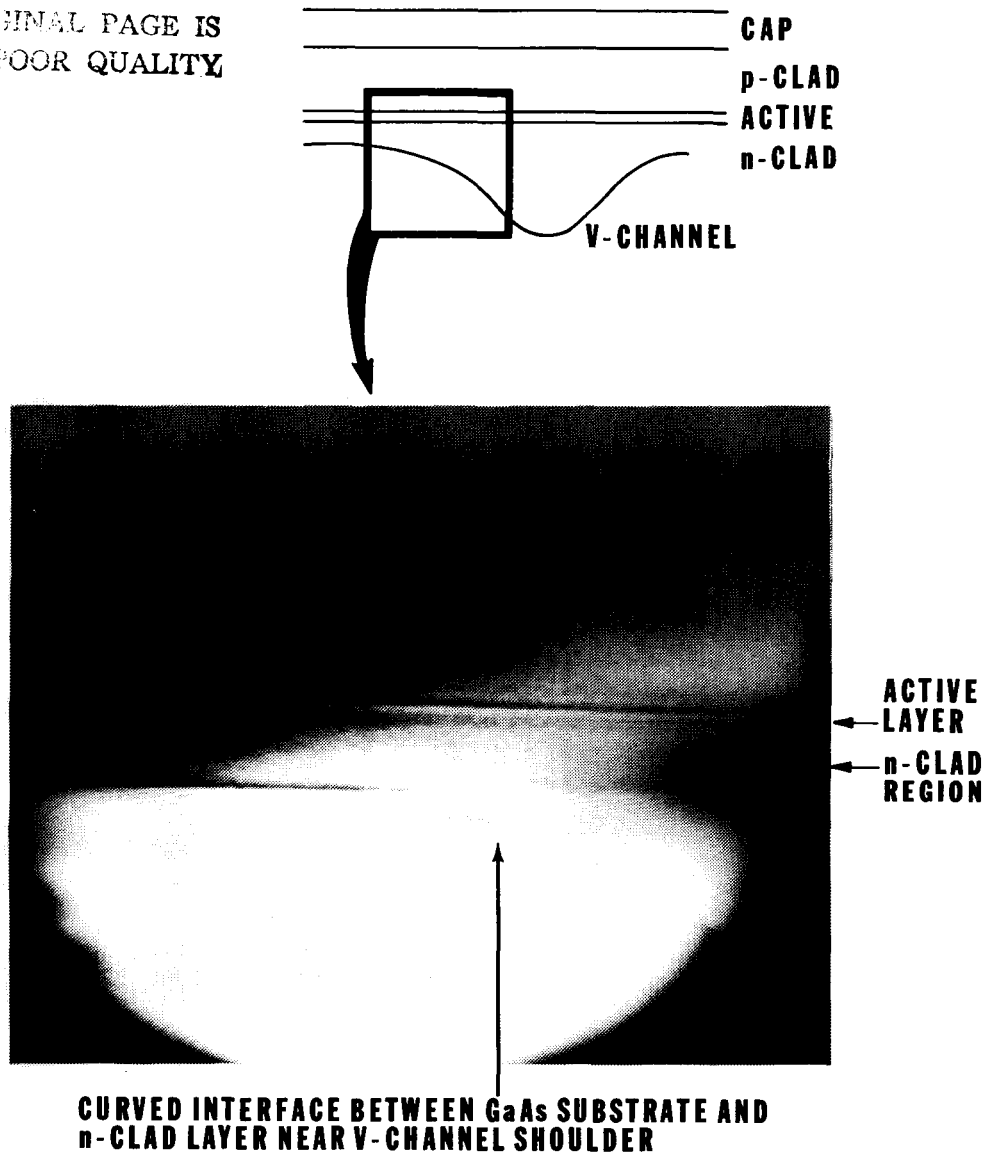

Figure 23. Transmission electron micrograph of CSP structure in the vicinity of the shoulder of the V-channel showing the continuation of buffer/n-clad interface into the region above the channel.

Cathodoluminescence (CL), a technique by which photons produced by electron bombardment are used to generate an image of a sample, is a capability of our newly acquired scanning electron microscope. This technique has enabled us to observe the dark line defects commonly thought to be associated with degradation. By combining cathodoluminescence analysis with angle lapping, we have observed an association between dark line formation and zinc penetration into the active layer. Figure 24 shows corresponding secondary electron and cathodoluminescence images of a CSP diode laser. A linear dark region is seen at the center of the stripe along its entrie length in the CL image. The dark line region is most obvious in the stripe etch pits and at the ends of the stripe, where the central dark areas are bordered by regions possessing greater luminescence efficiencies.

Another feature of the SEM is an energy dispersive spectroscopy (EDS) capability. This analytical technique provides compositional information derived from the energies of the x-ray photons whose generation is associated with the electron bombardment of the sample. Figure 25 shows two overlapping EDS spectra, one from the base of a crater and the other from the region outside it. Differences in aluminum content between the two regions and the complementary nature of the gallium and aluminum concentrations are observed. Near-surface compositional studies of defects such as craters and pits are made possible by this technique.

Finally, X-ray topography and wafer curvature measurements have been used to examine, respectively, local wafer damage and processing-induced stress in the wafer. Figure 26a shows an x-ray topograph of a wafer that was damaged during handling. The bright regions represent defects introduced into the crystal lattice by the high contact stresses accompanying handling wafer with fine-tipped tweezers. Figure 26b is a plot of the lattice orientation versus distance across the wafer (fixed diffraction angle) for GaAs/SiO_2 composites that were heat treated in different atmospheres. Residual stresses in the GaAs wafer can be determined from the curvature of the composite and minimized through judicious choice of sintering atmosphere.

The problems uncovered by the analytical techniques described above receive continual attention in our efforts to improve laser performance and reliability.

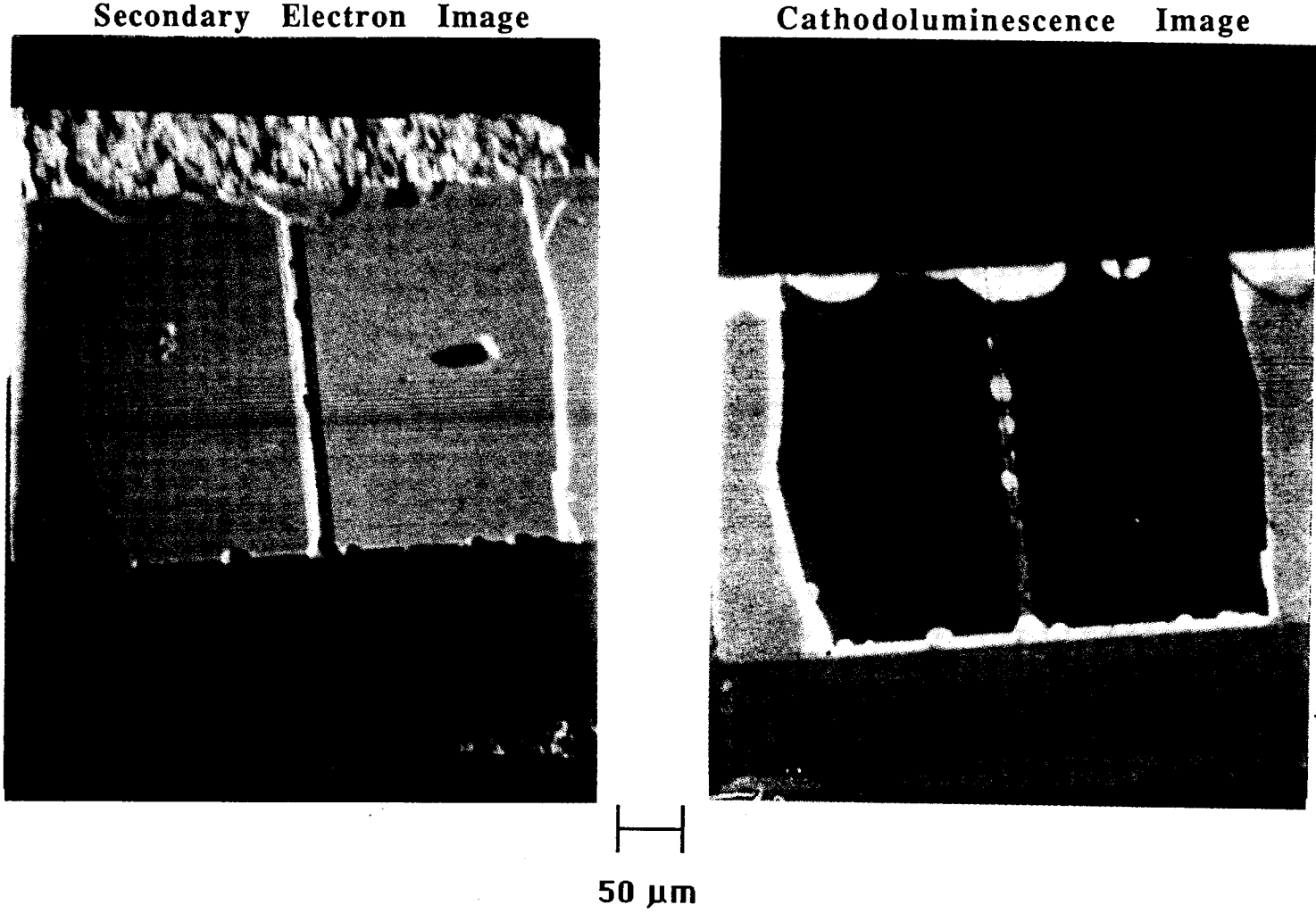

ORIGINAL PAGE IS
OF POOR QUALITY

Figure 24. Dark-line defects in contact stripe as brought out by cathodoluminescence and clearly related etch pits brought out by chemical etching.

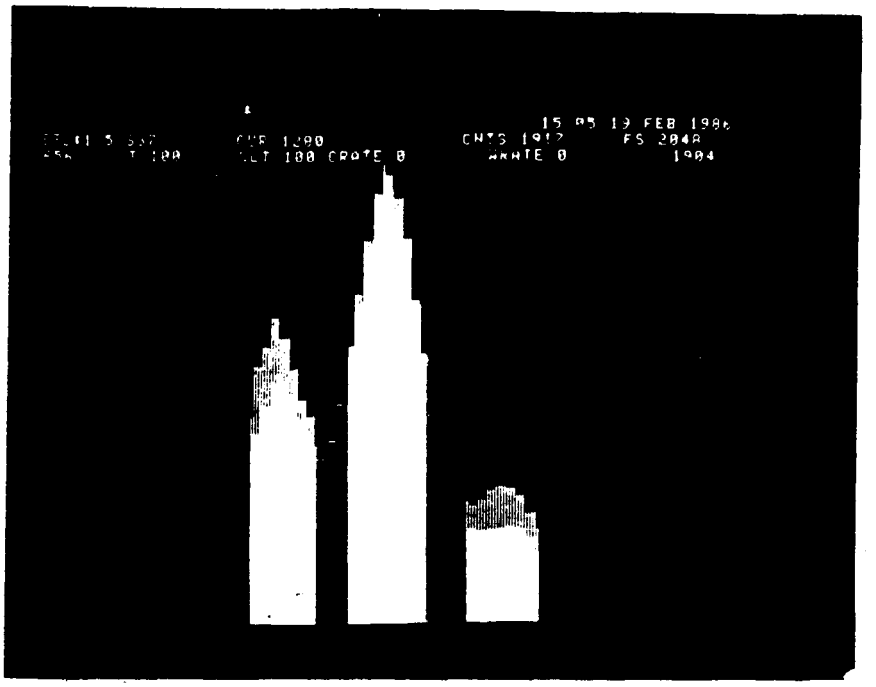

Figure 25. Overlapping EDS spectra from inside and outside a crater showing compositional differences between the two regions.

(a)

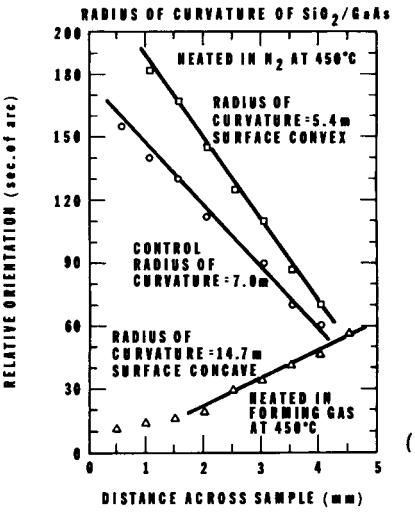

(b)

Figure 26. (a) X-ray topograph of GaAs substrate showing damage due to a tweezer-damaged GaAs wafer. (b) X-ray lattice curvature measurements for GaAs/SiO_2 composites sinitered in different atmospheres.

ORIGINAL PAGE IS
OF POOR QUALITY

VI. LIFETESTING

Lifetesting in our earlier programs typically assumed non-specific shapes, involving only a general assessment, failure diagnosis, and feedback. A very brief resume of our lifetest results for this earlier period (perforce for 8300 Å units) is given in Fig. 27(a-d). Operation at 20 mW cw can be considered fairly reliable and units are now approaching 20,000 hours with no apparent degradation. Based on 3000 hours, machine-mounted units also seem reliable. At 50°C ambient temperature, degradation begins immediately and units seem to be reaching their 50% power level at approximately 1000 hours. Operation at 40 mW cw also produces early degradation with operating life only to about 2000 hours.

Lifetesting in the 8650 Å program, however, directed as it is toward the ACTS program, has some well defined goals. One of these is operation at 65 mW at 50% duty cycle for 2000 hours (note the 2000 hour operation at 40 mW cw mentioned above). In this context, we have changed our customary life testing mode from constant power to constant current. There are two reasons for this. Many systems actually run in this mode so that we get a picture of the laser's power degradation that is more directly applicable to its use. Secondly, constant power operation actually double stresses the unit; not only is it running at rated power, but the temperature may be constantly rising due to the increases in bias current required to maintain that power.

For these lifetest assessments in the 8650 Å program we have introduced both a pre-screening schedule--to which the laser is subjected before it is incorporated into the lifetest proper--and a lifetesting plan that carries with it statistical validity and that spells out in detail the procedures to be followed. These are shown in Tables III and IV. The pre-screen elements are essentially self-explanatory. The lifetesting plan is mostly so, the most notable exception being that the definition of "device failure" is currently flexible and depends on the specified needs of the ACTS program, which may, in fact, change over a period of time.

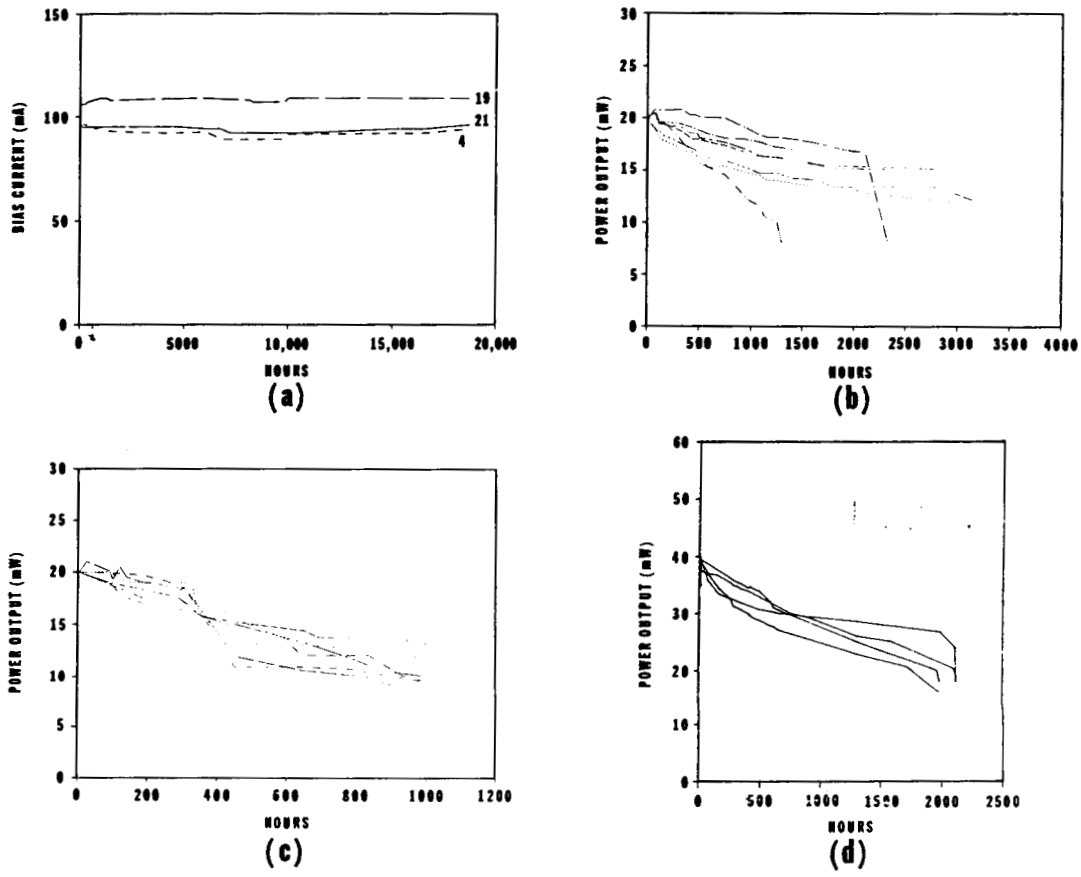

Figure 27. Brief summary of early lifetest results of 8300 CSP units. The data should be read only as trend indicators. All powers are cw. All aging times are hours. (a) 20 mW, 30°C, hand-mounted, constant-power, Indium. (b) 20 mW, 30°C, machine-mounted, constant-current, tin. (c) same as (a) but 50°C, and constant current. (d) same as (a) but 40 mW and constant current.

TABLE III. PRESCREEN OF RCA 8650 Å HIGH POWER CSP LASERS

- Screening
  - Selection of devices for lifetesting
  - Examine visual, electrical, and optical characteristics
  - Acceptable values determined from available data
- Visual
  - Diode alignment on mount
  - Solder bond condition (no voids or creep)
  - Facet coating quality (color and continuity)
  - Chip condition (no striations, cracks, etc.)
  - Mount area around diode (clean)
- Electrical
  - Thermal resistance - <50°cw
  - Leakage - V_f>1.1 Y at 1 mA
  - K factor - 0.4 to 0.8°C/mV mean, 0.1°C/mV variation
  - Threshold (cw and pulsed) - <80 mA
  - Series resistance - <1.8 ohms
- Optical
  - Single spectral mode
  - Single spatial mode
  - P-I curve - kink free
  - Slope efficiency - >20%
  - Parallel farfield divergence - 5.5° to 8.5°
  - Parallel to perpendicular farfield center shift - <10°
  - Wavelength - as per spec.

TABLE IV. LIFETESTING PLAN FOR RCA 8650Å HIGH POWER CSP LASERS

- 20 devices per temperature group (all pass screening)
  - Devices failing screening are tested to evaluate screening
- 2 temperature groups
  - 25°C - close to field operation temperature
  - 50°C - acceleration factor = 8.25 (assuming E_a = 0.7 eY)
- Must define the meaning of failure
  - Periodic insitu examination
    - Spectrum - initially and at 100 hour intervals
    - Optical power -
      - Continuously for first hour
      - Twice a day for next 100 hours
      - Daily for next 1000 hours
      - Every two days thereafter
    - Threshold - when optical power drops substantially
- Mode of testing
  - Constant current - Set optical output at elevated temp.
- Run test untial all devices fail
- Data analysis
  - Computer analysis - Accelerated lifetest software
    - Maximum likelihood method
      - Input lifetest data and confidence interval
      - Output extrapolated lifetime
  - Graphical
    - Arrhenius plot
      - Distributions at elevated temperatures
      - Extrapolate mean and deviation to operating T
      - Desired life < 2 S.D. below mean life (95%)

Initial results at this time are encouraging; CSP diodes have been operating at 8650 Å in single mode at 35 mW cw for 900 hours.

Our work in this area is continuing with emphasis on reproducible reliability for single-mode lasers at 8650 Å.

VII. CONCLUSIONS

Continued development of the CSP AlGaAs structure has led to an increased understanding of the liquid phase epitaxial techniques required to fabricate such devices as well as an improved understanding of the performance capabilities of the device. Indeed, an argument may be made that much of the thrust of the diode laser industry in the development of a individual very high power, index-guided diode laser emitters has been directed at CSP and CSP-like devices. Such variations include the V-grooved substrate, inner strip (VSIS) from Sharp [15], MOCVD-grown self aligned strip structures, as typified by the self-aligned stripe with bent active layers (SBA) by Mitsubishi [16], the T^3 device, also by Mitsubishi [17], and the buried twin-ridge structure (BTRS) from Matsushita [18].

High power, high performance operation at emission wavelengths near 0.87 μm from modified CSP devices was demonstrated during this past year. This may be important because of the transparency of the atmosphere in this wavelength regime. Indeed, a possible candidate platform for initial space-to-ground optical communications links, the Advanced Communications Technology Satellite, is designed to operate at such longer-than-normal wavelengths for AlGaAs devices. Reliability at this wavelength is currently a predominant concern. Further work is necessary to determine whether the accelerated degradation of devices seen thus far is due to device design, growth, processing, or is an inherent consequence of the added strain imposed on the structure by the required layer compositions.

Continued success was achieved in the further development of monolithic arrays of individually addressed CSP lasers, primarily intended for optical data storage applications. Indeed, this technology has progressed to the point where yield, reliability, and packaging issues are of immediate concern rather than demonstration that the device meets the performance specifications required for incorporation into real systems.

Because of the potential applicability of AlGaAs diode laser sources in spaceborne communications systems, device reliability and stability at high output powers has become a critical issue, as yet not completely resolved. While advances made during this past year -- such as improved facet coatings -- manifest themselves as increased laser life, models describing the degradation

mechanisms of CSP devices are not yet completely satisfactory. Empirical observations give indictions of underlying thermal mechanisms; often the lasing wavelength at 1% duty-cycle is significantly different from that at cw operation. This may reflect heating in the active layer, present in varying degrees in different wafer growths.

Additional experimental evidence suggests that increasing the near-field area on the facet will significantly improve device life. Achieving this may involve thinning the active layer to widen the spot in the direction perpendicular to the active region. We expect to continue investigations in these areas during further development of the CSP laser.

REFERENCES

1. D. B. Carlin, B. Goldstein, and J. K. Butler, "AlGaAs heterojunction lasers," NASA Contractor Report 178085, Contract NAS1-17441, NASA Langley Research Center, Hampton, VA, February 1986.
2. RFP-90143/237 NASA Goddard Space Flight Center, Greenbelt, MD, 15 July 1986.
3. J. K. Butler, G. A. Evans, and B. Goldstein, "Analysis and performance of channeled-substrate-planar double-heterojunction lasers with geometrical asymmetries," IEEE J. Quantum Electron. QE-23, Nov. 1987, p. 1980.
4 D. B. Carlin, J. P. Bednarz, C. J. Kaiser, J. C. Connolly, and M. G. Harvey, "Multichannel optical recording using monolithic arrays of diode lasers," Appl. Optics 23, 3994-4000, 15 November, 1984; erratum 4613-9, 15 December 1984.
5 D. Botez, J. C. Connolly, D. B. Gilbert, M. G. Harvey, and M. Ettenberg, "High-power individually addressable monolithic array of constricted double heterojunction large-optical-cavity lasers," Appl. Phys. Lett. 41, 1040-2, 1 December 1982.
6. B. Goldstein, M. Ettenberg, N. A. Dinkel, and J. K. Butler, "A high-power channeled-substrate-planar AlGaAs laser, Appl. Phys. 47, 655-7, 1 October 1985.
7. D. B. Carlin, B. Goldstein, J. P. Bednarz, M. G. Harvey, and N. A. Dinkel, "A ten-element array of individually addressable channeled-substrate-planar AlGaAs diode lasers," IEEE J. Quantum Electron. QE-23, 476, May 1987.
8. D. B. Carlin, G. N. Pultz, and B. Goldstein, "0.87 μm CSP diode lasers for spaceborne communications," SPIE Vol. 756, Optical Technologies for Space Communication Systems, Los Angeles, CA, January 1987.
9. G. A. Evans, J. K. Butler, and V. Masin, "Lateral optical confinement of AlGaAs channeled-substrate-planar lasers," to be published in IEEE J. Quantum Electron.
10. J. D. Barry, "Design and system requirements imposed by the selection of GaAs/GaAlAs single mode laser diodes for free space optical communications," IEEE J. Quantum Electron. QE-20 478, 1984.
11. G. A. Evans and M. Ettenberg, "Semiconductor laser sources for satellite communications," in Laser Satellite Communications, ed. M. Katzman, Prentice-Hall, 1986.

12. K. M. Leung and S. R. Lange, "Wavefront evaluation on laser diodes using a phase measurement interferometer," Proc. SPIE, vol. 429, 27, 1983.

13 J. Hayes and S. R. Lange, "A heterodyne interferometer for testing laser diodes," Proc. SPIE, vol. 429, 22, 1983.

14 N. W. Carlson and V. J. Masin, IEEE J. Quantum Electron. QE-22, 2079, 1986.

15 S. Yamamoto, H. Hayashi, T. Hayakawa, N. Miyauchi, S. Yano, and T. Hijikata, "High power cw operation in visible spectral range by window V-channeled substrate inner stripe lasers," Appl. Phys. Lett. 42, 5, 406-408, March 1983.

16 Y. Mihashi, Y. Nagai, H. Matsubura, amd K. Ikeda, "A novel self-aligned laser with small astigmatism grown by MO-CVD," 17th Conference on Solid State Devices and Materials, Tokyo, 1985, pp. 63-66.

17. T. Murakami, K. Ohtaki, H. Matsubara, T. Yamawaki, H. Saito, K. Isshiki, Y. Kokubo, A. Shima, H. Kumabe, and W. Susaki, "A very narrow-beam AlGaAs laser with a thin-tapered-thickness active layer (T^3 laser)," IEEE J. Quantum Electron. QE-23, 712, June 1987.

18. T. Shibutani, M. Kume, K. Hamada, H. Shimizu, K. Itoh, G. Kano, and I. Teramoto, "A novel high-power laser structure with current-block regions near cavity facets," IEEE J. Quantum Electron. QE-23, 760, June 1987.

Appendix A

Lateral Optical Confinement of AlGaAs Channeled-Substrate-Planar Lasers[a]

Gary A. Evans, Jerome K. Butler,[b] and Valerie J. Masin [c]

David Sarnoff Research Center

CN 5300

Princeton, NJ 08543-5300

ABSTRACT

A physical explanation is presented of the lateral guiding mechanism in Channeled-Substrate-Planar (CSP) lasers based on the amount of wavefront tilt of the transverse mode outside the channel region. Because of this inherent wavefront tilt, all CSP lasers will have a slight asymmetry in their transverse far-field pattern. The nature of the lateral guiding does not require light absorption by the substrate. Design curves showing the complex lateral effective index step as a function of n-clad thickness with the active layer as a parameter are also presented. The CSP guiding mechanism provides a positive lateral index step for substrates (or buffer/blocking layers) with mole fractions of AlAs between 0 and 0.30.

---

[a]This work was supported in part by NASA, Langley Research Center, Hampton, VA, under Contract No. NAS1-17441.

[b]Southern Methodist University, Dallas, TX 75275.

[c]TASC, 55 Walkers Brook Drive, Reading, MA 08167.

Lateral Optical Confinement of AlGaAs Channeled-Substrate-Planar Lasers[a]

Gary A. Evans, Jerome K. Butler,[b] and Valerie J. Masin [c]
David Sarnoff Research Center
CN 5300
Princeton, NJ 08543-5300

INTRODUCTION

Channeled-Substrate-Planar (CSP) AlGaAs/GaAs semiconductor lasers are important commercial products and have been extensively studied both experimentally and theoretically [1-11]. CSP lasers have single spatial mode output powers as high as any single element semiconductor laser [4,5] and have demonstrated long life at very high power [6]. They have been used in conventional [12,13] arrays and Y-guide arrays [14,15]. Originally grown by liquid phase epitaxy (LPE) on n-type [1] and later p-type [2] GaAs substrates, functionally equivalent structures are also grown by metalorganic chemical vapor deposition (MOCVD) [16,17] and molecular beam epitaxy (MBE) [18,19]. Although GaAs substrates with GaAs buffer layers have been predominantly used for CSP lasers, AlGaAs buffer layers have also been used [13,20]. This paper analyzes the modal characteristics of these recent devices.

The waveguiding mechanism of this extensively researched and highly developed laser structure (Fig. 1a) has not been previously explained in physical terms, although theoretical analyses [7-11] agree that lateral mode confinement results from the

[a]This work was supported in part by NASA, Langley Research Center, Hampton, VA, under Contract No. NAS1-17441.

[b]Southern Methodist University, Dallas, TX 75275.

[c]TASC, 55 Walkers Brook Drive, Reading, MA 08167.

combination of a positive real index guide (Fig. 1b) parallel to the junction, with high losses (related to a large imaginary component of the effective index) in the region outside the channel (Fig. 1c). This resulting complex effective index profile provides mode confinement parallel to the junction. In this paper, we give a simple physical explanation of why the real effective index is depressed on either side of the channel.

Growth of CSP lasers on AlGaAs substrates or AlGaAs buffer layers is also of interest to prevent meltback of the channel profile during the growth of both single devices and arrays [13], to prevent meltback of a grating incorporated in the structure that provides distributed feedback (DFB) [20], and to provide a transparent window for junction-down mounting of grating surface emitting lasers [21]. In addition, we speculate that AlGaAs buffer layers may be a more effective current blocking layer than the usual GaAs blocking layers [2, 16] and may even reduce local heating. In this paper, we show that in CSP lasers emitting at ~ 0.8 μm, a real positive index step is provided even if the substrate (or buffer/blocking layer) has a mole fraction of AlAs approaching 0.3. This analysis also shows that light absorption by the substrate is not required for guiding in the CSP structure.

THE EFFECTIVE INDEX METHOD

The analysis of the near- and far-fields of laser structures can be accomplished using the effective index method as discussed extensively in the literature [22]. The analysis of the lateral modes (along the y-direction) uses the effective index obtained from calculations of the transverse modal field. We assume the fields are written as

$$E_y = E_o\, u(x,y)\, v(y)\, \exp(j\omega t - \gamma z) \qquad (1)$$

where $\gamma = \alpha + j\beta$ is the complex modal propagation constant. The quantity u(x,y) is the transverse field function and is a solution of the wave equation

$$\partial^2 u/\partial y^2 + [\gamma_o(y)^2 - k_o^2\, \kappa(x,y)]\, u = 0 \qquad (2)$$

where $\kappa(x,y)$ is the layer dependent complex relative electric permittivity, $\gamma_o(y) = \alpha_o(y) + j\beta_o(y)$ is the transverse complex propagation constant, and k_o is the free-space wavenumber. Assuming the top p-clad layer > 1.0 μm in thickness, the transverse modes can be determined from a solution of the four-layer waveguide shown in Fig. 2. The secular equation for the modes in the four-layer waveguide is

$$[(r^2 - q^2) \tan rd_2 - 2qr] (p + q) \exp(qd_2) + [(r^2 + q^2) \tan rd_2] (p - q) \exp(-qd_2) = 0 \quad (3)$$

where

$$r^2 = [\gamma_o^2 + k_o^2 \kappa_2] \quad (4a)$$

$$q^2 = - [\gamma_o^2 + k_o^2 \kappa_i], \quad i = 1,3 \quad (4b)$$

$$p^2 = - [\gamma_o^2 + k_o^2 \kappa_4] \quad (4c)$$

We have assumed for proper modes, i.e., modes that decay exponentially as $|x| \rightarrow \infty$, that Re {p} and Re {q} > 0. Generally the solutions are complex and the fields in the substrate are damped sinusoidal functions as shown in Fig. 3. The solutions for the transverse field functions u(x,y) are obtained in both the channel region ($|y| < W/2$) and the wing region ($|y| > W/2$) by matching the fields and their derivatives at the three interfaces located at x = 0, d_2, and d_3; W is the channel width. The lateral field functions v(y) are computed after the complex effective index profile $n_{eff}(y) = -j\gamma_o(y)/k_o$ is determined. In the analysis of the transverse mode functions, we assume the absorption losses in the p-cladding, active layer, and n- cladding layers have values $\alpha_1 = 10\ cm^{-1}$, $\alpha_2 = 200\ cm^{-1}$, and $\alpha_3 = 10\ cm^{-1}$. (The actual value of loss (or gain) in the active layer has an insignificant effect on the value of the complex effective index. However, the lateral distribution of the gain in the active layer above threshold is very important in determining the optoelectronic characteristics of the device[10]). The Al content of the active layer is 7% so that the

lasing wavelength λ_o is 0.83 μm. The Al content of the cladding layers is 33% while the Al content of the substrate (normally 0% for CSP lasers), is varied from 0 to 40%. This variation allows for a study of the coupling of light from the lasing region to the substrate. Because the mole fraction of AlAs in the substrate is variable, the value of the substrate absorption coefficient (at $\lambda = 0.83$ μm) ranges from about 10,000 cm^{-1} (p-type GaAs substrate) or 5,000 cm^{-1} (n-type GaAs substrate) [23] down to 10 cm^{-1} as the mole fraction of AlAs in the substrate increases beyond 0.10. A material absorption value of 10 cm^{-1} is nominally assigned to the cladding layers and the AlAs containing substrates to account for free-carrier losses.

The far-field intensity pattern is found from the two dimensional Fourier transform of the aperture field distribution and the obliquity factor [32] $g(\theta)$. The two dimensional Fourier transform of the aperture field at the laser facet lying in the $z = 0$ plane is

$$F(k_x, k_y) = Eo \int_{-\infty}^{\infty} \int_{-\infty}^{\infty} u(x,y)\ v(y)\ \exp[jk_x x + k_y y]\ dxdy \qquad (5)$$

where $k_x = k_o \cos\phi \sin\theta$ and $k_y = k_o \sin\phi \sin\theta$ and r, θ, and φ are the observation point coordinates in the far-field defined by $z = r\cos\theta$, $x = r\sin\theta$, and $y = r\sin\theta\sin\phi$. The transverse radiation pattern is obtained by placing $\phi = 0$ and varying θ. The lateral pattern is obtained by placing $\theta = \pi/2$ and varying φ.

Since we are focusing our attention on the transverse patterns, we place $\phi = 0$ so that

$$F(k_x,0) = \int_{-\infty}^{\infty} \int_{-\infty}^{\infty} u(x,y)\ v(y)\ \exp[jk_x x + k_y y]\ dxdy \qquad (6)$$

represents an "average transform" of the transverse field function u(x,y) where v(y) is the weighting term. In the special case of a square channel CSP, the function u(x,y) can be

written

$$u(x,y) = \begin{cases} u(x)_{ch}, & |y| < W/2 \\ u(x)_{w}, & |y| > W/2 \end{cases} \tag{7}$$

For this case, Eq. (6) reduces to:

$$F(k_x,0) = F_{ch}(\theta)\,\zeta_{ch} + F_w(\theta)\zeta_w \tag{8}$$

where

$$F_i(\theta) = \int_{-\infty}^{\infty} u_i(x)\exp[jk_x x]dx, \quad i = \text{channel, wing} \tag{9}$$

and

$$\zeta_{ch} = \int_{-W/2}^{W/2} v(y)dy \Big/ \int_{-\infty}^{\infty} v(y)dy \tag{10a}$$

$$\zeta_w = 2\int_{W/2}^{\infty} v(y)dy \Big/ \int_{-\infty}^{\infty} v(y)dy \tag{10b}$$

Thus the transverse far-field radiation pattern perpendicular to the junction $I_{\perp}(\theta) = |g(\theta)|^2 F(k_x,0)F^*(k_x,0)$ for the square channel CSP laser can be written as

$$I_{\perp}(\theta) = I_{ch}(\theta)\,|\zeta_{ch}|^2 + I_w(\theta)|\zeta_w|^2 + 2\,|g(\theta)|^2\,\mathrm{Re}[F_{ch}(\theta)F_w(\theta)\zeta_{ch}\zeta_w] \quad (11)$$

where $I_{ch}(\theta) = |g(\theta)|^2 F_{ch}(\theta)F_{ch}^*(\theta)$ and $I_w(\theta) = |g(\theta)|^2 F_w(\theta)F_w^*(\theta)$. ζ_{ch}, the fraction of the lateral field confined to the channel, is generally large. For the conventional CSP laser described in Table 1, $|\zeta_{ch}|^2$ ranges from 0.97 to 0.99 for channel widths of 4 to 6 μm. Therefore the transverse far-field pattern of the laser will be almost totally determined by the Fourier transform of the transverse field in the channel region.

LATERAL OPTICAL CONFINEMENT

Based on intuition for bound modes in dielectric waveguides, one expects that the CSP geometry has a larger effective index (real part) in the region outside the channel since a significant portion of the perpendicular field distribution there "averages in" the high index of the GaAs substrate. In addition, one expects that the losses outside the channel region are due to the high substrate losses (because α_4 = 5000 - 10000 cm^{-1} [23] at a lasing wavelength of 0.83 microns) by the GaAs substrate . However, analysis of the CSP structure indicates that the effective index (real part) is higher inside the channel than outside (producing a positive index step and corresponding bound lateral modes), and the mode loss outside the channel region increases as the substrate absorption is decreased.

The reason for these apparent contradictions is that the transverse mode in the regions outside the channel is almost a leaky mode [24] rather than the conventional bound mode. The conventional bound mode of a passive dielectric waveguide has decaying exponential field solutions in the first and last (the outermost, semi-infinite) layers. A leaky mode has sinusoidal solutions with exponential growth in one or both of the outermost layers. When the outermost layers have sufficient loss, the field solution is an "almost" leaky mode because the fields exponentially decay due to the absorption. In addition, bound modes have normalized transverse propagation constants β_o/k_o that are greater than the refractive indices of the outermost layers, whereas the almost leaky modes have normalized propagation constants less than the refractive index of one (or both) outermost

layers.

Examples of structures that support bound modes perpendicular to the junction are double heterostructure (DH) (exponential solutions in the p- and n-clad layers, sinusoidal solutions in the active layer) and Large Optical Cavity (LOC) (exponential solutions in the p- and n-clad layers, sinusoidal solutions in the active and waveguide layers) geometries.

In Fig. 3, the index of refraction profile of the layers outside the channel region is shown superimposed on a plot of the real (3a) and imaginary (3b) parts of the electric field for the fundamental mode. The magnitude (3.4163) of the normalized longitudinal propagation constant β_o/k_o (at $y > W/2$) for the fundamental mode, also shown in Fig.3, corresponds to sinusoidal solutions in both the active layer and the substrate. The oscillatory behavior of the fields for $x > 0.36$ is characteristic of a leaky mode. In the channel region, the mode perpendicular to the junction is also, strictly speaking, an almost leaky mode, but the electric field is so isolated from the substrate by the thick n-clad region that the amplitude of the field oscillations in the substrate are negligible (see Fig. 3 of reference [11]).

Figure 4 shows the near-field intensities (4a) and near-field phases (4b) for the modes perpendicular to the junction in both the regions inside and outside the channel for a CSP structure with $d_2 = 600$ Å and $\alpha_4 = 10{,}000\text{cm}^{-1}$. Note that the wavefront is tilted at 1.03^o for $-1.5 < x < 0.0$ microns and is tilted at about 20.21^o for $x > 0.3$ microns for the mode in the regions outside the channel. Since the direction of wave propagation is perpendicular to the wavefront, the wave outside the channel is therefore tilted away from the z-axis of the waveguide and is radiating some energy into the substrate. As the wavefront tilt increases, the guide wavelength λ_z increases (see Fig. 5). Correspondingly, the propagation constant ($\beta = 2\pi/\lambda_z$) and the effective index ($n_{eff} = \beta/k_o$) decrease.

If we assume that the guide wavelength (λ_z) does not change for the fundamental mode perpendicular to the junction whether it is inside or outside the channel, we can calculate the average tilt angle of the leaky mode from (see Fig. 5)

$$\theta = \cos^{-1}[\lambda_z/\lambda_p] = \cos^{-1}[\beta_o(y=0)/\beta_o(y>W/2)] \qquad (12)$$

For a structure with d_2 = 600 Å and α_4 = 10,000cm^{-1}, β_o/k_o (at y = 0) = 3.42315, and β_o/k_o (at y > W/2) = 3.41656 which results in a tilt angle of 3.6° using Eq. (12).

From curves such as Fig. 4b, a plane wave equivalent tilt Θ can be calculated between any two points x_1 and x_2 with corresponding phases (in degrees) $\Phi(x_1)$ and $\Phi(x_2)$ from

$$\Theta = \tan^{-1}\frac{[\Phi(x_1) - \Phi(x_2)]\lambda_o}{360\, n_{eff}\,[x_1 - x_2]} \qquad (13)$$

Indicated in Fig. 4b are plane wave equivalent tilts between the region of nonzero intensity (-1.0 < x < 1.0) of 8.45°, between the $1/e^2$ points in intensity of 2.40°, and between the half power points of 1.6°. Another indication of average tilt of the wavefront can be obtained from the calculated shift of the peak of the far-field intensity pattern (corresponding to the "wing" region, |y| > W/2) which is offset from 0° because of radiation into the substrate [11,25,26]. For the mode perpendicular to the junction outside the channel region, the calculated shift in the far-field peak is 4.0° in air (Fig. 4c), and therefore about 1.2° in the structure.

As a further illustration of the guiding mechanism, three structures are considered in Table 1. All three models have the same dimensions: a 600 Å active layer, 1.5 μm channel depth, and a 0.3 μm thick n-clad in the "wing" regions (|y| > W/2). The first model (CSP) is that of a real CSP with losses of 10,000 cm^{-1} (5,000 cm^{-1}) in the GaAs substrate. The second model (CSPNL) is the same as the first model, except that there are no losses in the GaAs substrate. The third model (CSPNIC) is the same as the first model except that the "substrate" has the same AlAs composition as the n-clad layer (no index change between the n-clad and the substrate). The last two models are not physical, but are pedagogically chosen to show the various effects of leaky modes and substrate absorption on the complex effective index that provides lateral confinement in a CSP laser. The parameters listed in

Table 1 are the real and imaginary parts of the lateral complex effective index step, and for both inside and outside the channel, the normalized longitudinal propagation constant and full width half power (FWHP) of the transverse beam divergence. The transverse confinement is due to the difference Δn and $\Delta\alpha$ in the real and imaginary parts of the complex effective index (γ_o/k_o) between the channel and wing region.

The near-field intensities, phases, and far-field intensities in the channel region are nearly identical for all three cases. However, the near-field intensities in the wing region, plotted in Fig.6a differ, primarily for $x > 0.36$, where the bound mode (CSPNIC) is the strongest damped, the CSP leaky mode is moderately damped, and the CSPNL leaky mode is undamped. The near-field phases in the wing region are plotted in Fig. 6b. They are similar for the CSP and CSPNL cases, with the CSPNL case having slightly more tilt for $x > 0.36$. The near-field phase of the CSPNIC has considerably less tilt than the other cases. The far-field intensities corresponding to the near-field in the wing region are shown in Fig. 6c. The far-field peaks are all shifted from 0^o to about 4^o. Because the far-field pattern in the transverse direction obtained from either Eq. (6) or (11) is due to the field in the channel and wing regions, the asymmetries in the far-fields produced by the wing regions will always add a slight asymmetry to the far-field produced by CSP lasers. Although these equations also hold for other laser geometries such as the ridge guide, the transverse fields inside and outside the ridge both have symmetric transforms, and therefore ridge (and most other) laser structures should have symmetric transverse far-field patterns.

Of the three models, the first two (CSP and CSPNL) give almost identical results, with the "no loss" model having a slightly larger complex effective index step. The third has less than half the complex effective index step of the other two models for a substrate loss of 10,000 cm^{-1}. If the substrate absorption is 5000 cm^{-1}, the result is a positive index step of only 1.25×10^{-3} for the CSPNIC model, which is comparable to the amount of gain induced index depression [27] expected at threshold.

These results are anticipated since from Fig. 6a the CSPNL structure has a larger fraction of the mode intensity in the substrate, has slightly more tilt in the near-field phase, and has slightly more off-axis tilt in the far-field than the CSP case. As the substrate absorption is decreased, more energy is radiated into the substrate resulting in an increased average wavefront tilt, and therefore both the positive index step and the mode absorption in the region outside the channel increases. Another way to view the increasing mode loss with decreasing substrate absorption is that the "skin depth" of the almost leaky mode increases as the substrate becomes less like a perfect conductor (which requires that the field be zero at the boundary). This effect is slight, however. Table 1 shows that the mode loss and the lateral index step only increase by about 13% and 8% as the substrate absorption decreases from 10,000 cm^{-1} to 0.

CSP Design Curves

Figure 7a is a plot of the real part of the effective index for the mode perpendicular to the junction as a function of the n-clad thickness (d_3 in Fig. 2) for active layer thicknesses of 300, 400, 600, 800, and 1000 Å. For a CSP laser to have stable near- and far-field patterns with increasing drive current, the lateral index step should be large compared to index variations due to gain. The gain induced index depression will typically reduce the index of refraction of the active layer by 10^{-2}, which in turn reduces the "cold cavity" effective index by about 10^{-3}. For this reason, a "cold cavity" lateral index step greater than 3×10^{-3} is desired to provide lateral mode stability . From Fig. 7, this is obtained for n-clad thicknesses (outside of the channel) of 0.3 μm or less for channel depths greater than 1.0 μm.

Figure 7b is a plot of the imaginary part of the effective index, which increases with decreasing cladding thickness. The resulting magnitudes of the real and imaginary parts of the lateral effective index step for a CSP are always the same order of magnitude. Although a large imaginary component of the effective index is beneficial for stability of

single laser diodes, it is detrimental to the operation of coherent CSP arrays in the fundamental array mode [28,29].

Figure 8 is a plot of the active layer confinement factor as a function of the n-clad thickness (d_3) for active layer thicknesses (d_2) of 300, 400, 600, 800, and 1000 Å.

AlGaAs Substrates for CSP Lasers

The use of an AlGaAs substrate or a thick AlGaAs buffer layer is often desirable: Since AlGaAs has less meltback during LPE growth than GaAs, an AlGaAs layer is preferred for fabricating gratings for distributed feedback CSP lasers [20]. The reduced meltback can also aid in maintaining the dimensions of the channel and the n-clad thickness. Due to a shorter diffusion length of minority carriers, an AlGaAs buffer layer could also be a more effective current blocking layer than conventional GaAs blocking layers [2]. In addition, some surface emission devices such as the CSP-LOC-DBR [21] could be made more efficient if the lasing light was extracted through a transparent substrate.

Plots of the real and imaginary parts of the effective index for a standard CSP geometry laser with a 600Å active layer, but with a substrate composition of 0, 10, 20, 30, and 40% AlAs are shown in Fig. 9. The behavior of the curves for 10 and 20% AlAs have the same explanation as the effective index curves for CSP lasers on GaAs substrates: the real part of the effective index is lower outside the channel region because of the wavefront tilt. Although this tilt is the dominant mechanism and is responsible for the lower index outside the channel, there is less of an index step as the Al increases from 0 to 20% in the substrate. The reason for this is that λ_z (see Fig. 5) in the region outside the channel is reduced as the index of the substrate decreases--the same behavior one expects for a conventional bound mode--causing the real part of the effective index to increase.

For a fixed n-clad thickness, for example 0.3 μm, and for mole fractions of AlAs below about 30%, the transverse mode losses increase with increasing mole fraction of

AlAs in the substrate. This can be explained by increased coupling of the mode energy to the substrate as the index of the substrate approaches the value of the normalized transverse mode propagation constant β_0/k_0. This increased coupling of energy to the substrate is also apparent in Fig. 10a which shows a reduced peak mode intensity with increased mode intensity in the substrate; in Fig. 10b, which shows the near-field phase; and in Fig. 10c which shows an increasing tilt of the far-field patterns as the mole fraction of AlAs increases. Because of the increased mode penetration (increased "skin depth") of the leaky mode into the substrate with increasing mole fraction of AlAs, the local heating at the channel shoulders [30,31] may be reduced by spreading the absorption of the optical field further into the substrate.

As the mole fraction of AlAs in the substrate approaches 30%, the index in the substrate becomes close to the value of the normalized transverse mode propagation constant β_0/k_0 in both regions. Table 2 lists the applicable parameters for a CSP laser with an AlAs mole fraction of 0.30 in the substrate. For this case, the effective index for the region outside the channel is greater than the index of the substrate, corresponding to a bound mode. Inside the channel, the effective index is less than the index of the substrate, resulting in a leaky mode in the channel region, exactly opposite to a conventional CSP laser. Because the effective index of the (leaky) transverse mode in the channel region is very close to the value of the index of the substrate, the mode energy couples strongly to the substrate. This strong coupling is analogous to impedance matching in a transmission line, and is similar to the effect of enhanced coupling of mode energy to the substrate by nonuniformities in the Al composition in the channel region of a CSP laser [11]. Although this strong coupling is not apparent in the near-field intensity (Fig. 11a), the near-field phase (Fig. 11b) shows a wavefront tilt of 2.8° for $x > 1.5$ μm. In addition, the far-field pattern (Fig. 11c) corresponding to the channel region is characteristic of strong coupling of mode energy to the substrate--the pattern is asymmetric and tilted 2.5 degrees towards the substrate. For the 30% case, Fig. 9b indicates a highly resonant region (for n-clad

thicknesses $0.4 < d_3 < 1.0$) in which the "average wavefront tilt" argument no longer properly predicts the index step. Again, the assumption that λ_z (Fig. 5) remains unchanged by the tilt is no longer the case. In fact, in this case the change in λ_z more than offsets the wavefront tilt. λ_z decreases (the effective index increases) because n_4 is greater than n_3 and the substrate confinement factor is very large (increasing from 0.19 to 0.95 as d_3 decreases from 1.0 to 0.4). Figure 12, which plots the active layer confinement factor for the cases shown in Fig. 9, shows a large decrease in the active layer confinement factor over the same range in d_3.

As the n-clad thickness decreases even further (below about 0.35 μm), the mode becomes a conventional bound mode and the effective index of the mode continues to increase because an increasing fraction of the mode energy is in the (slightly) higher index substrate. In Fig. 9b, the losses for the 30% case increases as the n-clad thickness decreases, until the mode changes from a complex mode into a conventional bound mode and the losses approach zero (background).

Table 3 lists the applicable parameters for a CSP laser with a 0.40 mole fraction of AlAs substrate. In this case, both the mode inside the channel and outside the channel are conventional modes. The effective index curve decreases with decreasing n-clad thickness because the mode energy outside the channel is "averaging in" the lower clad index--just as in any ridge guide structure. The near-and far-fields for this case are shown in Fig.13 a and b. Both inside and outside the channel, the modes are bound modes with flat phase fronts.

Although the large imaginary part of the effective index outside the channel region of a CSP laser helps stabilize the mode, it also increases the threshold current and decreases the differential quantum efficiency. Using the computational procedure described in reference [10], the power versus current curves for a CSP type laser, a ridge guide laser with cladding layer losses of 10 cm^{-1}, and a lossless ridge guide laser (all with active layer thicknesses of 600 Å) are calculated in Fig. 14. All three structures have the same lateral

index step (6.822×10^{-3}) and profile (see inset of Fig. 14) with a channel or ridge width of 4 μm. The large differences in threshold current and differential quantum efficiency are due to the reduced losses outside the ridge of the two ridge structures compared to the high losses outside the channel for the CSP device. For the devices in Fig. 14, $\Delta\alpha_o/k_o = 0$ for the ridge guide structures and 5.074×10^{-3} for the GaAs substrate CSP laser.

CONCLUSIONS

We have presented a physical explanation of the guiding mechanism in CSP lasers: the lateral index step is determined by (1) the amount of wavefront tilt, and (2) the magnitude of the guide wavelength λ_z. In most cases, the wavefront tilt is the dominate mechanism and slight changes in the magnitude of λ_z explain minor changes in the real part of the lateral index step with changes in the AlAs composition ($0 < x < 0.3$) of the substrate or buffer layer. However, when the normalized transverse propagation constant is very close to the refractive index of the substrate or buffer layer (as in the example of a substrate with an AlAs composition equal to 0.3), a highly resonant condition exists, and the dominate mechanism is the magnitude of the guide wavelength λ_z. This explanation does not require light absorption by the substrate for lateral guiding in the CSP structure.

Because of the contribution of the tilted wavefront in the calculation of the far-field radiation pattern, all CSP lasers will have a slight asymmetry in their transverse far-field pattern.

Design curves which provide the complex lateral effective index step as a function of n-clad thickness with the active layer thickness as a parameter are presented. We also show that the CSP guiding mechanism provides a positive lateral real index step for substrates with mole fractions of AlAs approaching 0.30.

The use of AlGaAs substrates is of interest to prevent meltback of the channel profile during the growth of both single devices and arrays, to prevent meltback of a grating incorporated in the structure to provide distributed feedback (DFB), and to provide

a transparent window for junction-down mounting of grating surface emitting lasers. We speculate that (1) AlGaAs buffer layers may be a more effective current blocking layer than the usual GaAs blocking layers; and (2) AlGaAs buffer layers or substrates may reduce local heating by spreading the optical penetration outside the channel further into the substrate.

ACKNOWLEDGMENTS

The authors gratefully acknowledge technical discussions with N. Carlson, J. Connolly, M. Ettenberg, B. Goldstein, J. Hammer, F. Hawrylo, M. Lurie, R. Martinelli, and S. Palfrey. This paper also benefitted from critical readings and suggestions by M. Ettenberg, J. Hammer, and J. Connolly.

REFERENCES

1. K. Aiki, M. Nakamura, T. Kuroda, J. Umeda, R. Ito, Naoki Chinone, and M. Maeda, "Transverse Mode Stabilized $Al_xGa_{1-x}As$ Injection Lasers with Channeled-Substrate-Planar Structure," IEEE Journal of Quantum Electronics, Vol. QE-14, No. 2, pp.89-94, Feb. 1978.

2. S. Yamamoto, H. Hayashi, S. Yano, T. Sakurai, and T. Hijikata, "Visible GaAlAs V-channeled substrate inner stripe laser with stabilized mode using p-GaAs substrate," Appl. Phys. Lett. Vol. 40, No. 5, pp. 372-374,1 March 1982.

3. S. Yamamoto, N. Miyauchi, S. Maei, T. Morimoto, O. Yamamoto, S. Yano, and T. Hijikata, "High output power characteristics in broad-channeled substrate inner stripe lasers," Applied Physics Letters, Vol.46, No. 4, pp. 319-321, Feb. 15, 1985.

4. K. Hamada, M. Wada, H. Shimizu, M. Kume, F. Susa, T. Shibutani, N. Yoshikawa, K. Itoh, G. Kano, and I. Teramoto, "A 0.2W cw laser with buried twin-ridge substrate structure," IEEE J. Quantum Electron., vol. QE-21, No. 6, pp. 623-628, June 1985.

5. B. Goldstein, M. Ettenberg, N. A. Dinkel, and J. K. Butler, "A high-power channeled-substrate-planar AlGaAs laser," Appl. Phys. Lett. 47, pp. 655-657, Oct. 1, 1985.

6. T. Shibutani, M. Kume, K. Hamada, H. Shimizu, K. Itoh, G. Kano, and I. Teramoto, "A Novel High-Power Laser Structure with Current-Blocked Regions near Cavity Facets," IEEE J. Quan. Electron., Vol. QE-23, No. 6, pp. 760-764, June, 1987.

7. T. Kuroda, M. Nakamura, K. Aiki, and J. Umeda, "Channeled-substrate-planar structure $Al_xGa_{1-x}As$ lasers: an analytical waveguide study," Applied Optics, Vol. 17, No. 20, pp. 3264-3267, 15 October 1978.

8. K. A. Shore, "Above-threshold analysis of channelled-substrate-planar (CSP) laser," IEE Proc. Part I, pp. 9-15, Feb. 1981.

9. S.Wang, C. Chen, A. S. Liao, and L. Figueroa, "Control of Mode Behavior in Semiconductor Lasers," IEEE Journal of Quantum Electron., Vol. QE-17, No. 4, pp. 453-468, April 1981.

10. J. K. Butler, G. A. Evans, and B. Goldstein, "Analysis and Performance of Channeled-Substrate-Planar Double-Heterojunction Lasers with Geometrical Asymmetries", IEEE J. Quan. Electron., (to be published), November 1987.

11. G. A. Evans, B. Goldstein, and J. K. Butler, "Observations and Consequences of Non-Uniform Aluminum Concentrations in the Channel Regions of AlGaAs Channeled-Substrate-Planar Lasers", IEEE J. Quan. Electron., (to be published), November 1987.

12. T. Kadowaki, T. Aoyagi, S. Hinata, N. Kaneno, Y. Seiwa, K. Ikeda, and W. Susaki, "Long-Lived Phase-Locked Laser Arrays Mounted on a Si-Submount with Au-Si Solder with a Junction-Down Configuration" IEEE International Semiconductor Laser Conference, Kanazawa, Japan, Conference Program and Abstract of Papers, pp. 84-85, October, 1986.

13. B. Goldstein, N. Dinkel, N. W. Carlson, G. A. Evans, and V. J. Masin, "Performance of a channeled-substrate-planar high-power phase-locked array operating in the diffraction limit", Conference on Lasers and Electro-Optics, Baltimore, Technical Digest, pp. 330-331, May 1987.

14. M. Taneya, M. Matsumoto, S. Matsui, S. Yano, and T. Hijikata, "0° phase mode operation in phased-array laser diode with symmetrically branching waveguide", Appl. Phys. Lett., Vol. 47, No. 4, pp. 341-343, 15 August 1985.

15. D. F. Welch, P. Cross, D. Scifres, W. Streifer, and R. D. Burnham, "In-phase emission from index-guided laser array up to 400 mW", Electronics Letters, Vol. 22, No.6, pp. 293-294, 13 March 1986.

16. K. Uomi, S. Nakatsuka, T. Ohtoshi, Y. Ono, N. Chinone, and T. Kajimura, "High-power operation of index-guided visible GaAs/GaAlAs multiquantum well lasers," Appl. Phys. Lett. 45 (8), pp. 818-821, 15 October 1984.

17. J. J. Yang, C.S. Hong, J. Niesen, and L. Figueroa, "High-power single longitudinal mode operation of inverted channel substrate planar lasers," J. Appl. Phys., Vol. 58, pp. 4480-4482, Dec. 1985.

18. H. Tanaka, M. Mushiage, Y. Ishida, "Single-Longitudinal-Mode Selfaligned (AlGa)As Double-Heterostructure Lasers Fabricated by Molecular Beam Epitaxy", Japanese Journal of Applied Physics, Vol. 24, No. 2, pp. L89-L90, February 1985.

19. K. Yagi, H. Yamauchi, and T. Niina, "High External Differential Quantum Efficiency (80%) SCH Lasers Grown by MBE", IEEE International Semiconductor Laser Conference, Kanazawa, Japan, Conference Program and Abstract of Papers, p. 158-159, October 1986.

20. B. Goldstein, G. Evans, J. Connolly, N. Dinkel, and J. Kirk, "An Efficient AlGaAs Distributed Feedback Channeled-Substrate-Planar Laser," submitted for publication.

21. G. A. Evans, J. M. Hammer, N. W. Carlson, F. R. Elia, E. A. James, and J. B. Kirk, "Surface-emitting second order distributed Bragg reflector laser with dynamic wavelength stabilization and far-field angle of 0.25°" Appl. Phys. Lett., vol. 49, No. 6, pp. 314-315, 11 August 1986.

22 J. K. Butler and D. Botez, "Mode Characteristics of Nonplanar Double-Heterojunction and Large-Optical-Cavity Laser Structures", IEEE Journal of Quantum Electron., Vol. QE-18, No. 6, pp. 952-961, June 1982.

23. H. C. Casey, Jr., D. D. Sell, and K. W. Wecht, "Concentration dependence of the absorption coefficient for n- and p-type GaAs between 1.3 and 1.6 eV," J. Appl. Phys., Vol. 46, No. 1, pp. 250-257, January 1975.

24. T. Tamir and F. Y. Kou, "Varieties of Leaky Waves and Their Excitation Along Multilayered Structures," IEEE Journal of Quantum Electronics, Vol. QE-22, No. 4, pp. 544-551, April 1986.

25. D. R. Scifres, W. Streifer, and R. D. Burnham, "Leaky wave room-temperature double heterostructure GaAs:GaAlAs diode laser," Appl. Phys. Lett., Vol. 29, No. 1, pp.23-25, July 1976.

26. J. K. Butler, H. Kressel, and I. Ladany, "Internal Optical Losses in Very Thin CW Heterojunction Laser Diodes," IEEE Journal of Quantum Electronics, Vol. QE-11, No. 7, pp. 402-408, July 1975.

27. J. Manning and R. Olshansky, "The Carrier-Induced Index Change in AlGaAs and 1.3 μm InGaAs Diode Lasers," IEEE J. Quan. Electron., QE-19, 10, pp. 1525-1530, October 1983.

28. L. Figueroa, T. L. Holcomb, K. Burghard, D. Bullock, C. B. Morrison, L. M.

Zinkiewicz, and G. A. Evans, "Modeling of the optical characteristics for twin-channel laser (TCL) structures," IEEE J. Quantum Electron., Vol. QE-22, pp. 2141-2149, Nov. 1986.

29. N. W. Carlson, V. J. Masin, M. Lurie, B. Goldstein, and G. A. Evans, "Measurement of the Coherence of a Single-Mode Phase-Locked Diode Laser Array", to appear in Appl. Phys. Lett., August 31, 1987.

30. Satoru Todoroki, Masaaki Sawai and Kunio Aiki, "Temperature Distribution along the striped active region in high power GaAlAs visible lasers," J. Appl. Phys., Vol. 58, pp. 1124-1128, August 1985.

31. S. Todoroki, "Influence of local heating on current-optical output power characteristics in $Ga_{1-x}Al_xAs$ lasers," J. Appl. Phys., Vol. 60, pp. 61-65, July 1986.

32. L. Lewin, "Obliquity-factor correction to solid-state radiation patterns," Journal of Applied Physics, Vol. 46, No. 5, pp. 2323-2324, May 1975.

Table 1. Three Models

	CSP	CSPNL	CSPNIC
d_2	600 Å	600 Å	600 Å
α_4	10,000 cm^{-1} (5000 cm^{-1})	0 cm^{-1}	10,000 cm^{-1} (5000 cm^{-1})
Δn	6.59×10^{-3} (6.82×10^{-3})	7.14×10^{-3}	2.55×10^{-3} (1.25×10^{-3})
$\Delta\alpha/k_o$	4.75×10^{-3} (5.07×10^{-3})	5.37×10^{-3}	2.57×10^{-3} (2.08×10^{-3})
$(\beta/k_o)_{ch}$	3.42315 (3.42315)	3.42315	3.42315 (3.42315)
$(\beta/k_o)_w$	3.41656 (3.41633)	3.41601	3.42061 (3.42190)
FWHP of $I_{ch}(\theta)$	25.18° (25.17°)	25.21°	24.88° (24.73°)
FWHP of $I_w(\theta)$	32.12° (32.21°)	32.40°	30.14° (28.17°)

Table 2. CSP laser with 30% AlAs Substrate

structure	wing parameters (bound mode)	channel parameters (leaky mode)
d_2 = 600 Å	$\beta/k_o = 3.4273$	$\beta/k_o = 3.4232$
n_4 = 3.4270	$\Gamma_1 = 0.16$	$\Gamma_1 = 0.43$
α_4 = 10 cm^{-1}	$\Gamma_2 = 0.06$	$\Gamma_2 = 0.14$
Δn = -4.17×10^{-3}	$\Gamma_3 = 0.18$	$\Gamma_3 = 0.43$
$\Delta\alpha/k_o = 2.32 \times 10^{-6}$	$\Gamma_4 = 0.60$	$\Gamma_4 = 0.0036$

Table 3. CSP laser with 40% AlAs Substrate

structure		wing parameters (bound mode)	channel parameters (bound mode)
d_2	= 600 Å	$\beta/k_o = 3.4209$	$\beta/k_o = 3.4231$
n_4	= 3.364	$\Gamma_1 = 0.51$	$\Gamma_1 = 0.43$
α_4	= 10 cm^{-1}	$\Gamma_2 = 0.15$	$\Gamma_2 = 0.14$
Δn	= 2.21 x 10^{-3}	$\Gamma_3 = 0.32$	$\Gamma_3 = 0.43$
$\Delta\alpha/k_o$	= 0.0	$\Gamma_4 = 0.032$	$\Gamma_4 = 1.15 \times 10^{-5}$

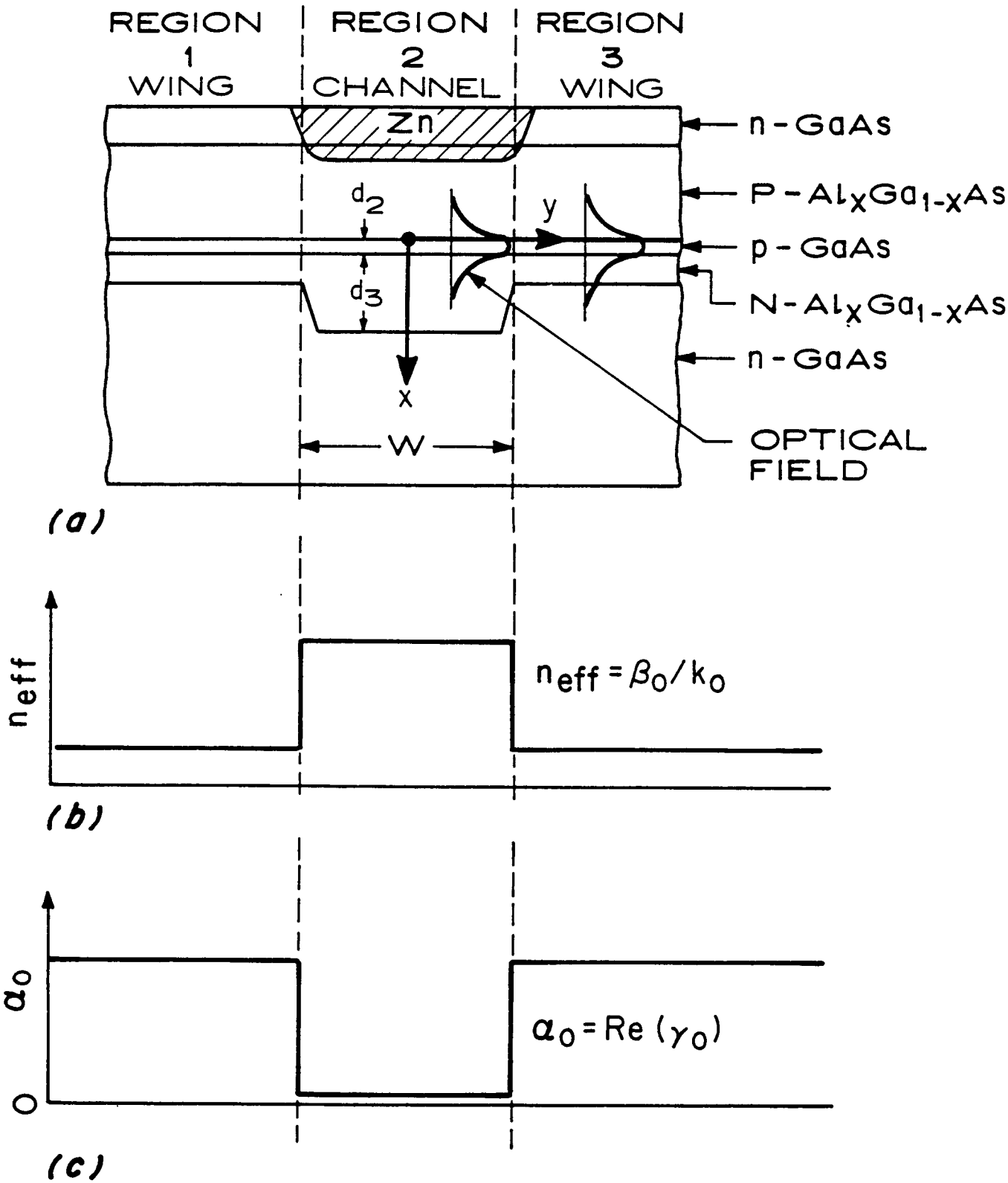

Figure 1. a) Geometry of a CSP laser, b) real part of the lateral effective index profile, and c) imaginary part of the lateral effective index profile.

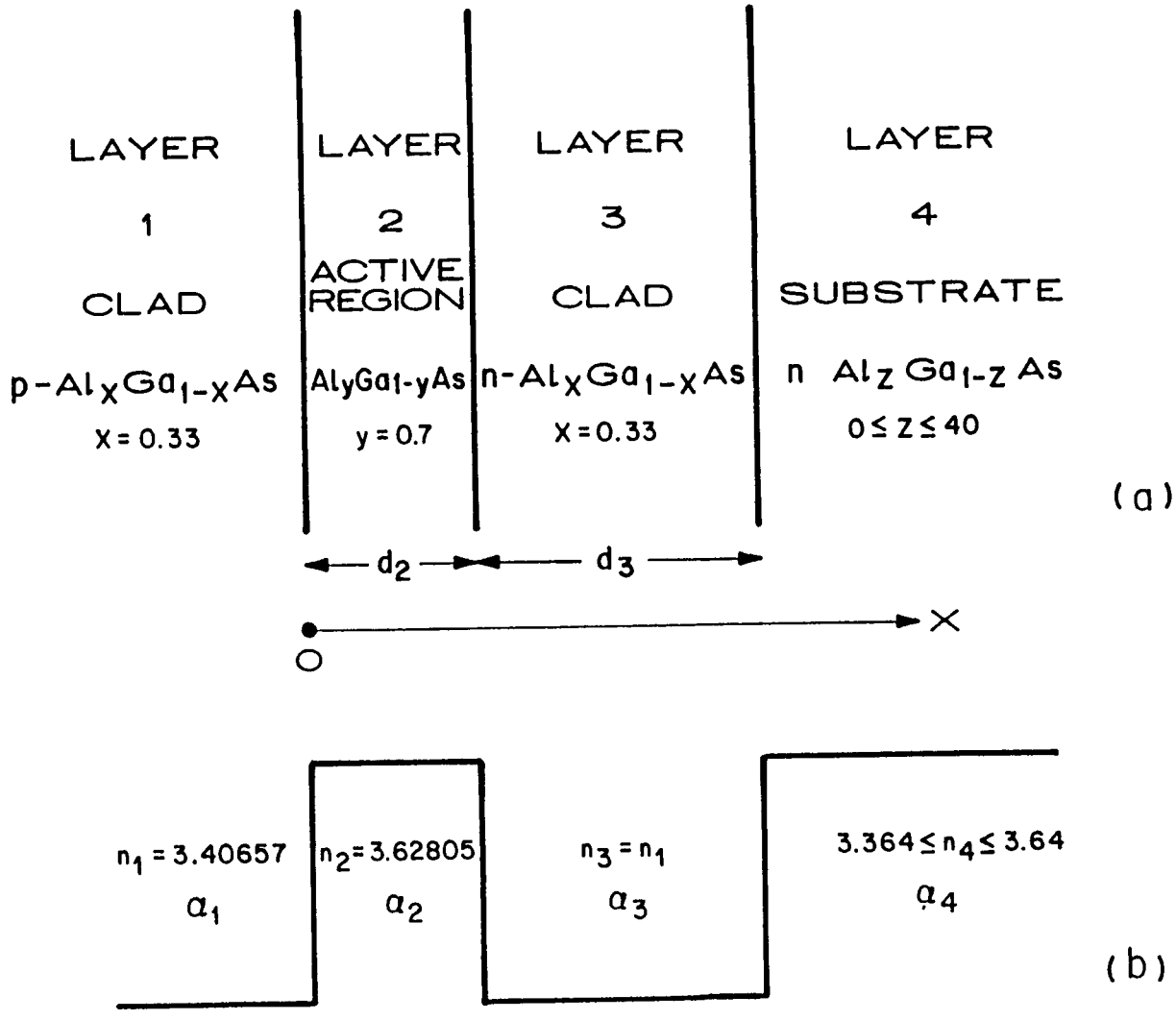

Figure 2. The four-layer waveguide structure with a) the layer geometry and b) the refractive index profile.

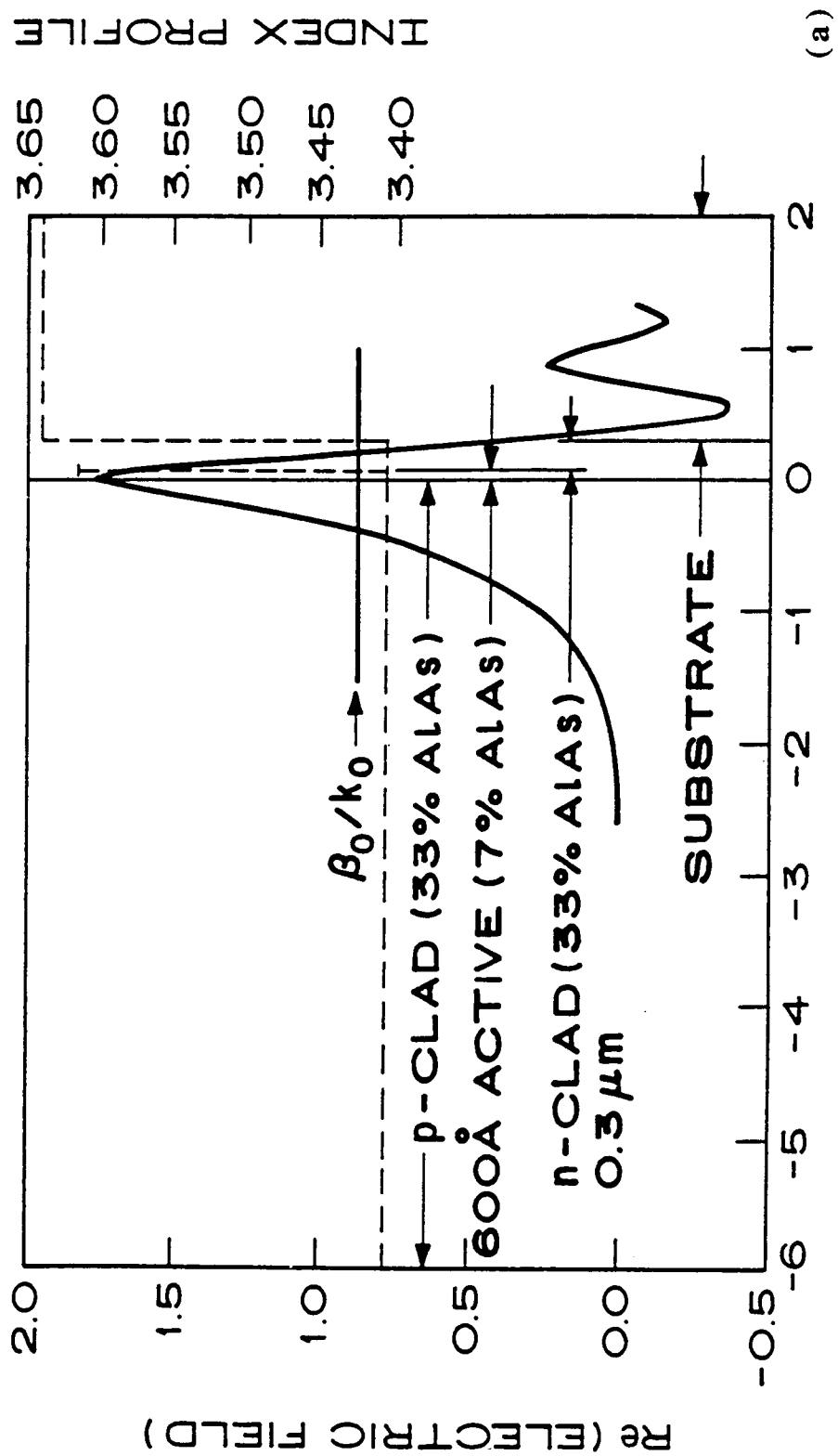

Figure 3. The a) real and b) imaginary part of the electric field distribution for the transverse profile shown in Fig. 2 with d_2 = 600 Å and α_S = 5000 cm^{-1}.

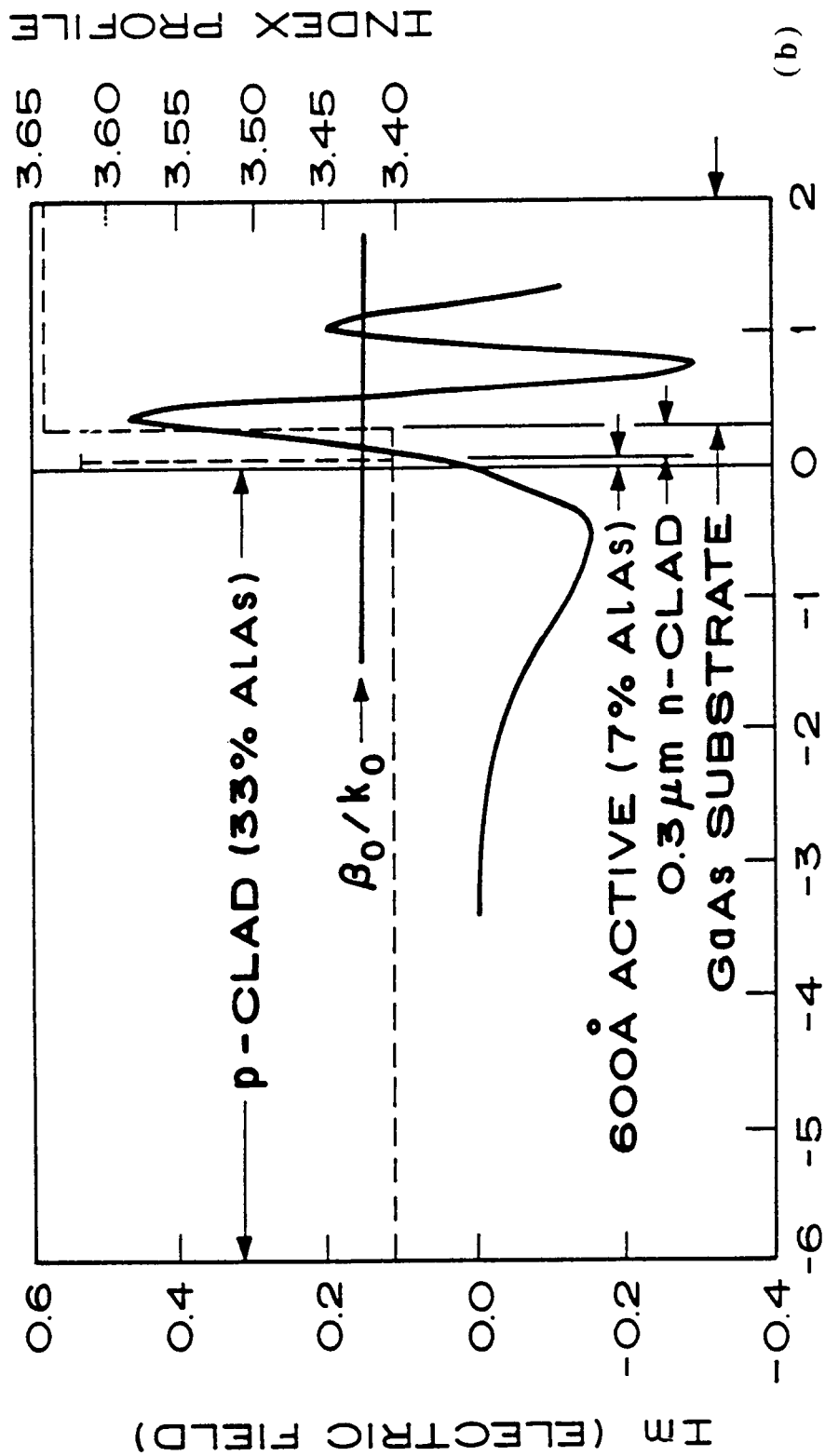

Figure 3. The a) real and b) imaginary part of the electric field distribution for the transverse profile shown in Fig. 2 with d_2 = 600 Å and α_s = 5000 cm^{-1}.

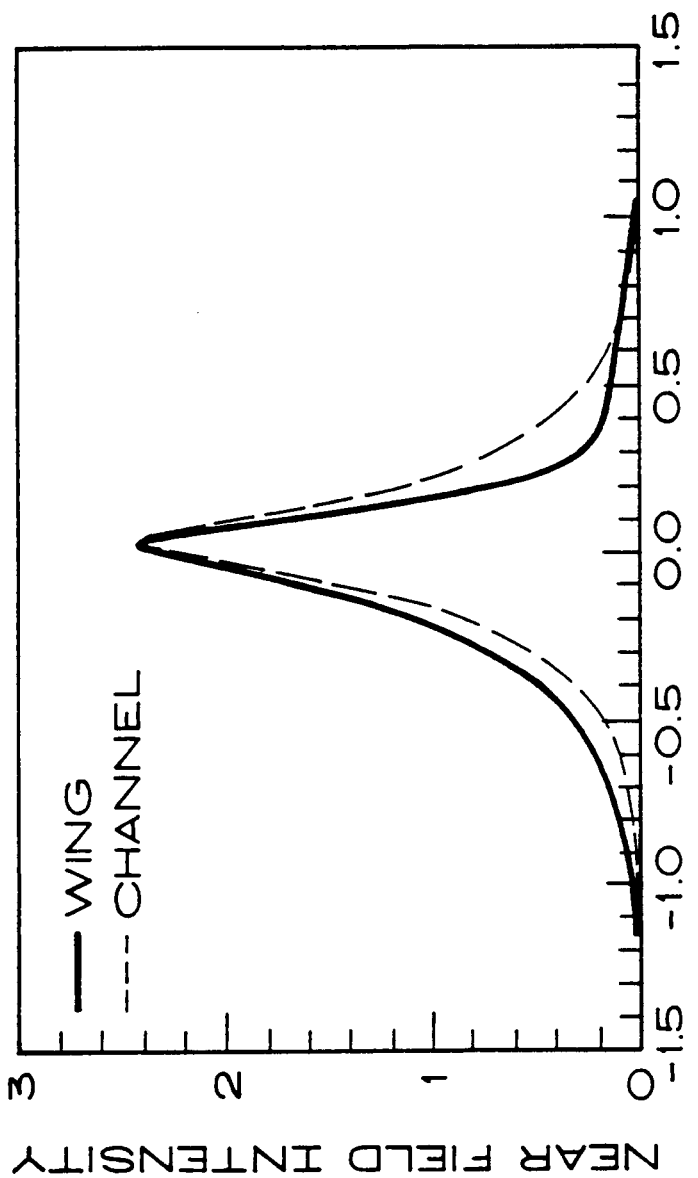

Figure 4. The transverse a) near field intensity, b) near field phase, and c) far field intensity $I_{ch}(\theta)$ and $I_w(\theta)$ for a conventional CSP laser with an active layer thickness of 600 Å in the region inside (——) and outside (---) the channel.

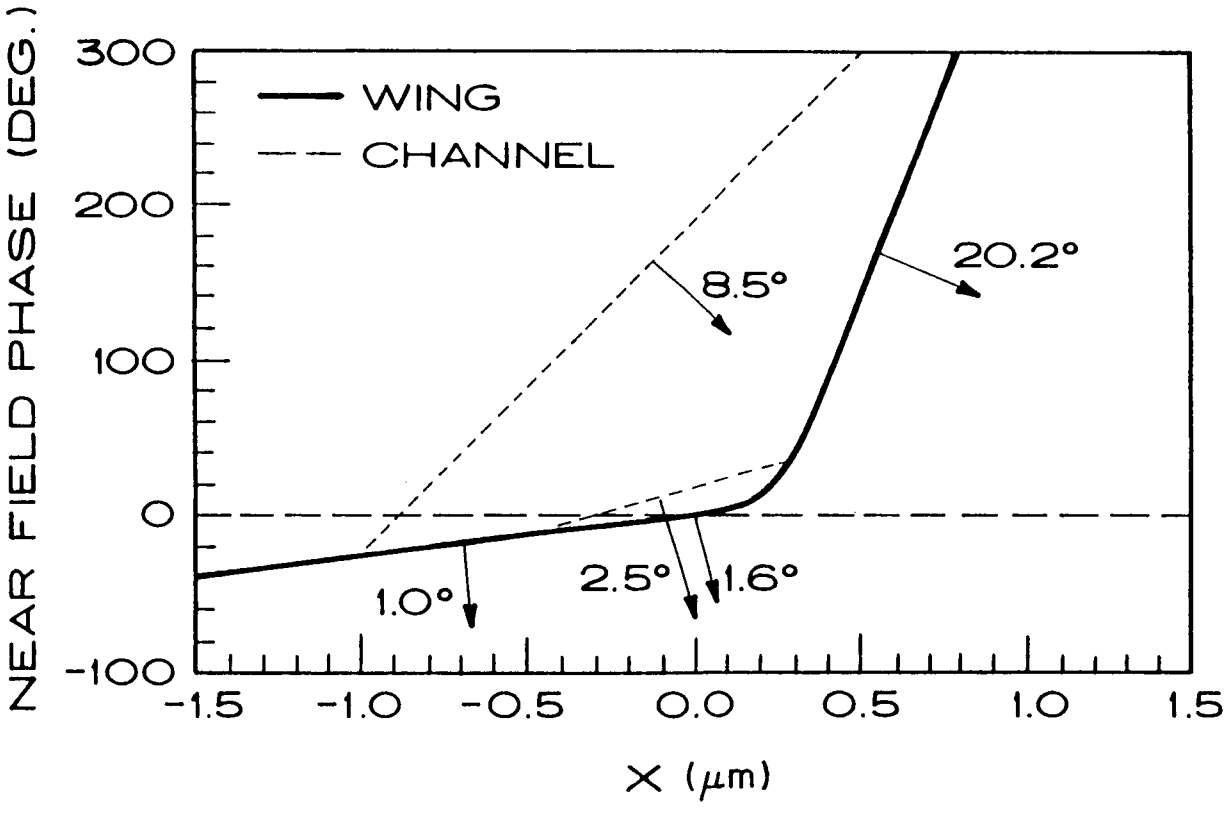

Figure 4. The transverse a) near field intensity, b) near field phase, and c) far field intensity $I_{ch}(\theta)$ and $I_w(\theta)$ for a conventional CSP laser with an active layer thickness of 600 Å in the region inside (——) and outside (----) the channel.

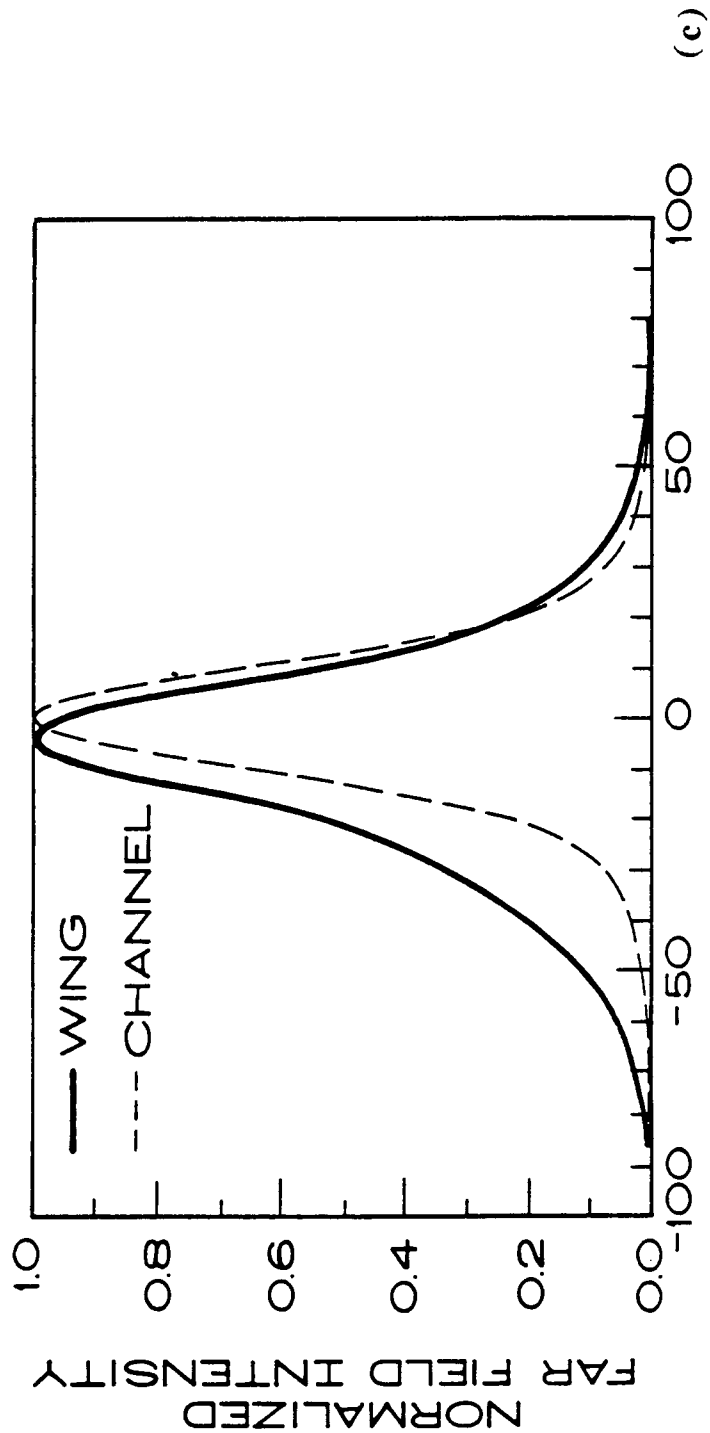

Figure 4. The transverse a) near field intensity, b) near field phase, and c) far field intensity $I_{ch}(\theta)$ and $I_w(\theta)$ for a conventional CSP laser with an active layer thickness of 600 Å in the region inside (——) and outside (----) the channel.

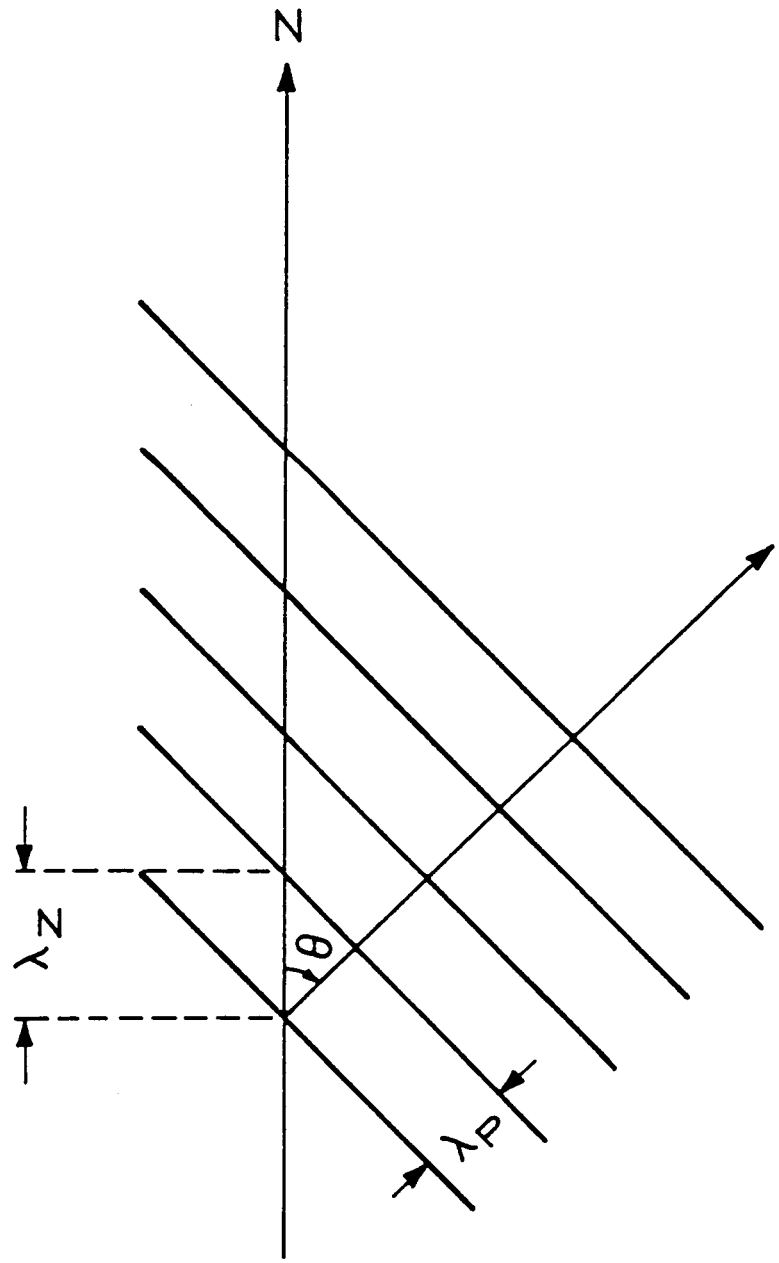

Figure 5. Relationship of the guide wavelength λ_z to the wavelength in the direction of propagation λ_p for a wave propagating at an angle θ with respect to the guide axis.

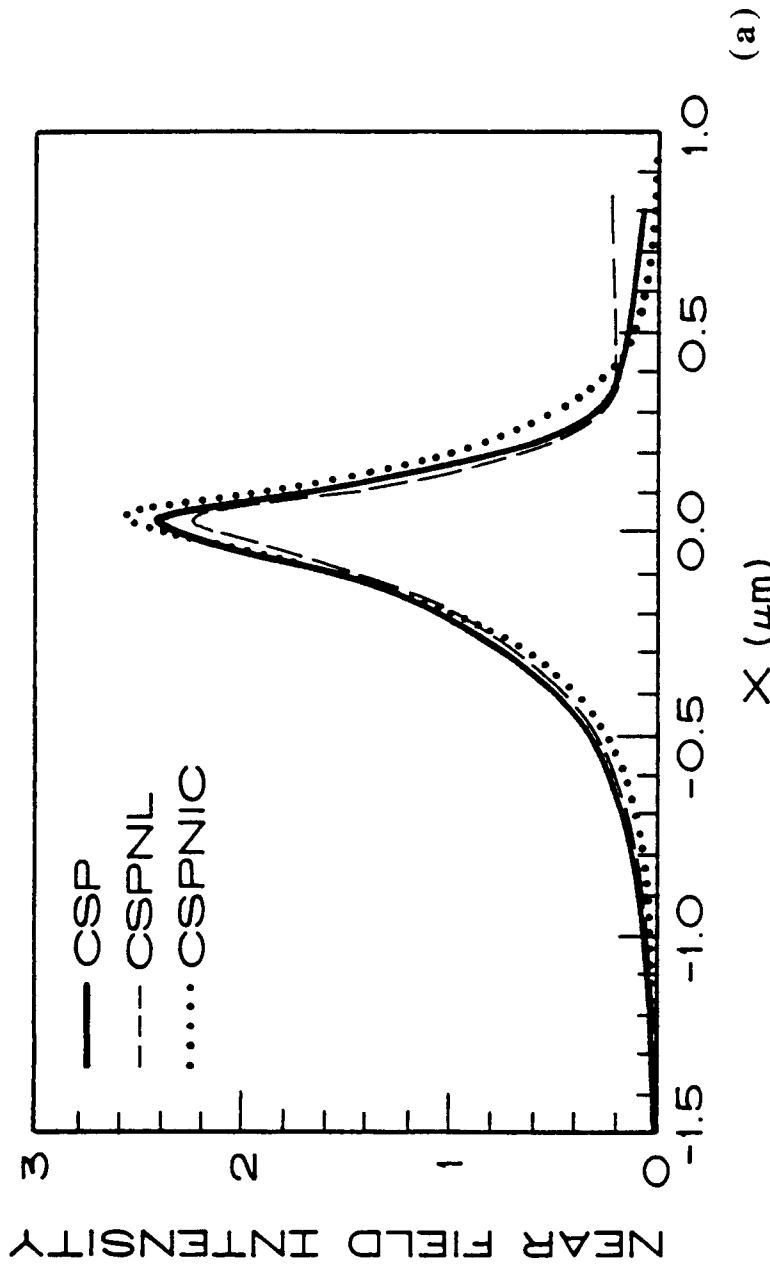

Figure 6. The transverse a) near field intensity, b) near field phase, and c) far field intensity in the region outside the channel region for a conventional CSP laser (—), a CSP laser with no absorption in the GaAs substrate (--) and a structure with the same index in the substrate as the channel region, but with high losses (10,000 cm^{-1}) in the substrate (....). All structures have an active layer thickness of 600 Å.

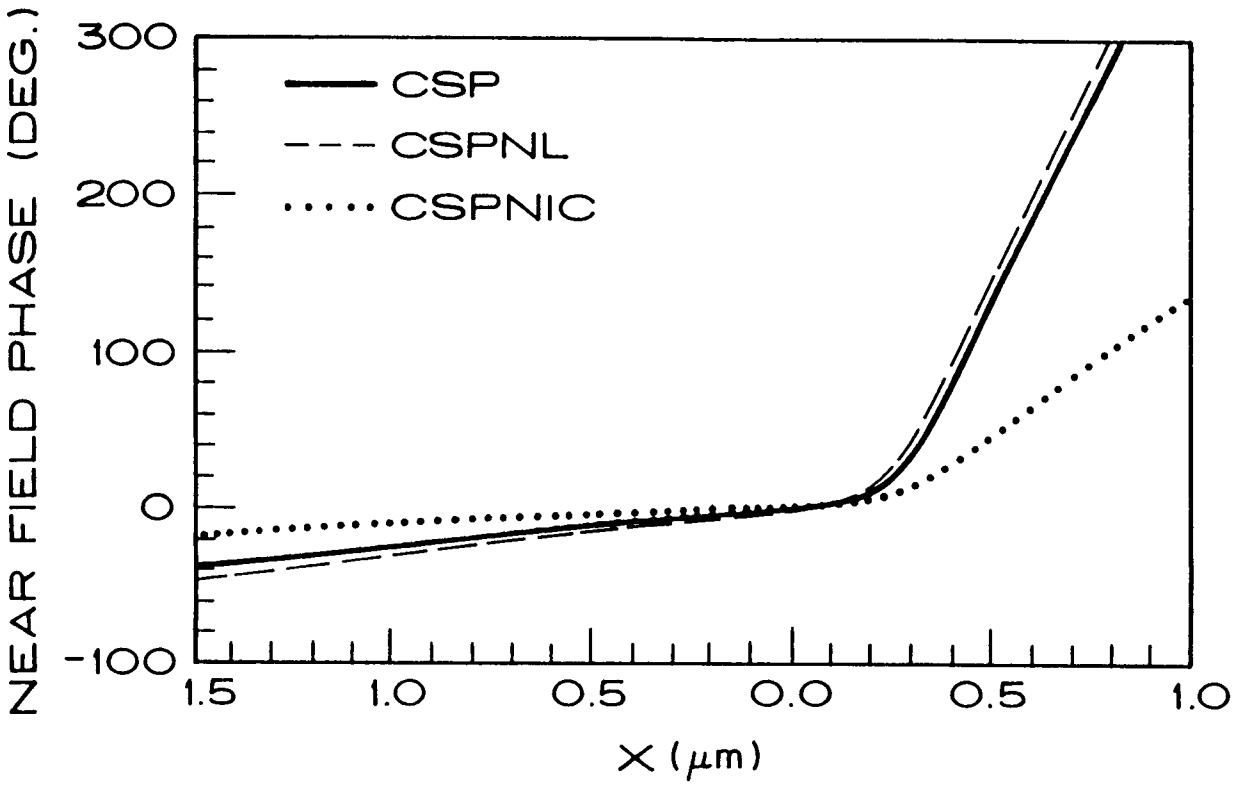

Figure 6. The transverse a) near field intensity, b) near field phase, and c) far field intensity in the region outside the channel region for a conventional CSP laser (——), a CSP laser with no absorption in the GaAs substrate (---) and a structure with the same index in the substrate as the channel region, but with high losses (10,000 cm^{-1}) in the substrate (....). All structures have an active layer thickness of 600 Å.

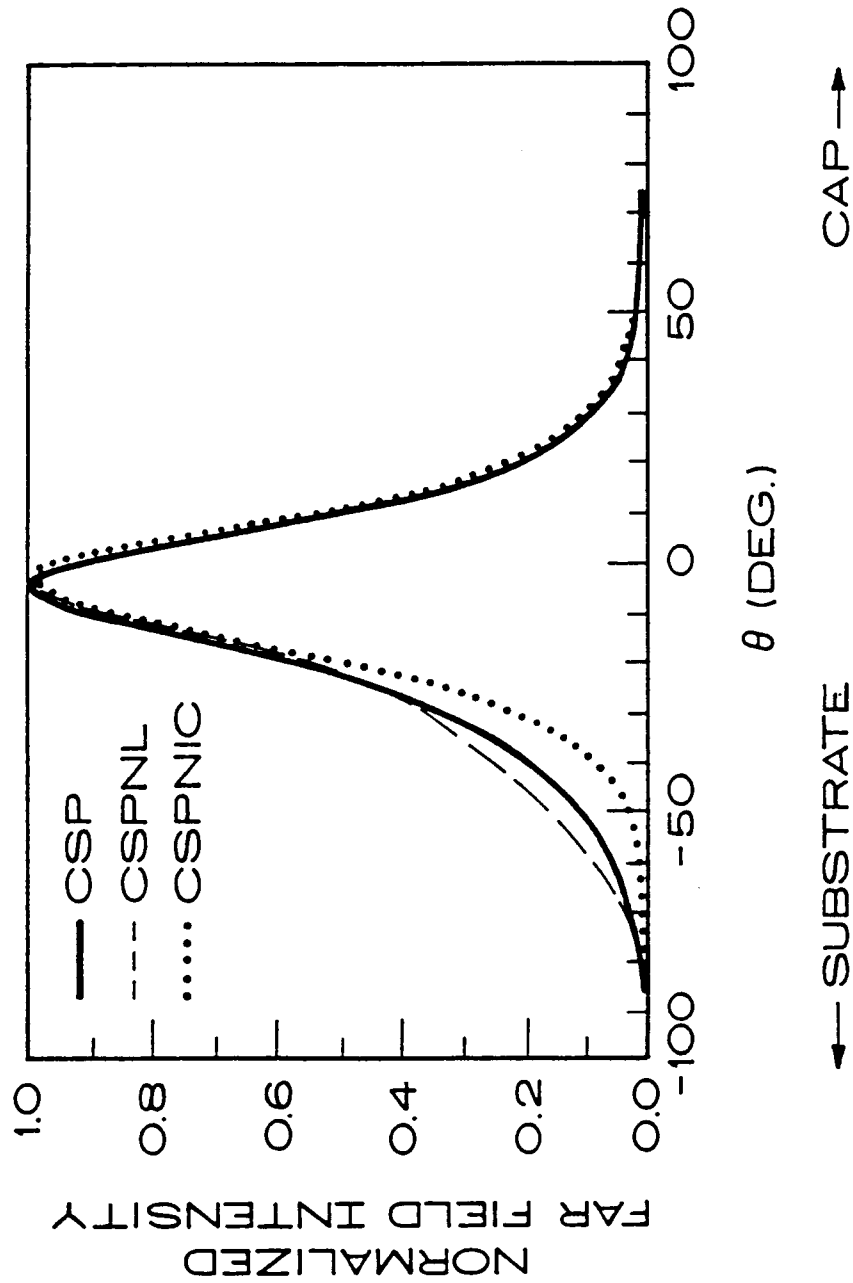

Figure 6. The transverse a) near field intensity, b) near field phase, and c) far field intensity in the region outside the channel region for a conventional CSP laser (——), a CSP laser with no absorption in the GaAs substrate (---) and a structure with the same index in the substrate as the channel region, but with high losses (10,000 cm^{-1}) in the substrate (....). All structures have an active layer thickness of 600 Å.

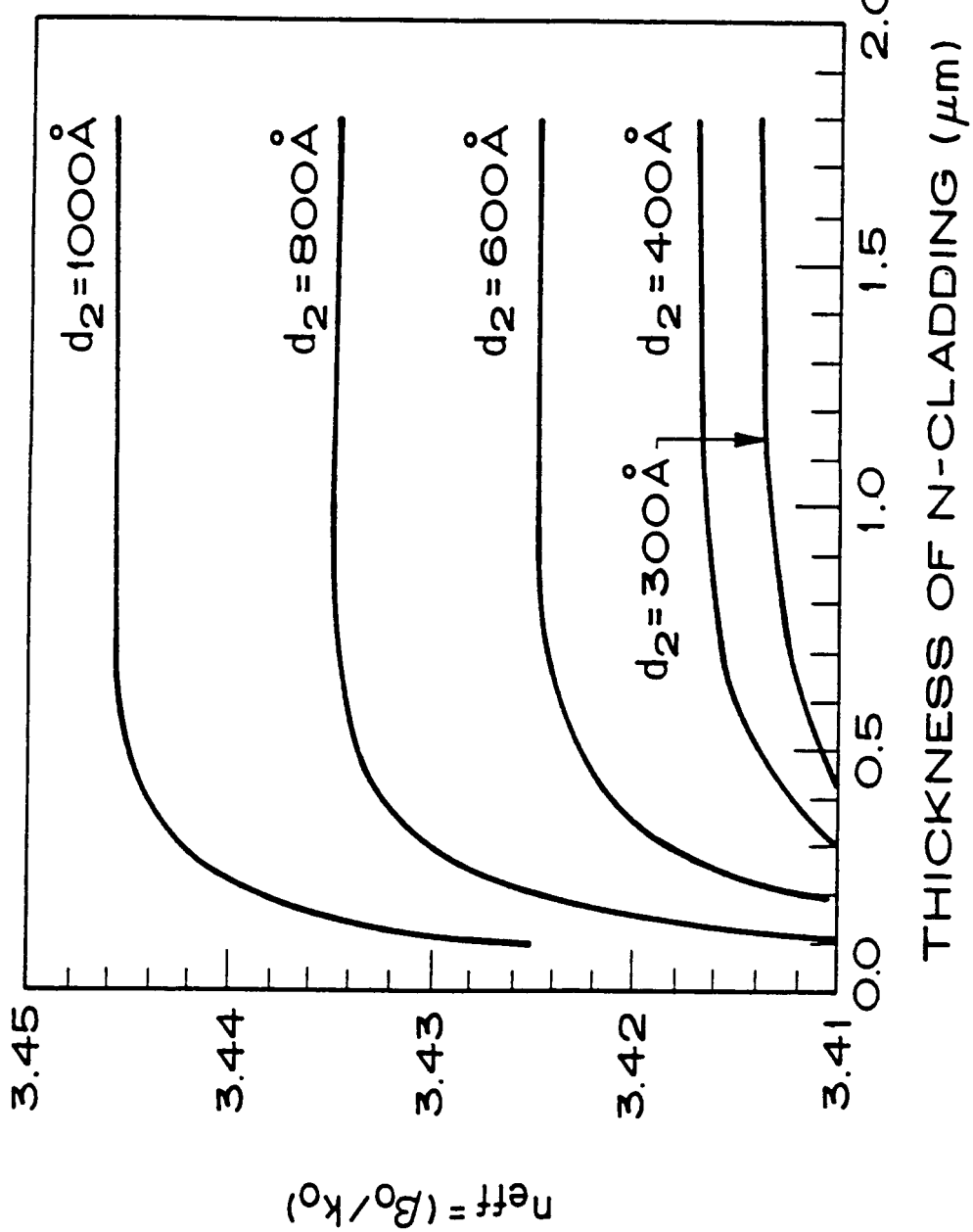

Figure 7. The a) real part of the effective index and b) imaginary part of the effective index as a function of the n-clad thickness for active layer thicknesses of 400, 600, 800, and 1000 Å of a conventional CSP laser.

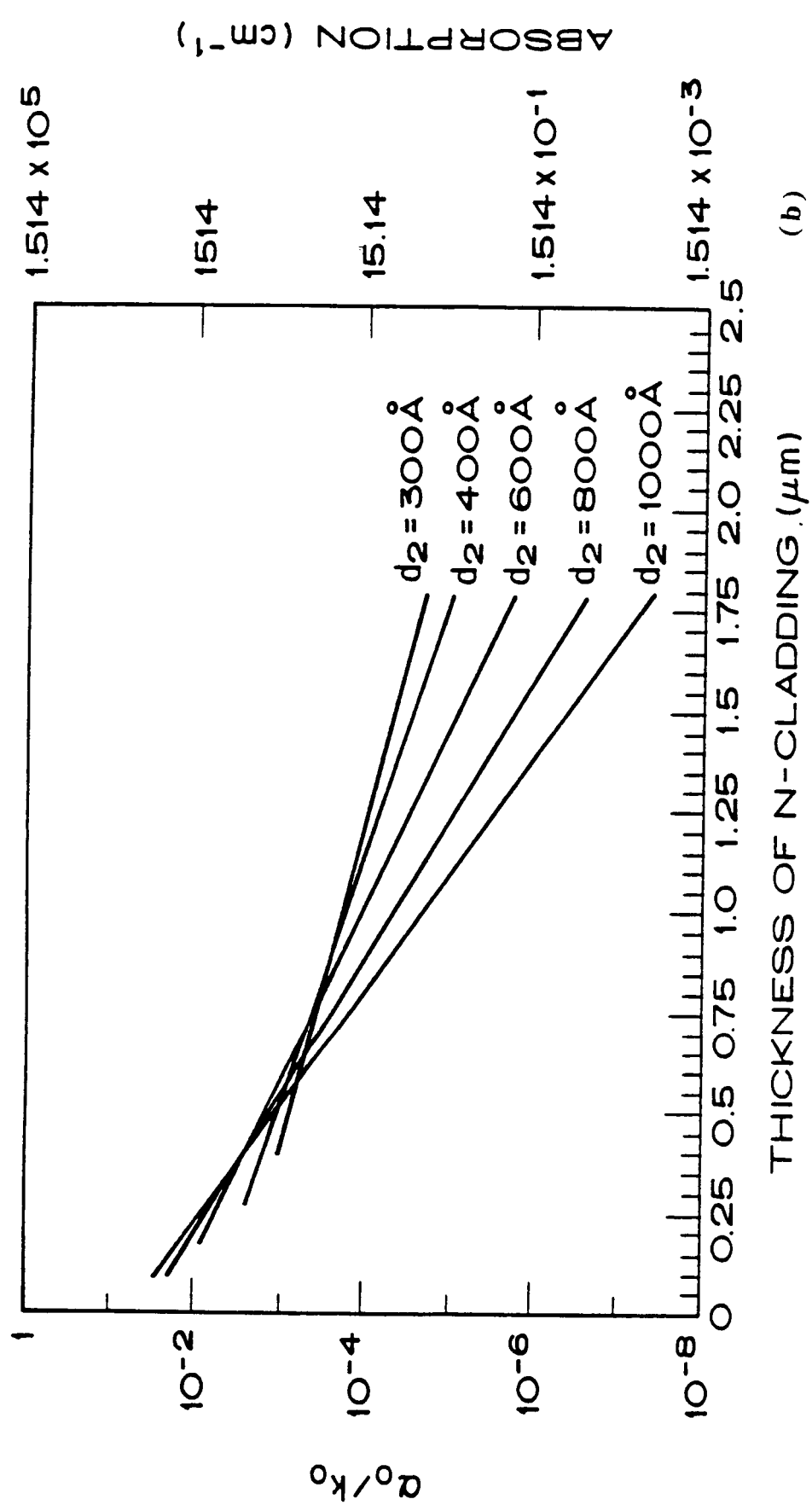

Figure 7. The a) real part of the effective index and b) imaginary part of the effective index as a function of the n-clad thickness for active layer thicknesses of 400, 600, 800, and 1000 Å of a conventional CSP laser.

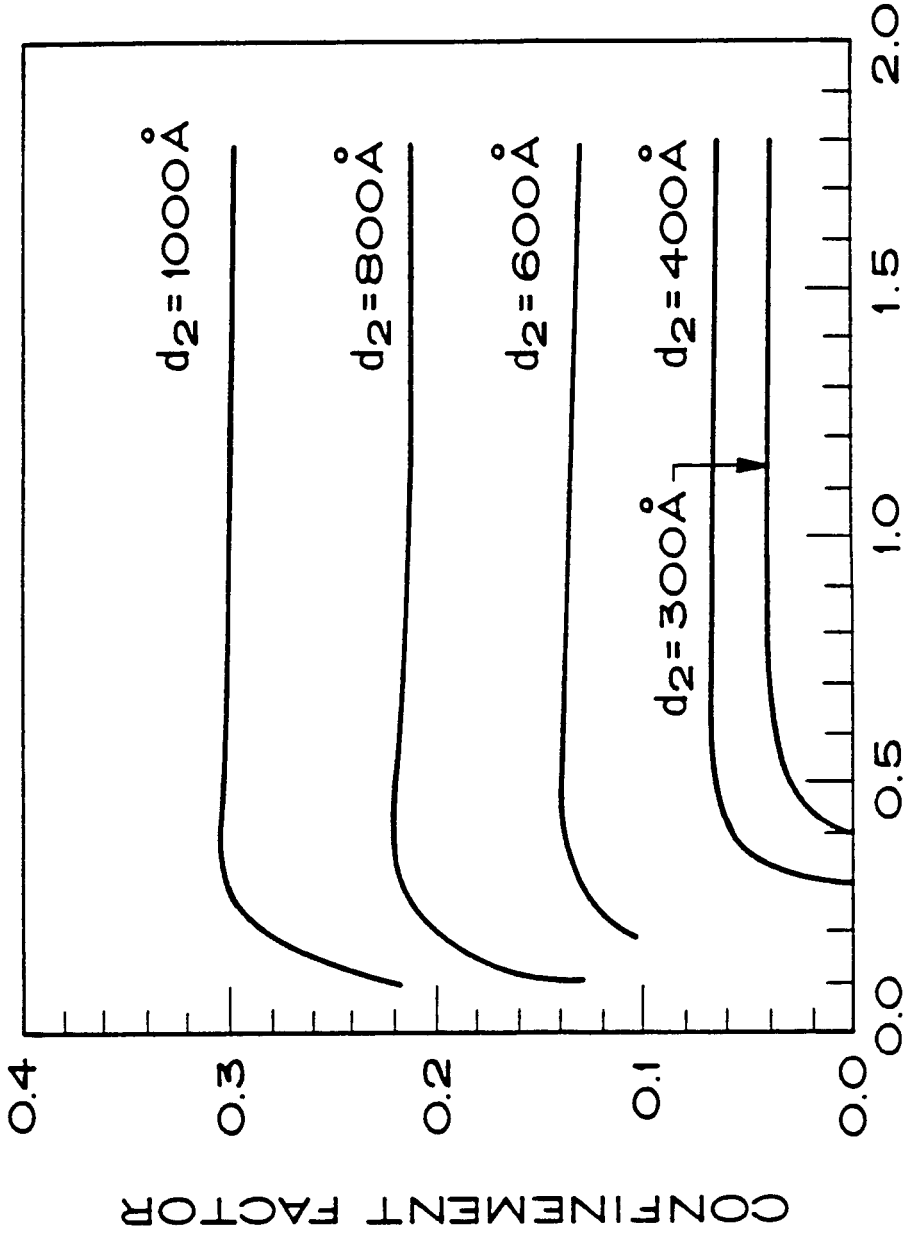

Figure 8. The active layer confinement factor as a function of the n-clad thickness for active layer thicknesses of 400, 600, 800, and 1000 Å of a conventional CSP laser.

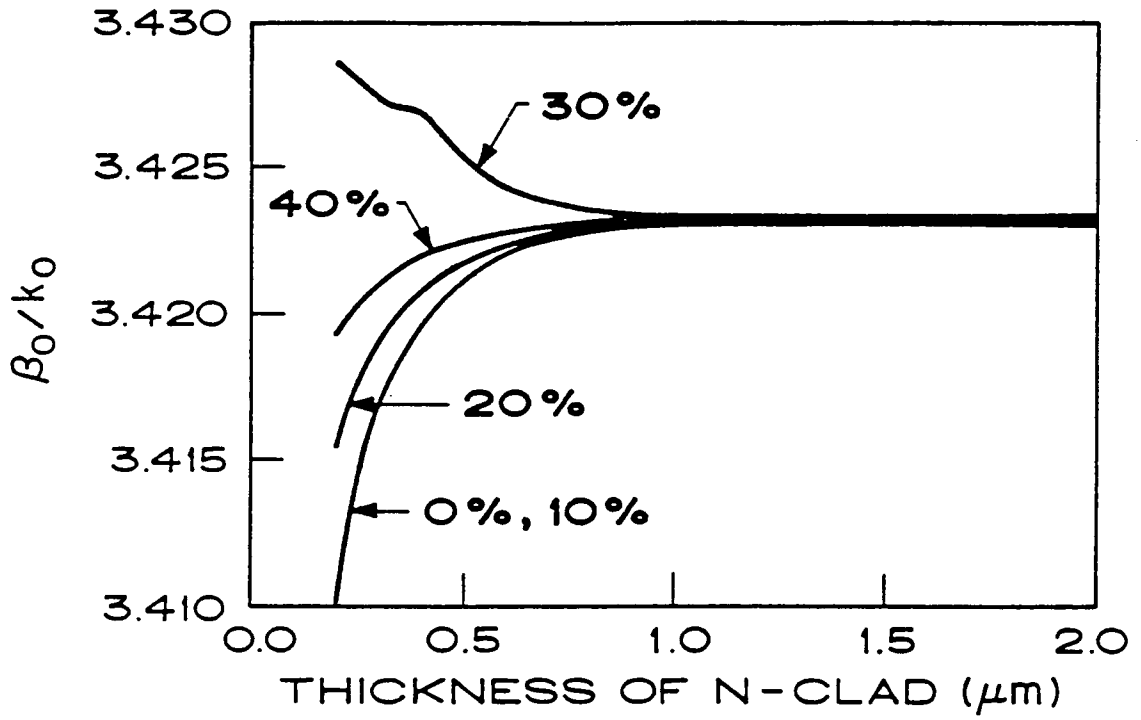

(a)

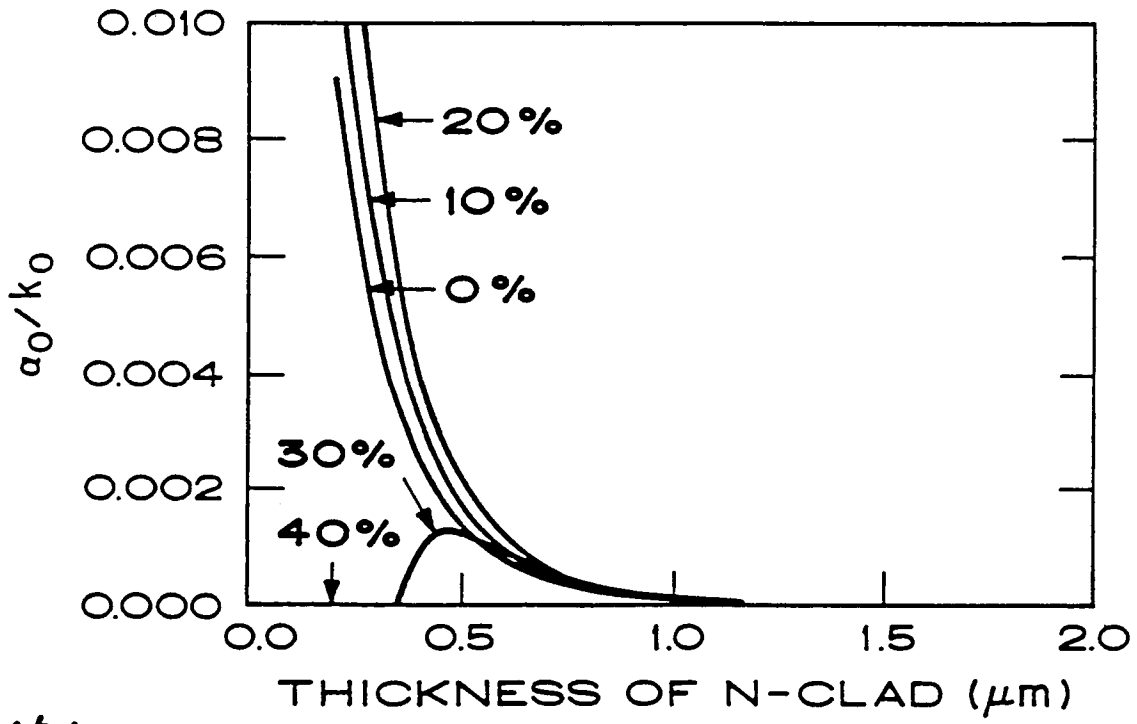

(b)

Figure 9. The a) real part of the effective index and b) imaginary part of the effective index as a function of the n-clad thickness for an active layer thickness of 600 Å for CSP lasers with mole fractions of AlAs of 0, 10, 20, 30, and 40%.

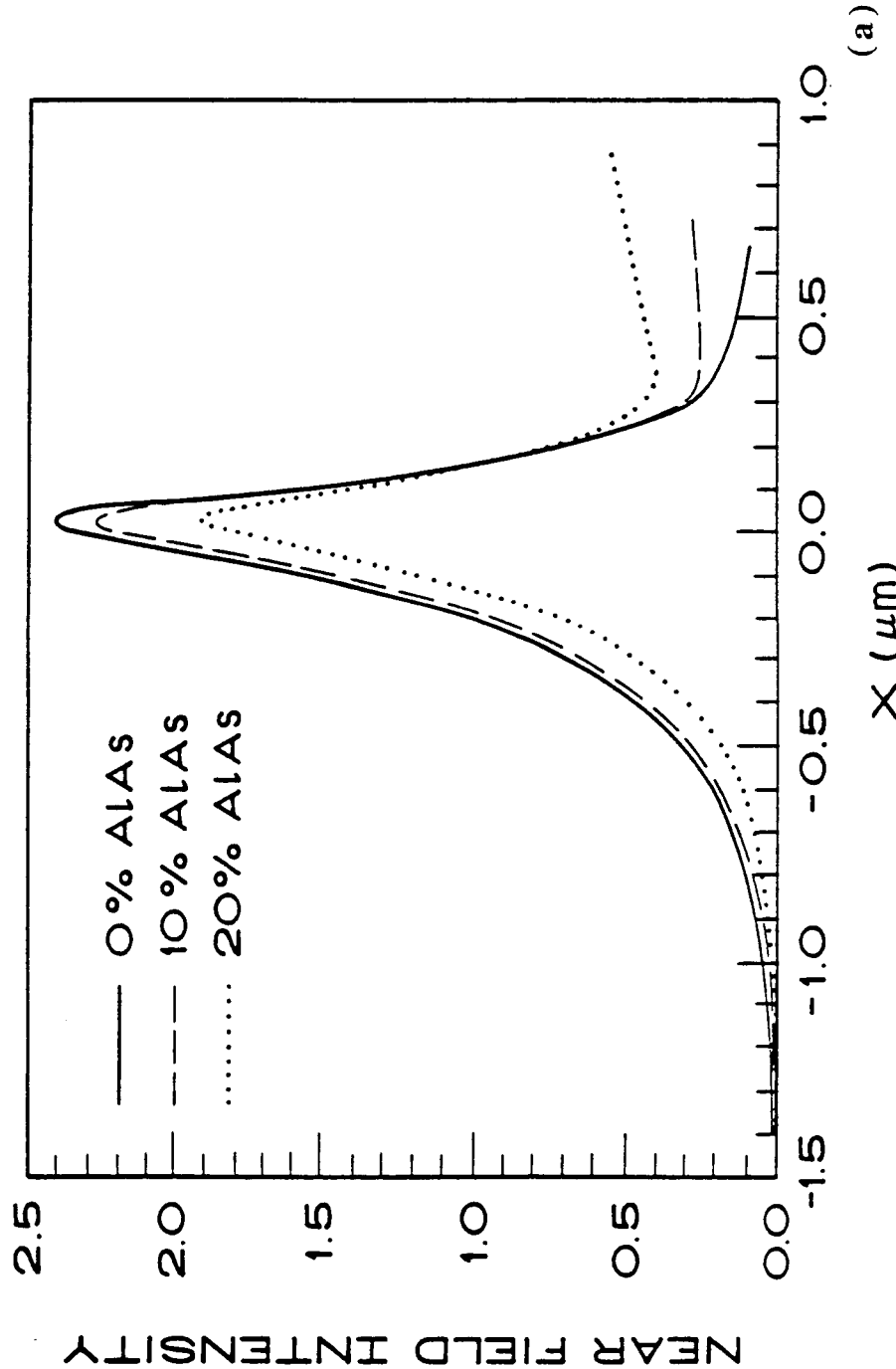

Figure 10. The transverse a) near field intensity, b) near field phase, and c) far field intensity pattern $I_W(\theta)$ in the region outside the channel region for CSP lasers with mole fractions of AlAs in the substrate of 0 (——), 10 (---), and 20% (···).

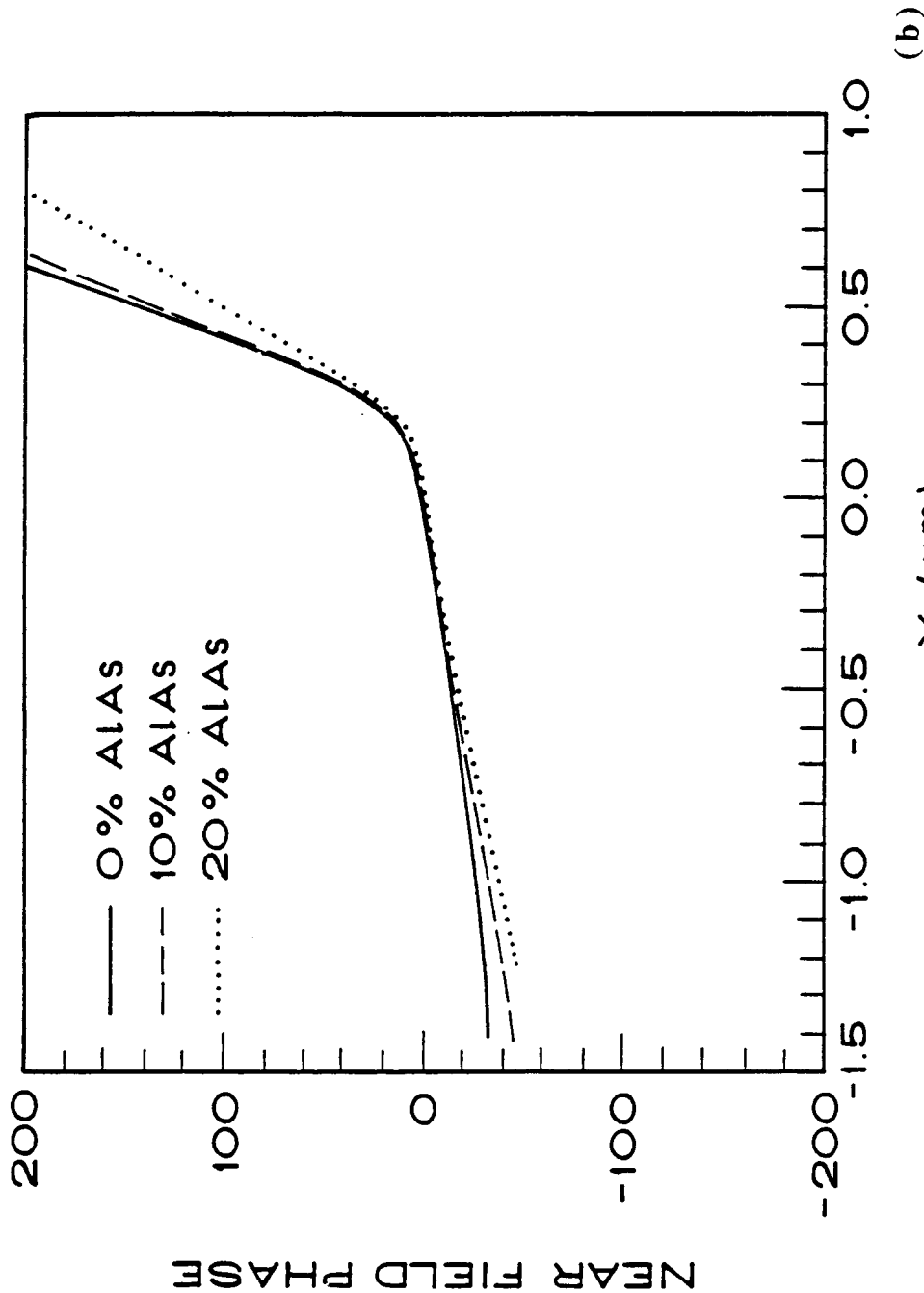

Figure 10. The transverse a) near field intensity, b) near field phase, and c) far field intensity pattern $I_W(\theta)$ in the region outside the channel region for CSP lasers with mole fractions of AlAs in the substrate of 0 (——), 10 (---), and 20% (···).

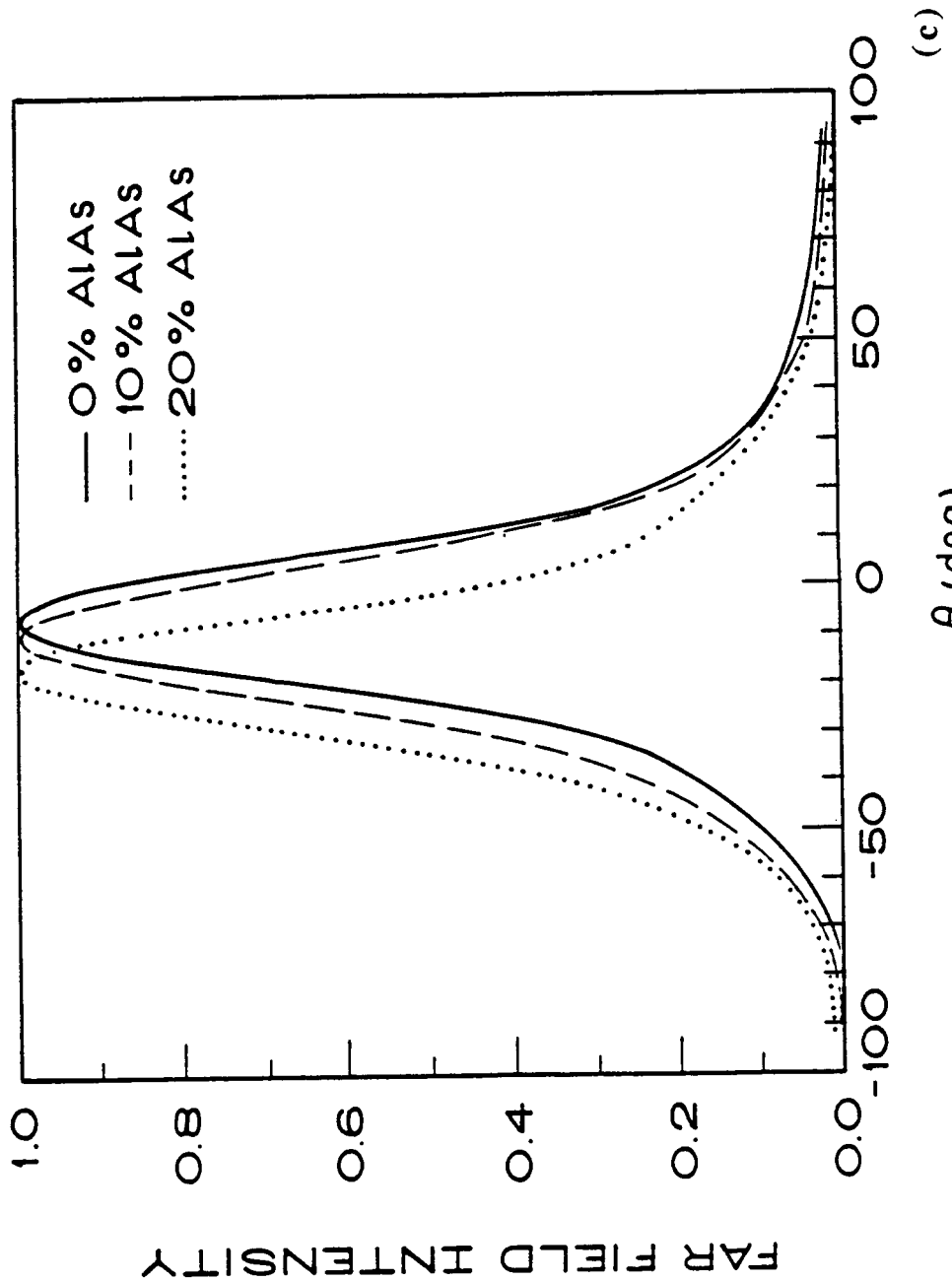

Figure 10. The transverse a) near field intensity, b) near field phase, and c) far field intensity pattern $I_w(\theta)$ in the region outside the channel region for CSP lasers with mole fractions of AlAs in the substrate of 0 (——), 10 (---), and 20% (···).

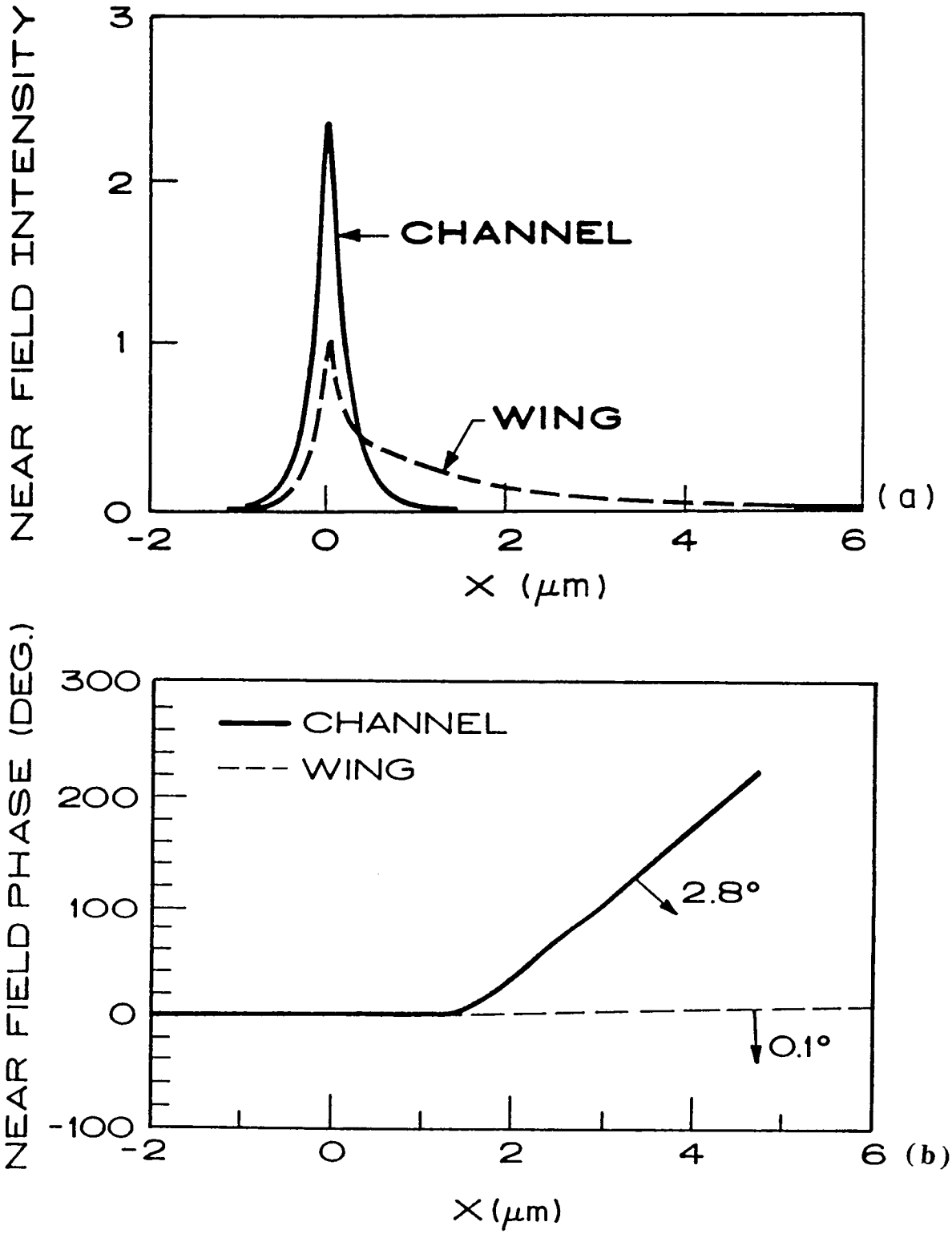

Figure 11. The transverse a) near field intensity, b) near field phase, and c) far field intensity pattern for a CSP laser with a mole fractions of AlAs in the substrate of 30%.

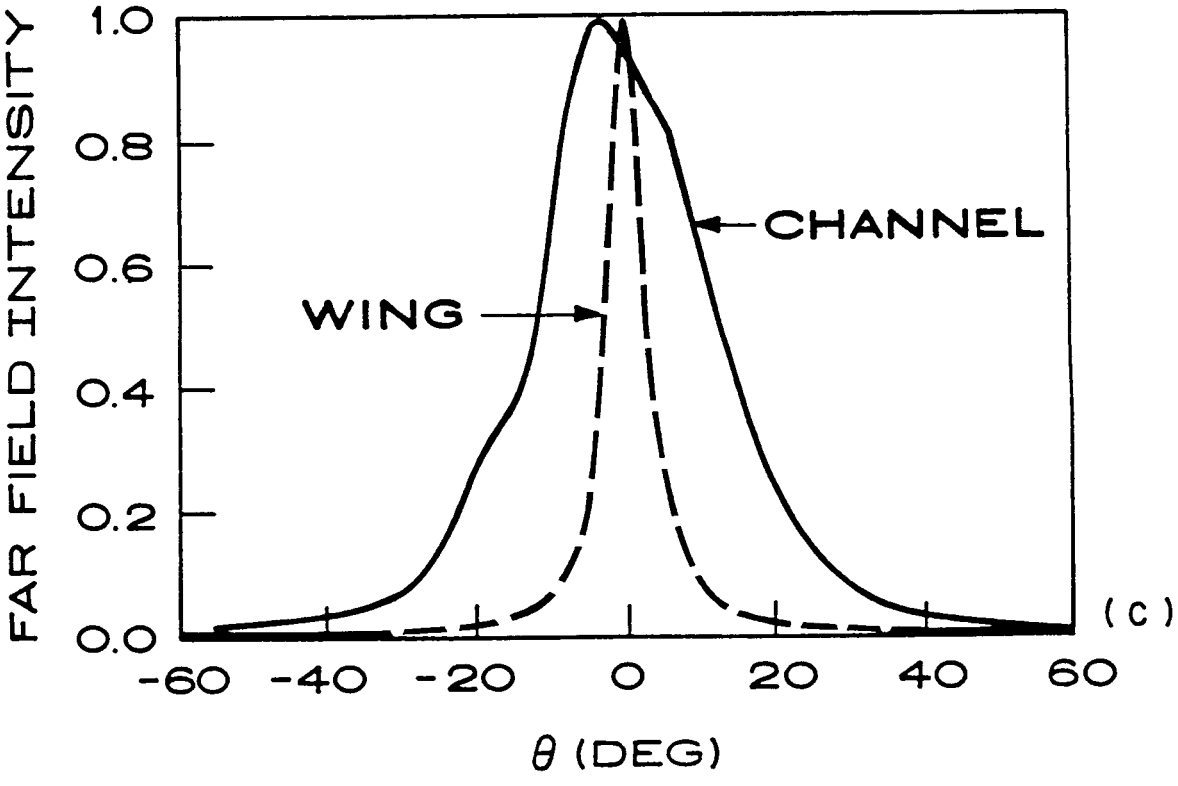

Figure 11. The transverse a) near field intensity, b) near field phase, and c) far field intensity pattern for a CSP laser with a mole fractions of AlAs in the substrate of 30%.

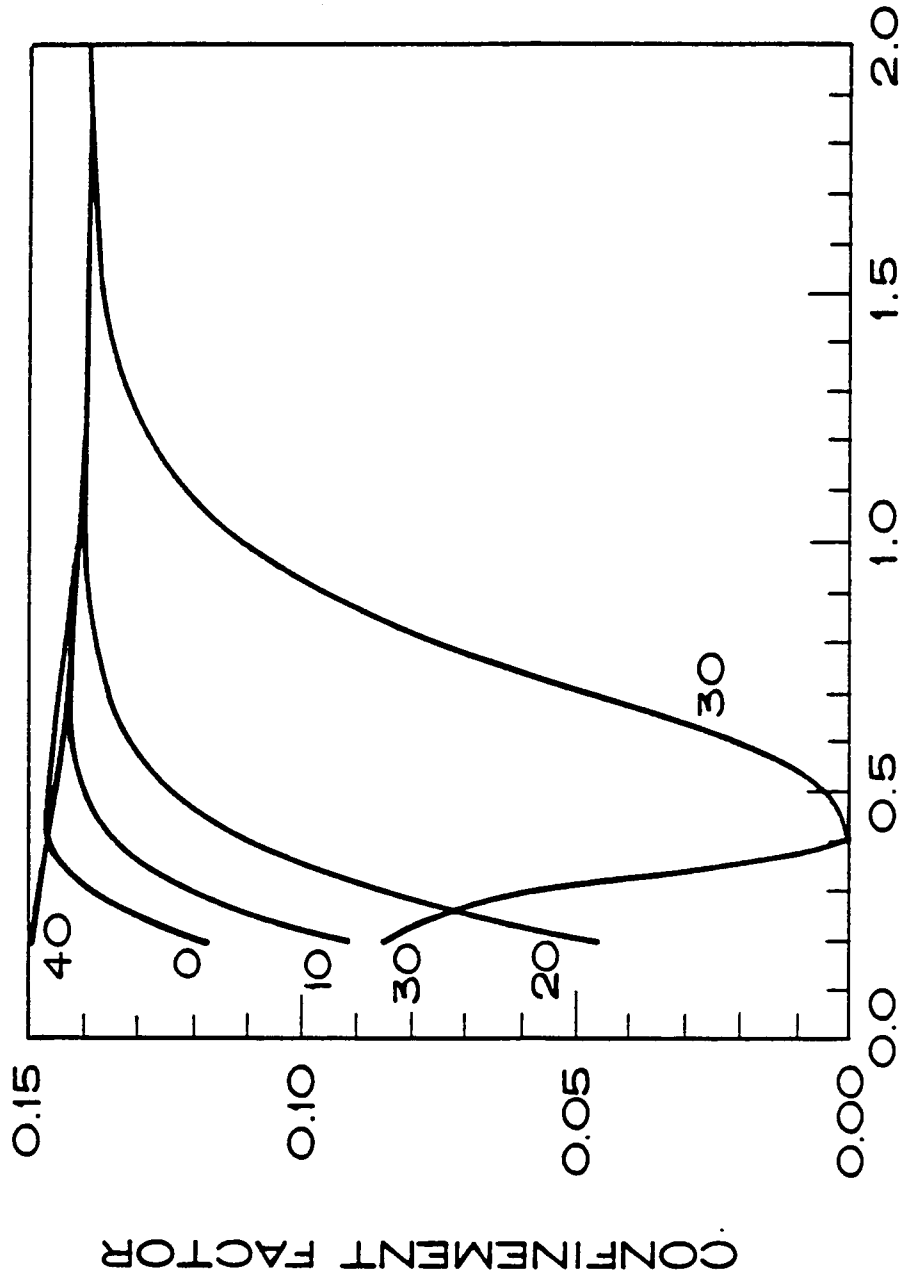

Figure 12. The active layer confinement factor as a function of the n-clad thickness for an active layer thickness of 600 Å for CSP lasers with mole fractions of AlAs of 0, 10, 20, 30, and 40%.

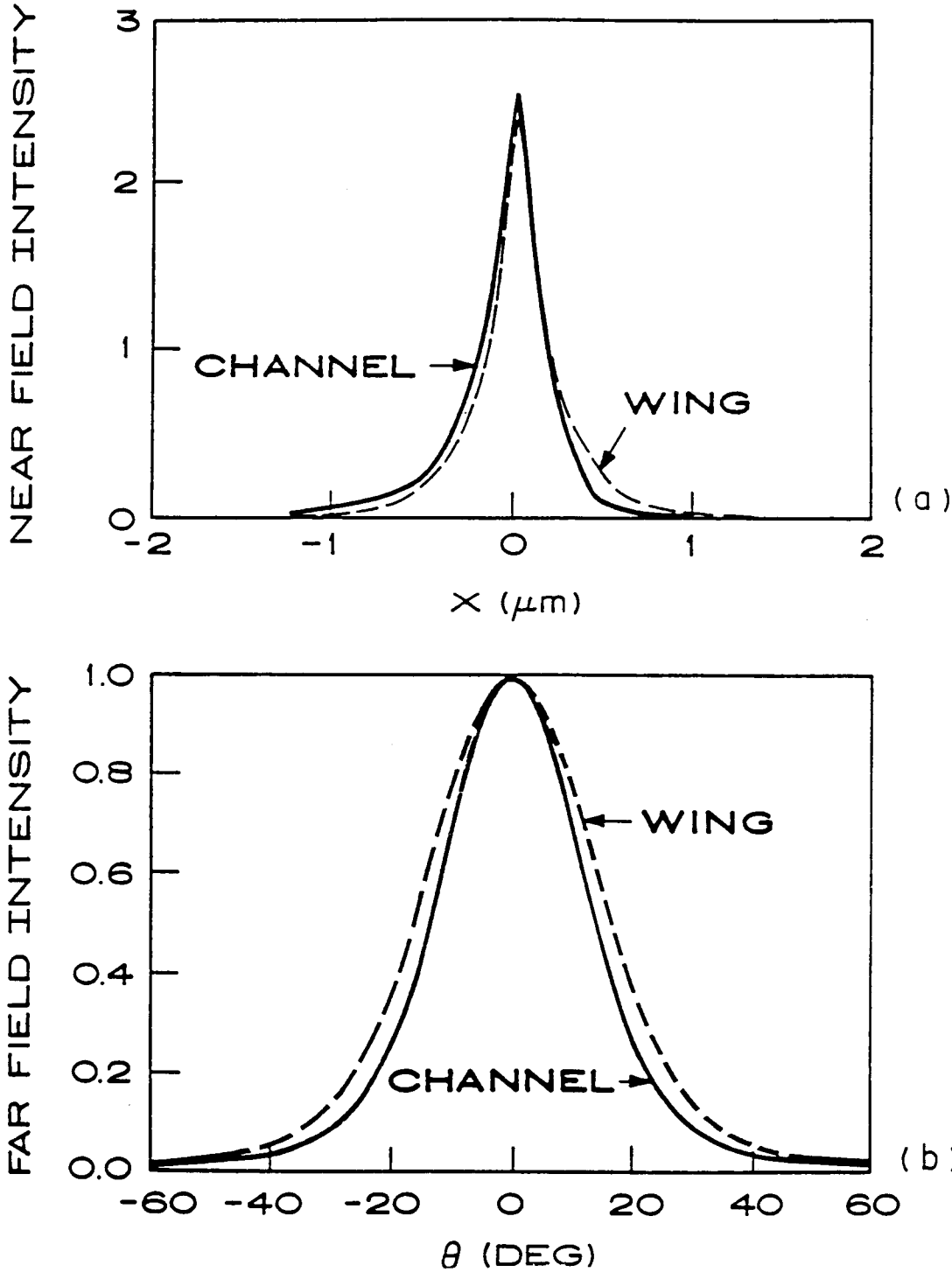

Figure 13. The transverse a) near field intensity and b) far field intensity pattern $I_{ch}(\theta)$ and $I_w(\theta)$ for a CSP laser with a mole fractions of AlAs in the substrate of 40% in the region inside (——) and outside (---) the channel.

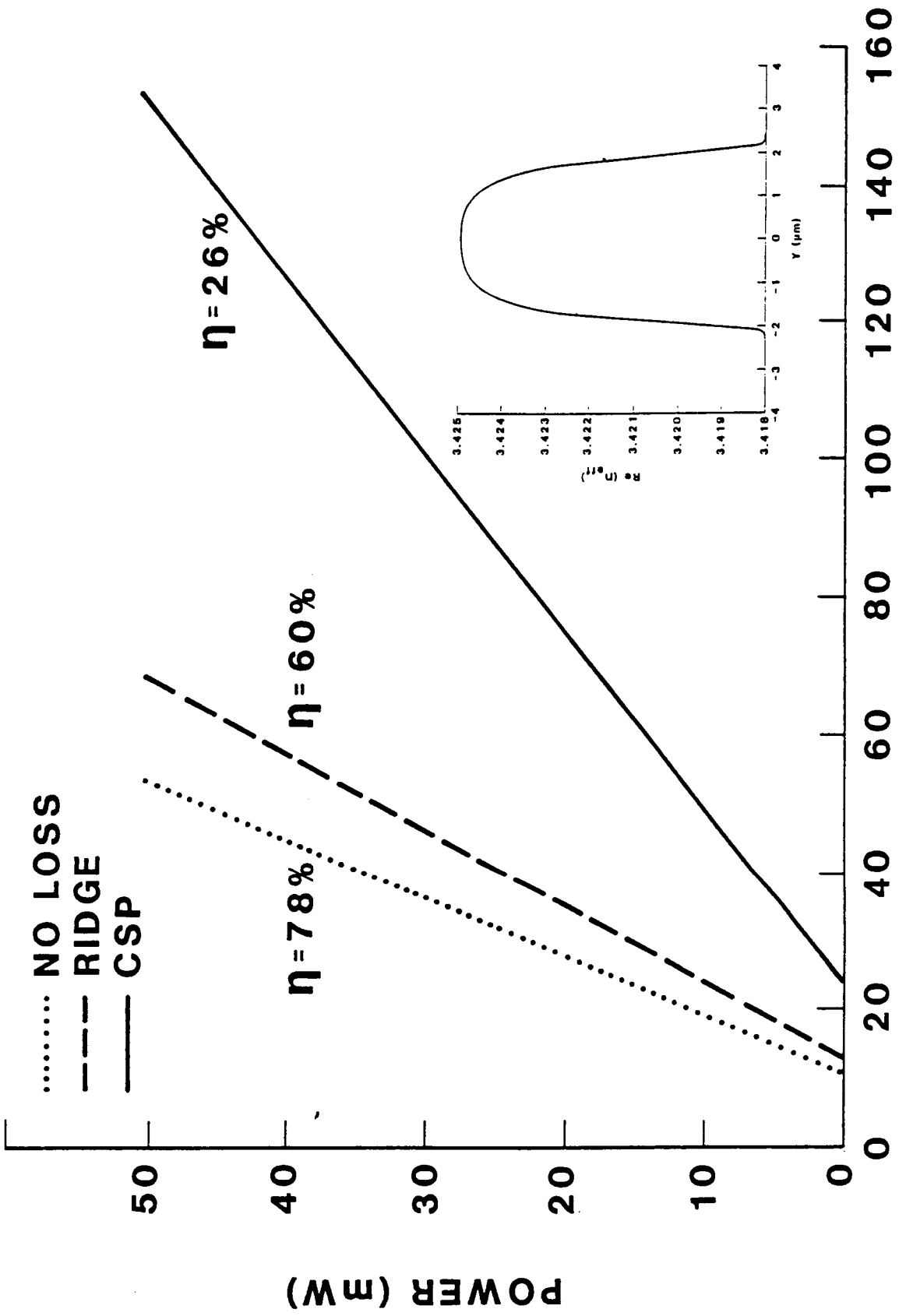

Figure 14. Calculated power versus current curves for a conventional CSP laser (——), a conventional ridge guide laser (---), and a lossless ridge guide laser (···).

Appendix B

Analysis and Performance of Channeled-Substrate-Planar Double-Heterojuntion Lasers With Geometrical Asymmetries

Jerome K. Butler, Gary A. Evans, and Bernard Goldstein

RCA Laboratories, Princeton, New Jersey 08540

ABSTRACT

The effects of geometrical asymmetries on the opto-electronic properties of CSP-DH lasers using self-consistent calculations of the optical field and the electron-hole distribution in the active layer are analyzed and compared with device measurements. Laser properties modeled include gain profile, threshold, slope efficiency, near field, and far field. This analysis shows that small geometrical asymmetries due to device fabrication can produce significant changes in the optical and electrical properties of CSP-DH lasers, especially at high output power levels. For example, a 0.5 μm misalignment of the Zn diffusion with respect to the substrate channel can produce lateral near-field and far-field shifts of 0.6 μm and 2.5° respectively, and limit single spatial mode operation to about 30 mW.

Analysis and Performance of Channeled-Substrate-Planar Double-Heterojuntion Lasers With Geometrical Asymmetries

Jerome K. Butler, Gary A. Evans, and Bernard Goldstein

RCA Laboratories, Princeton, New Jersey 08540

INTRODUCTION

In this paper, we analyze the influence of changes in the profile of the lateral gain and effective index distributions on the opto-electronic properties of channeled-substrate - planar double-heterojunction (CSP-DH) semiconductor lasers. Alterations in gain profiles result from power dependent interactions of the optical field with the electron-hole distribution. In an ideal, symmetric structure alterations of the gain profile produce only slight changes in the full width half power (FWHP) of the near- and far- field patterns. However, slight geometrical asymmetries can cause significant and undesireable shifts in the field patterns with increasing current. Furthermore, these slight asymmetries limit the ultimate emission power.

Several asymmetries can occur during the growth and fabrication of CSP-DH lasers. A schematic diagram of the basic CSP-DH laser structure is shown in Fig. 1. Asymmetry of the channel (shown in Fig. 1b) can occur during etching of the channel into the substrate prior to growth or during the growth by meltback. Zinc diffused regions, used to confine current, may be misaligned with respect to the channel (Fig. 1c). Additionally, asymmetries introduced by nonuniform layer thicknesses and varying compositional properties generally produce variations in effective refractive index, and, if they exist in the active layer, strongly alter the local gain properties.

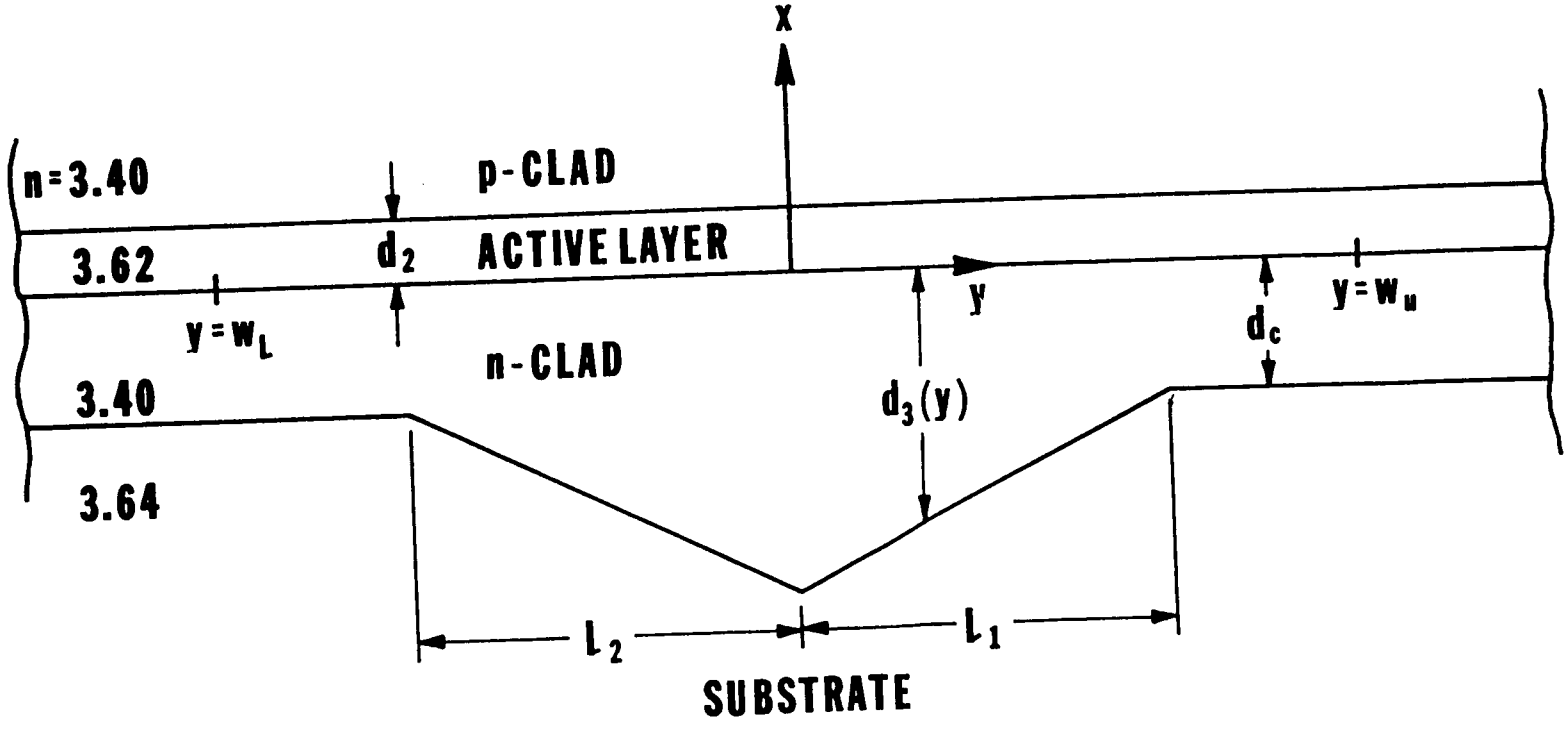

Fig. 1. The CSP-DH laser structure; a) idealized model, b) scanning electron micrograph illustrating channel assymetries, and c) scanning electron micrograph illustrating misalignment of the zinc diffusion with the channel.

ORIGINAL PAGE IS
OF POOR QUALITY

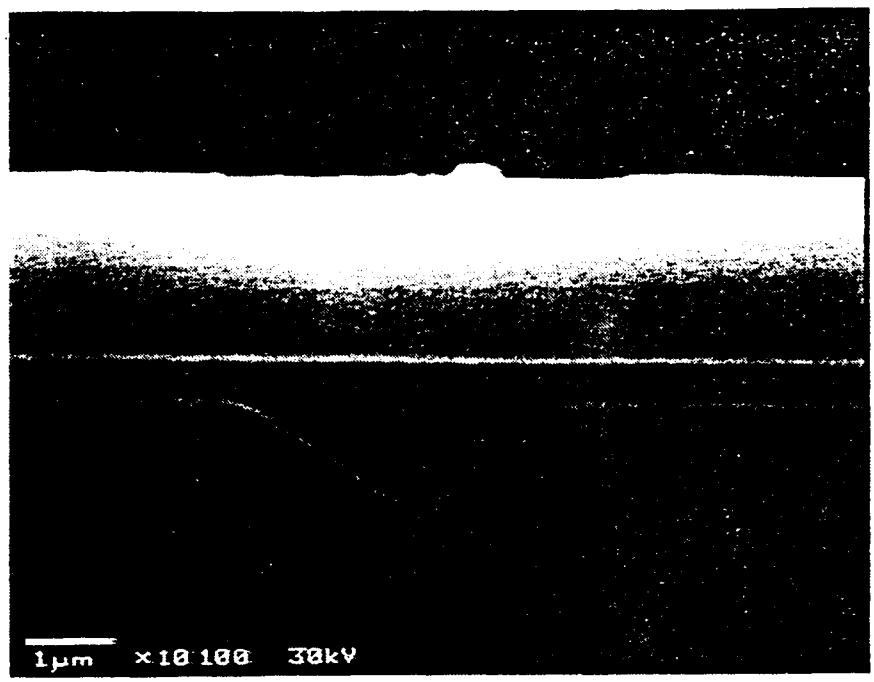

Fig. 1(b)

ORIGINAL PAGE IS
OE POOR QUALITY

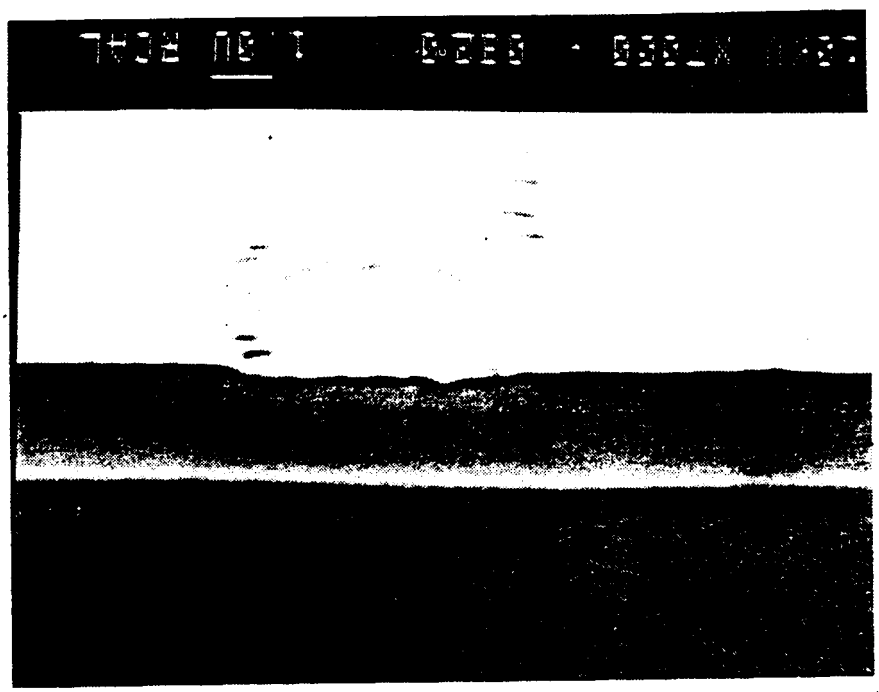

Fig. 1(c)

The first analysis of the static properties of stripe geometry lasers was given by Buus [1]. Analysis of different geometries and various laser materials have increased the understanding of the optical guiding mechanisms of semiconductor injection lasers [2-10]. In this paper, we have modeled some of the optical characteristics of CSP-DH lasers with different device geometries associated with device fabrication. In one case we model the ideal device with symmetric current excitations as well as with symmetric device geometry. In the second case, the current is symmetric, but the channel profile is slightly asymmetric (Fig. 1b). In the third case, we consider asymmetries associated with misalignment of the Zn diffusion relative to the channel (Fig. 1c). Our computations of the laser characteristics use a self-consistent calculation of the optical field and of the electron-hole pair distribution in the active layer. These are the first detailed computations that show how small asymmetries in the device geometry affect the optical and electrical properties of the CSP-DH laser. The parameters of the device model include the effects of the various layer thicknesses, refractive indices and material absorption coefficients. Theoretical computations of the opto-electronic properties of symmetrical and asymmetrical configurations show good agreement with experimental measurements made on LPE grown CSP-DH lasers [11].

The lasers discussed in this paper were grown by multi-bin liquid phase epitaxy on a (100) GaAs substrate on which grooves had been chemically etched. Zinc stripe diffusion and final contacting were accomplished by using a chemical vapor deposited SiO_2 diffusion mask and standard photolithographic techniques followed by e-beam evaporation of Ti-Pt-Au on the p-side and Au-Ge on the n-side. The diodes were mounted onto Au-plated Cu heat sinks using In or Sn solder.

MODEL

Field Analysis

The analysis of the optical fields in CSP-DH lasers is obtained by solving Maxwell's equations. The usual approach in determining the two dimensional optical field, known as the effective index method, is to first solve for the transverse fields (perpendicular to the active layer) using simple multi-layer waveguide theory. From the solution to the layered waveguide field at specific lateral points, the lateral effective index along the y direction is established (Cf. Fig. 3a). When the various layers have loss or gain, the effective index is complex. The absorption in the active layer is accounted for in the expression of the gain profile which we discuss later. The GaAs substrate has a very large absorption coefficient ($\sim$ 5000 - 10,000 cm^{-1}) while those of the p- and n- cladding layers are on the order of 10 cm^{-1}.

Assuming an $\exp[j\omega t-\gamma z]$ longitudinal and time variation of the electric field, where γ is the complex propagation constant, z the longitudinal coordinate, ω the radian frequency, and t is time, the transverse electric field polarized along y can be written as [12,13]

$$E_y = E_o\, u(x,y)\, v(y) \exp[-\gamma z] \tag{1}$$

where the complex function u(x,y) determines the transverse field shape along x, but it is slowly varying (along y) compared to v(y) which defines the lateral field profile. For a lasing mode the eigenvalue γ must satisfy the oscillation condition $Re\{\gamma\} = -G/2$, where $G = -\ln(R_1R_2)/(2L)$ is the modal gain, R_1 and R_2 are the facet reflectivities, and L is the length of the laser. The magnitude of G is equal to the emission losses at the laser facets. The differential equation for the lateral field v(y) satisfies

$$\partial^2 v/\partial y^2 + [\gamma^2 - \gamma_o^2 + k_o^2\, \Gamma_c(y)\, \kappa_v(y,N_{ph})]\, v = 0 \tag{2}$$

where $\Gamma_c(y)$ is the complex confinement factor

$$\Gamma_c = \int_0^{d_2} u^2(x,y)\,dx \Big/ \int_{-\infty}^{\infty} u^2(x,y)\,dx \qquad (3)$$

where d_2 is the active layer thickness. For an ideal structure with no loss or gain, the value of Γ_c is real. The complex effective index $n_{eff} = -j\gamma_o/k_o$ where $k_o = 2\pi/\lambda$ and γ_o is found from the solution of the transverse problem. The value $\kappa_v(y,N_{ph})$ is the gain (or carrier) dependent portion of the dielectric constant of the active layer and N_{ph} is the photon density in the active layer. At threshold, $N_{ph} = 0$, and $\kappa_v(y,N_{ph})$ is determined from the carrier injection and ambipolar diffusion processes in the active layer. Above threshold, $N_{ph} > 0$, and $\kappa_v(y,N_{ph})$ is then a function of v(y) so that Eq. (2) is nonlinear. In terms of the active layer gain g(y) and index changes due to carrier injection δ n(y), $\kappa_v(y,N_{ph})$ can be expressed as [12]

$$\kappa_v(y,N_{ph}) = 2n_2\delta n(y) + j\, n_2\ g(y)/k_o \qquad (4)$$

The value δ n(y) is linearly related to the carrier or gain profile as δ n(y) = R g(y) / k_o where R lies between -1 and -4 for laser structures of the type discussed here[14]. This relates the index change δn(y) at a point in the active layer to the gain g(y) at that position using a linear relationship. A more accurate description of δ n(y) in terms of g is a functional dependence where R/k_o is the first term of a Taylor series of the carrier dependent refractive index change.

The solution of Eq. (2) is obtained by numerical methods using a multipoint differential equation solver with prescribed boundary conditions[15]. In the structure of Figure 1a, the complex effective index of refraction is constant for both $y > w_u$ and $y < w_l$. If the optical fields and injected carrier profiles are neglected in the far lateral positions $y > w_u$ and $y < w_l$, the solution of Eq. (2) can be written as

$$v(y) = \begin{cases} v(w_u)\exp[p(w_u - y)], & y > w_u \\ v(w_l)\exp[q(w_l - y)], & y < w_l \end{cases} \quad (5)$$

where $v(w_u)$ and $v(w_l)$ are the boundary solutions. The complex values p and q are the evanescent field decay coefficients and satisfy the conditions

$$-p^2 = \gamma^2 - \gamma_o^2(w_u) + k_o^2 \Gamma_c(y) \kappa_v(y,0) \quad (6a)$$

$$-q^2 = \gamma^2 - \gamma_o^2(w_l) + k_o^2 \Gamma_c(y) \kappa_v(y,0) \quad (6b)$$

We have asummed that at the points $y = w_u$ and $y = w_l$, the optical fields are sufficiently small so that hole burning effects can be neglected.

Above threshold, the high optical fields in the region below the stripe contact become so intense that electron/hole pairs are depleted at a fast rate. The rate of recombination is proportional to the product of the photon density $N_{Ph}(x,y)$ and the optical gain coefficient g(y). Thus, stimulated recombination acts as a sink for carriers while the applied current density is the source. The resulting carrier distribution must be found from solutions of the diffusion equation.

Carrier Diffusion

To determine the source and sink terms in the diffusion equation, we must describe the current injection into the active layer as well as the optical fields inside the laser cavity. Current injection into the active layer depends on the stripe contact width S, and the resistivities and thicknesses of the various layers. In addition, if zinc is diffused through the cap and p-clad layers above the channel, the effects of the zinc finger must be included in the computations. Computations of the current distribution in the active layer of various CSP-DH laser structures have been made by using a finite-element code. Models were

developed for a self-consistent calculation for the voltage drop across the active layer caused by the electron/hole diffusion along the lateral direction [16]. These calculations have been made for devices with Zn diffusion in order to determine the effects of current confinement due to various diffusion depths. For very shallow depths the current spreads in the active layer, however, for deep diffusion depths, the current is almost constant under the stripe contact. In fact, our calculations on Zn diffused geometries show that the current spreading can be expressed by the well-known expression [17]

$$J_x(y) = \begin{cases} J_o & , |y| \le S/2 \\ J_o/[1 + (|y| - S/2)/y_o]^2 & , |y| > S/2 \end{cases} \qquad (7)$$

where J_o is the current density under the stripe. The value of y_o is primarily a function of Zn diffusion depth and stripe contact width, and the resistivities of the p-GaAs cap and p-AlGaAs cladding layers. For typical structures where the Zn diffusion front extends approximately halfway through the p-clad layer, the value of y_o lies in the range of a few tenths to several microns. The large values of y_o occur for small stripe widths. Nevertheless, the exact shape of the current injection profile plays a secondary role in the shape of the carrier profile in the active layer because the ambipolar diffusion process causes carrier redistribution.

The optical hole burning process plays a major role in the nonlinear nature of the electrical and optical properties of the laser. The field inside the cavity can be considered as a superposition of two traveling waves. Because the waves are propagating in opposite directions, there is a quasi-standing wave pattern in the axial direction. Spatial hole burning would occur along the axial direction if carrier diffusion lengths were small. However, since the carrier diffusion length $L_D >> \lambda_g/2$ where λ_g (= Im{2 π/γ) is the guide wavelength, we can neglect this axial variation of the carrier density. The photon density at a point in the axial direction is the sum of the photon densities in the forward and

backward traveling waves. The photon density in the active layer is given as a fraction $\Gamma(y)$ of optical power in the transverse direction overlapping the active layer, where

$$\Gamma(y) = \int_0^{d_2} |u(x,y)|^2 dx \; / \; \int_{-\infty}^{\infty} |u(x,y)|^2 \, dx \tag{8}$$

The real function $\Gamma(y)$ is different from the complex function $\Gamma_c(y)$ given in Eq. (3) which is the complex confinement factor that arises from the normalization of the complex-valued wave functions. The total photon density in the active layer becomes

$$N_{ph} = P_o n_{eff} \Gamma(y) |v(y)|^2 [\exp(Gz) + R_1 \exp(G\{2L - z\})] \; / \; [h\nu c d_2 \langle |v(y)|^2 \rangle] \tag{9}$$

where P_o is power in the forward traveling wave at z=0 (mirror 2), n_{eff} is the effective modal refractive index, c is the velocity of light, and R_1 is the reflectivity of mirror 1 located at z = L and G is the modal gain coefficient. The term $\langle |v(y)|^2 \rangle$ is the integral of the field intensity over the lateral dimension. The z-dependence of N_{ph} is nearly uniform over the cavity length so that the two exponential terms can be averaged over the length of the cavity. The resulting expression for the stimulated recombination term R_{st} in the diffusion equation becomes

$$R_{st} = 2P_1 \Gamma(y) |v(y)|^2$$
$$x\{1 - R_1 - (R_1R_2)^{1/2} + (R_1/R_2)^{1/2}\} g(y) / [h\nu \, d_2 \langle |v(y)|^2 \rangle (1 - R_1) \ln(1/R_1R_2)] \tag{10}$$

where the emission from the front facet P_1 is related to the power inside the laser at z = 0 (P_o) by

$$P_1 = P_o (1 - R_1) \exp(GL). \tag{11}$$

We have assumed the oscillation condition $\exp(GL) = (R_1R_2)^{-1/2}$, to eliminate G in Eq. (11).

The necessary source and sink terms in the diffusion equation are now completely defined. Letting N(y) denote the electron-hole pair density, the diffusion equation becomes

$$D_e \partial^2 N(y)/\partial y^2 - N(y)/\tau_s - BN^2(y) = -J_x(y)/[qd_2] + R_{st} \qquad (12)$$

where D_e ($=L_D^2/\tau_s$) is the effective diffusion coefficient, τ_s is the spontaneous carrier lifetime, and B is the bimolecular recombination term. The gain coefficient is expressed as

$$g(y) = a\,N(y) - b \qquad (13)$$

In GaAs active layers, we use $a = 2.5 \times 10^{-16}$ cm^2 and $b = 190$ cm^{-1} [18].

Substitution of the gain expression into Eq. (12) gives a differential equation for the carrier density where the term P_1 is the emission power out of the front facet, assumed as a parameter, and the wave function v(y) is a solution to Eq. (2). Of course, self-consistency requires the simultaneous solution of both the wave equation which has a dielectric constant that is carrier dependent and the carrier diffusion equation which has an optical field dependence. The flow chart in Fig. 2 illustrates our method of solution. In Appendix A, we discuss the numerical formulation of the differential equations which are solved by a multipoint boundary value routine.

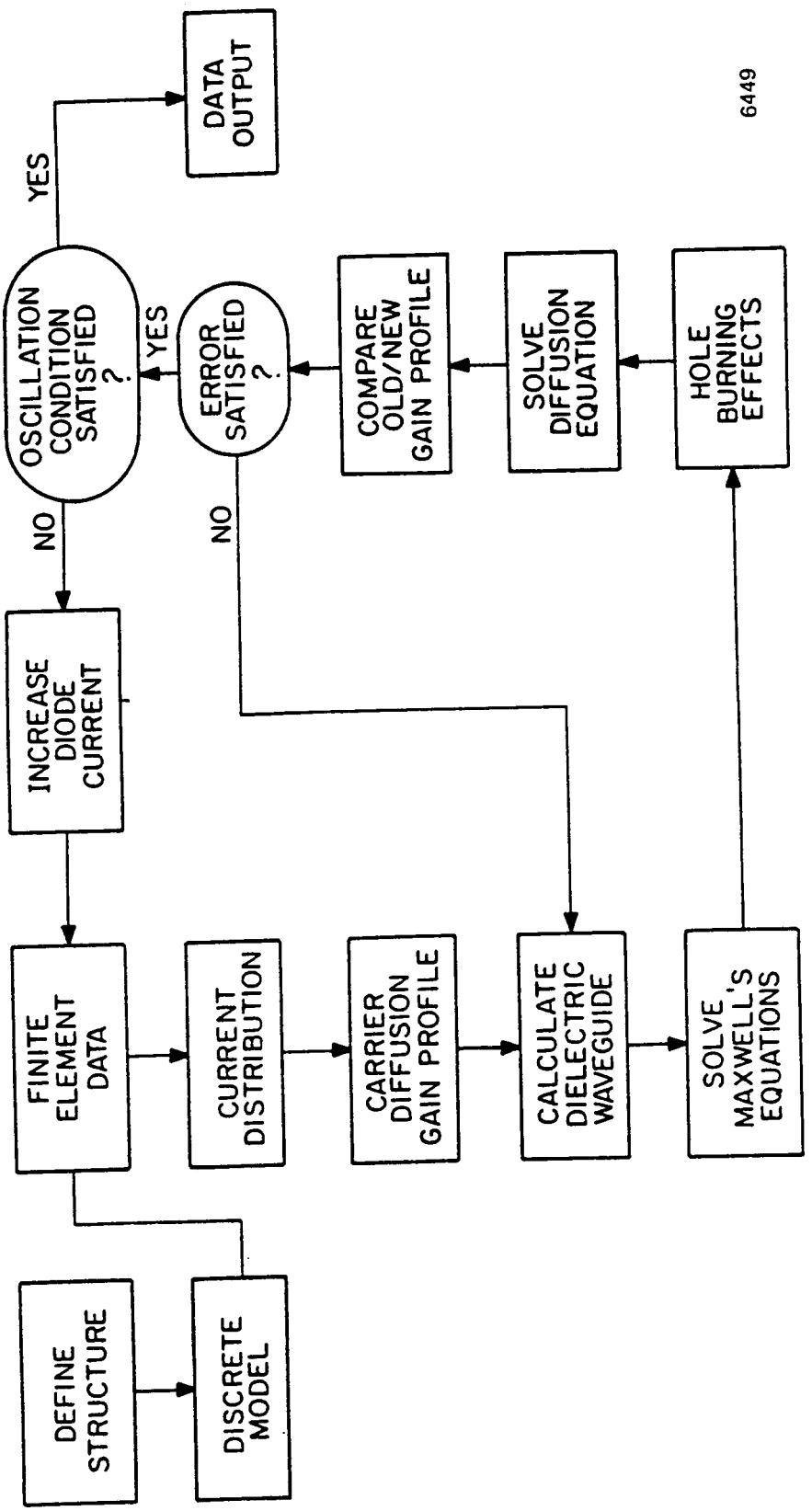

Fig. 2. Flow chart summarizing the numerical calculations for laser oscillation above threshold.

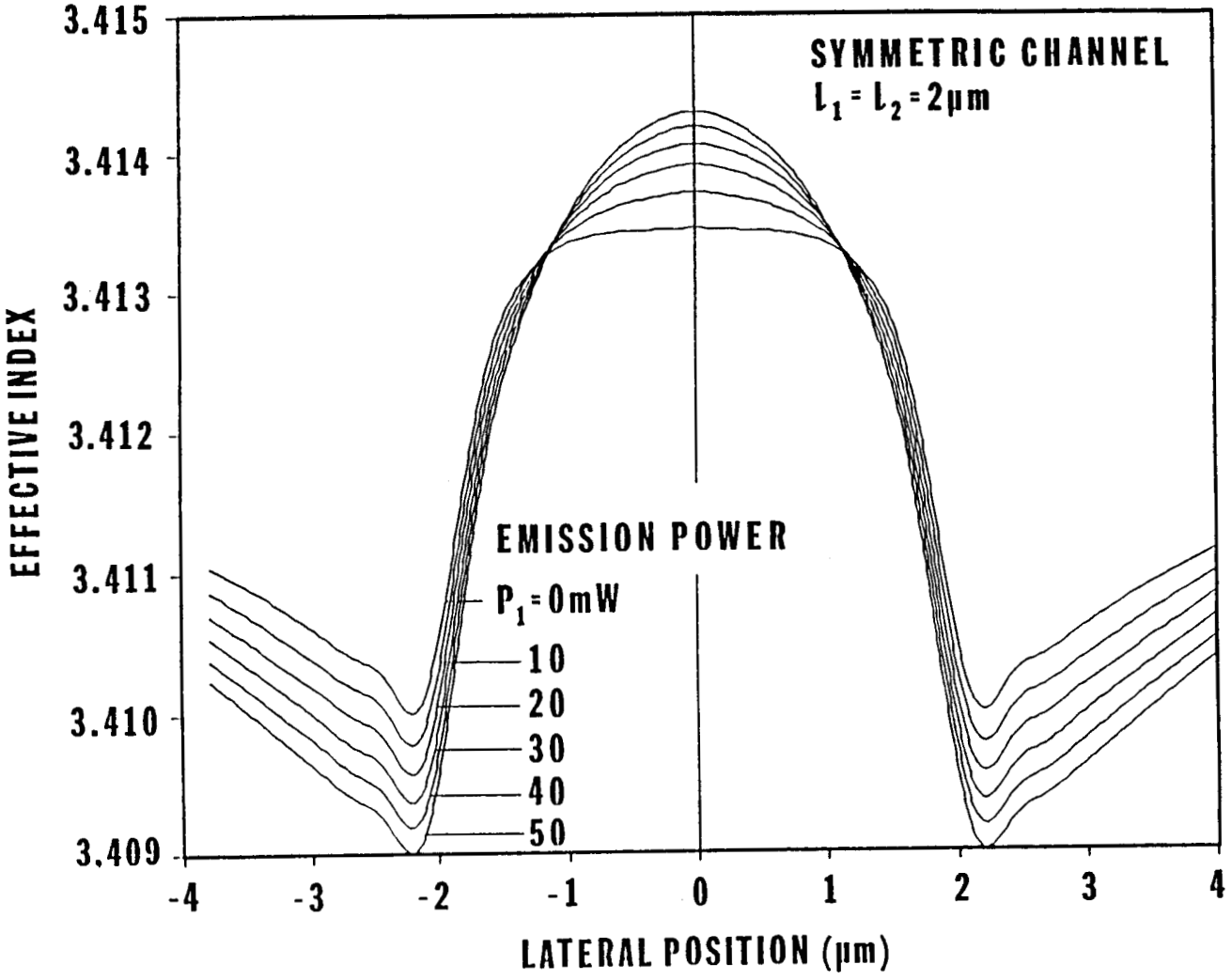

Fig. 3(a)

Fig. 3. Calculated a) lateral effective index profiles, b) lateral gain profiles in the active layer, c) near field intensity distributions, and d) far field intensity patterns for a symmetric CSP-DH structure (l_1 = 2.0 μm and l_2 = 2.0 μm) with a 4 μm wide Zn diffusion front for output powers of 0, 10, 20, 30, 40, and 50 mW.

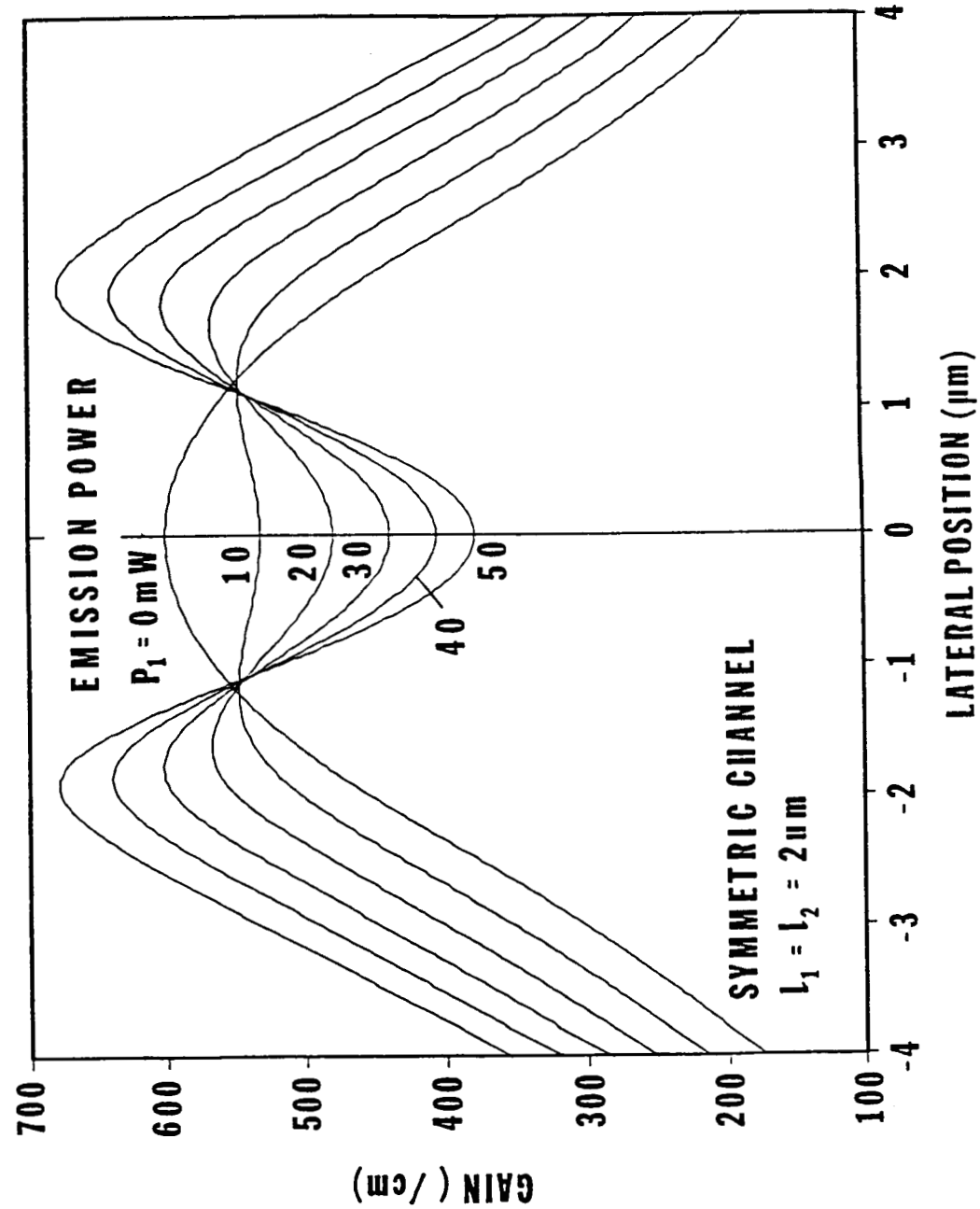
EMISSION POWER
P_1 = 0 mW
10
20
30
40
50
SYMMETRIC CHANNEL
$l_1 = l_2$ = 2 μm
GAIN (/cm)
LATERAL POSITION (μm)
700
600
500
400
300
200
100
-4
-3
-2
-1
0
1
2
3
4

Fig. 3(b)

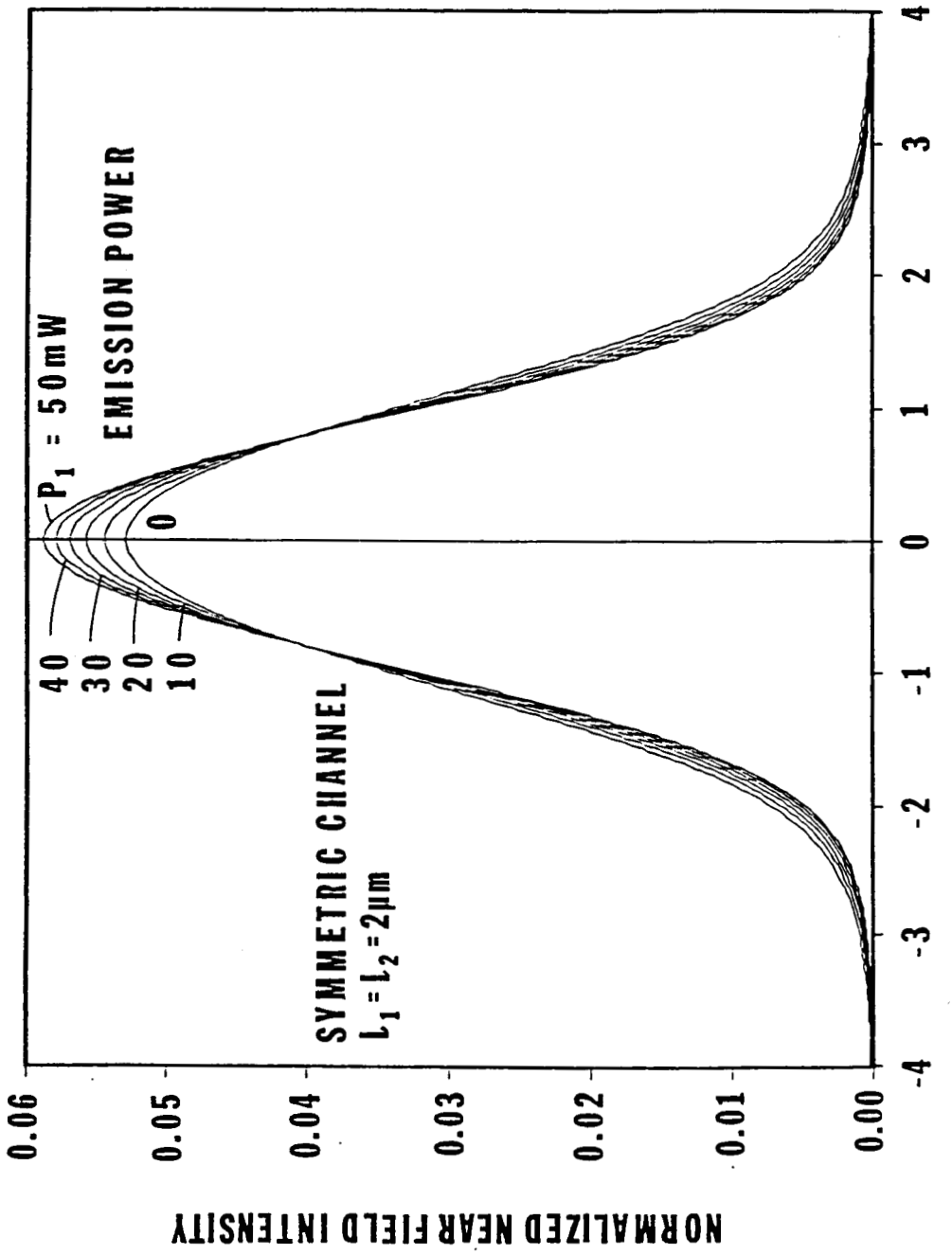
NORMALIZED NEAR FIELD INTENSITY
0.06
0.05
0.04
0.03
0.02
0.01
0.00
-4
-3
-2
-1
0
1
2
3
4
LATERAL POSITION (μm)
SYMMETRIC CHANNEL
$L_1 = L_2 = 2\mu m$
P_1 = 50mW
EMISSION POWER
40
30
20
10
0

Fig. 3(c)

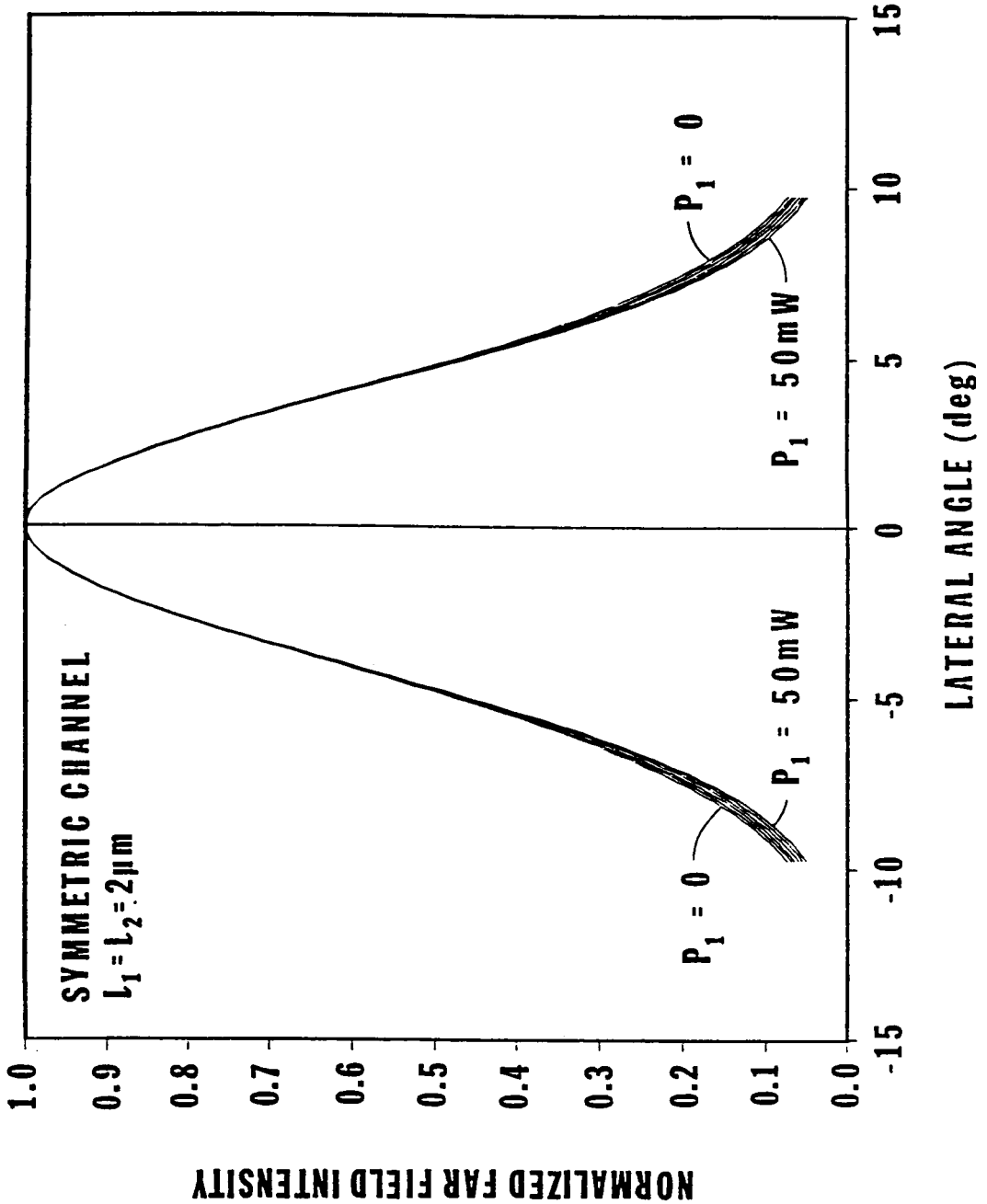
SYMMETRIC CHANNEL
$L_1 = L_2 = 2\mu m$
$P_1 = 0$
$P_1 = 50mW$
$P_1 = 0$
$P_1 = 50mW$
NORMALIZED FAR FIELD INTENSITY
LATERAL ANGLE (deg)
1.0
0.9
0.8
0.7
0.6
0.5
0.4
0.3
0.2
0.1
0.0
-15
-10
-5
0
5
10
15

Fig. 3(d)

RESULTS AND DISCUSSIONS

The basic laser structure is illustrated in Fig. 1, and Table I gives the parameters used in the calculations. In the following discussion, we consider a symmetrical CSP-DH laser where the Zn diffusion is symmetrically located over the channel. For the asymmetrical structures, we first assume that the slope of the walls of the channel are different, with the Zn diffused region symmetrical about y = 0. Next we study the effects of a misaligned (relative to the channel) Zn diffused region over a symmetrical channel. In the cases shown in Figs. 3, 4, 5, and 9, the width of the Zn diffused region is S = 4 μm, the same as the width of the symmetric channel. In Fig. 6, S = 6 μm which is larger than the channel. In all computations, we show (a) the effective index, (b) the gain distribution in the active layer, (c) the near field intensity and (d) the far-field radiation patterns at various emission powers. At threshold, the gain in the active layer is distributed according to the diffusion of carriers in the absence of hole burning.

For the symmetric waveguide, the dimensions are $l_1 = l_2 = 2$ μm while for the asymmetric case, $l_1 = 2$ μm, and $l_2 = 1.7$ μm. This range of values is not atypical for our fabrication process. Differences in lengths l_1 and l_2 arise during fabrication as discussed earlier and can be associated with, for example, the crystal orientation so that both chemical etch rates and meltback rates can be different for the two sloping walls of the channel. Other effects of asymmetries can arise due to the asymmetrical growth of AlGaAs in the sloping channels.

When $l_1 = l_2$, Fig. 3, the carriers are distributed symmetrically about the center of the waveguide while for $l_1 > l_2$, Fig. 4(b), the carriers are "pushed" to the side of the waveguide with the steeper channel slope. The redistribution of the carriers with drive affect the gain-induced refractive index as shown in Figs. 3(a) and 4(a). In Fig. 4(a), the effective index perturbation is drastically reduced along the negative y direction which causes the optical field to shift in the positive y direction with drive as much as 0.25 μm at

Table I

	Cladding Layers	Active Region	Substrate
Mole Fraction AlAs	0.30	0.07	0.0
Refractive Index	3.40	3.62	3.64
Absorption Coefficient	10 cm^{-1}	--	5000 cm^{-1}

λ = 0.83 μm (lasing wavelength)

d_2 0.06 μm (active layer thickness)

$B^2 = 10^{-12}$ cm^3/sec (bimolecular coefficient)

L_D = 3 μm (carrier diffusion length)

$\tau_s = 3 \times 10^{-9}$ sec (carrier lifetime)

R_1 = 0.32
R_2 = 0.85 (facet reflection coefficients)

d_c = 0.4 μm (ηclad layer thickness outside of the channel)

y_0 = 0.5 μm (current decay parameter)

S = 4 μm (stripe width)

L = 250 μm (device length)

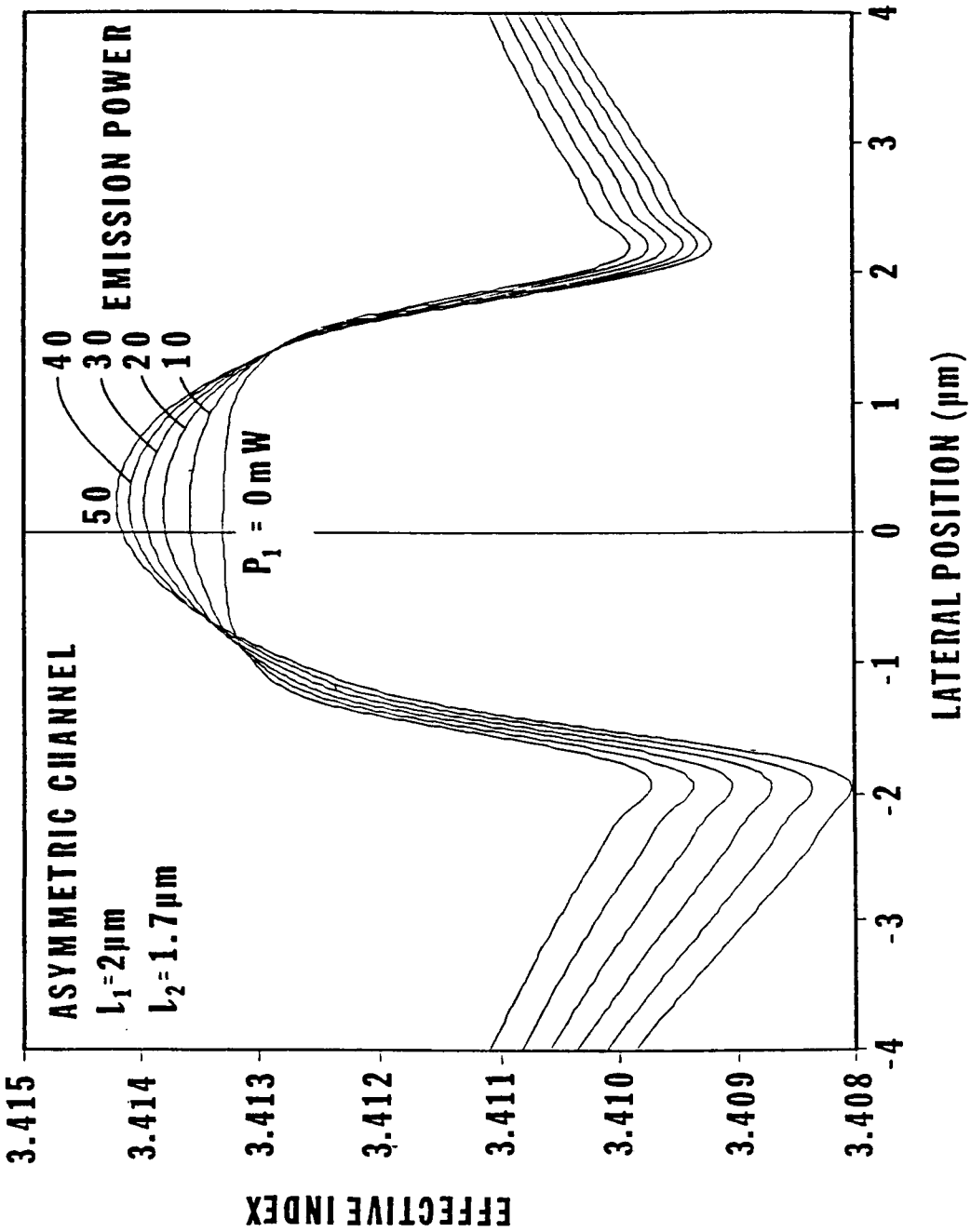

Fig. 4(a)

Fig. 4. Calculated a) lateral effective index profiles, b) lateral gain profiles in the active layer, c) near field intensity distributions, and d) far field intensity patterns for an asymmetric CSP-DH structure (l_1 = 2.0 μm and l_2 = 1.7 μm) with a 4 μm wide Zn diffusion front for output powers of 0, 10, 20, 30, 40, and 50 mW.

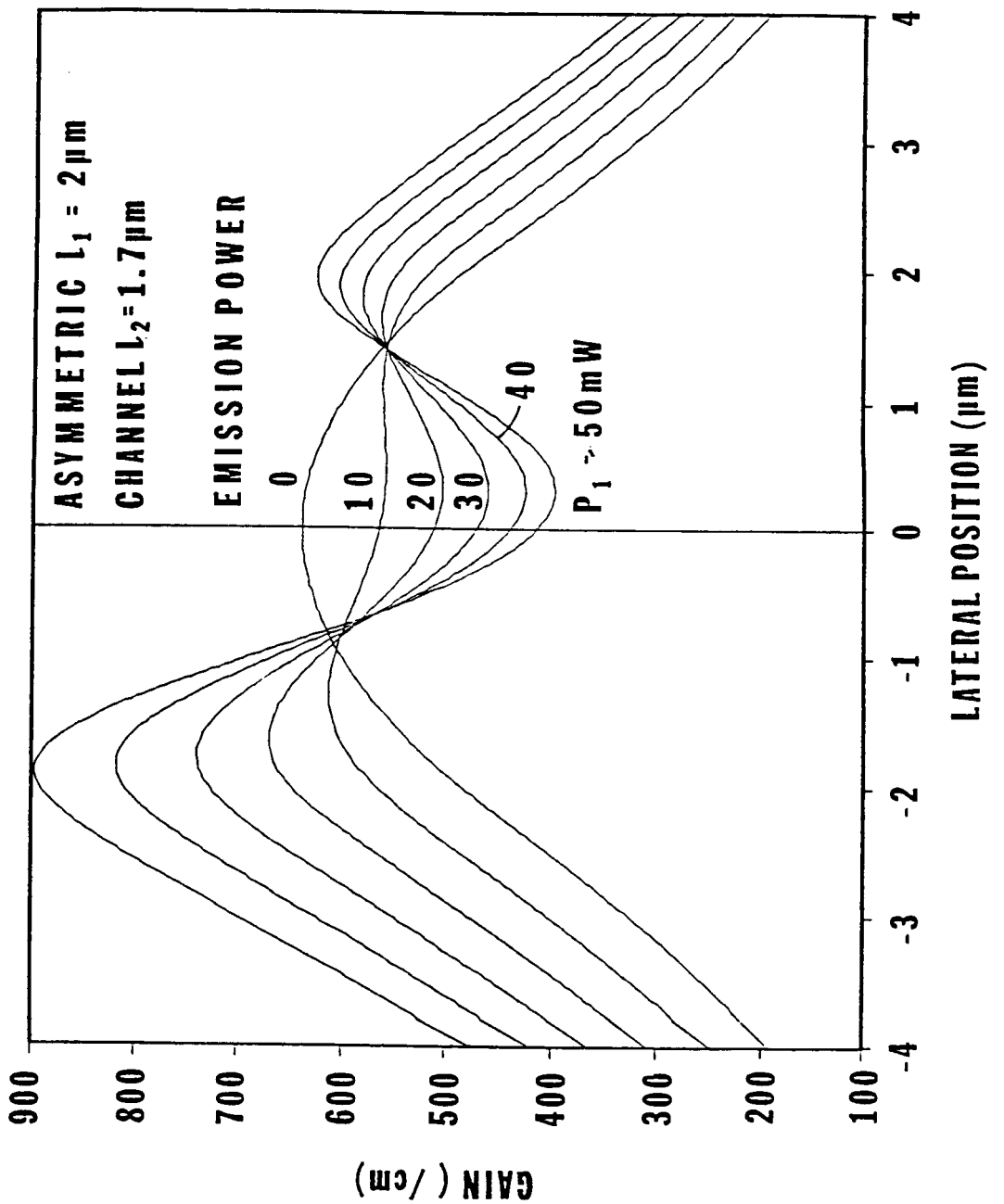
ASYMMETRIC L_1 = 2μm
CHANNEL L_2=1.7μm
EMISSION POWER
0
10
20
30
40
P_1 ~ 50mW
GAIN (/cm)
LATERAL POSITION (μm)
900
800
700
600
500
400
300
200
100
-4
-3
-2
-1
0
1
2
3
4

Fig. 4(b)

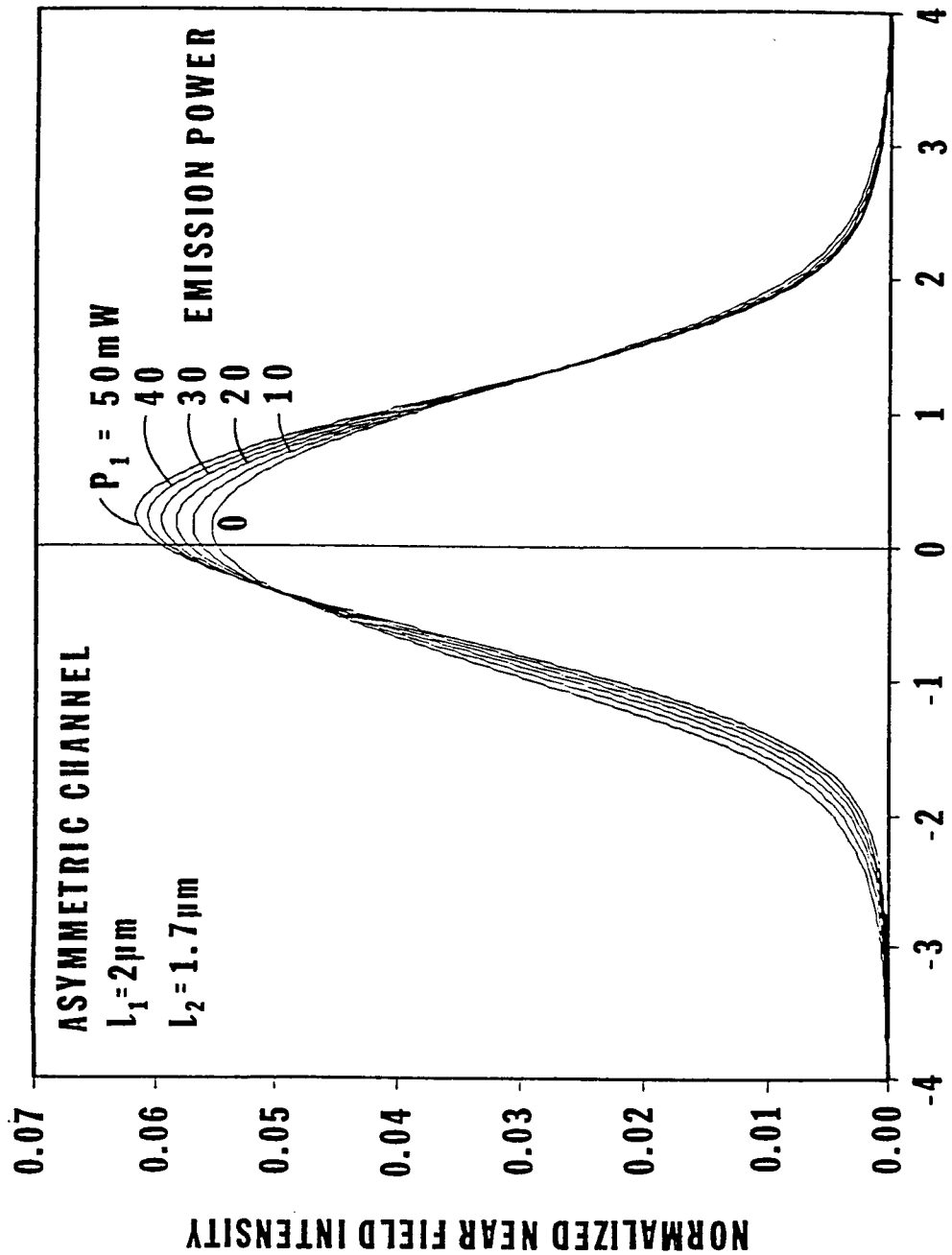
ASYMMETRIC CHANNEL
L1=2μm
L2=1.7μm
P1 = 50mW
40
30
20
10
0
EMISSION POWER
NORMALIZED NEAR FIELD INTENSITY
LATERAL POSITION (μm)
0.07
0.06
0.05
0.04
0.03
0.02
0.01
0.00
-4
-3
-2
-1
0
1
2
3
4

Fig. 4(c)

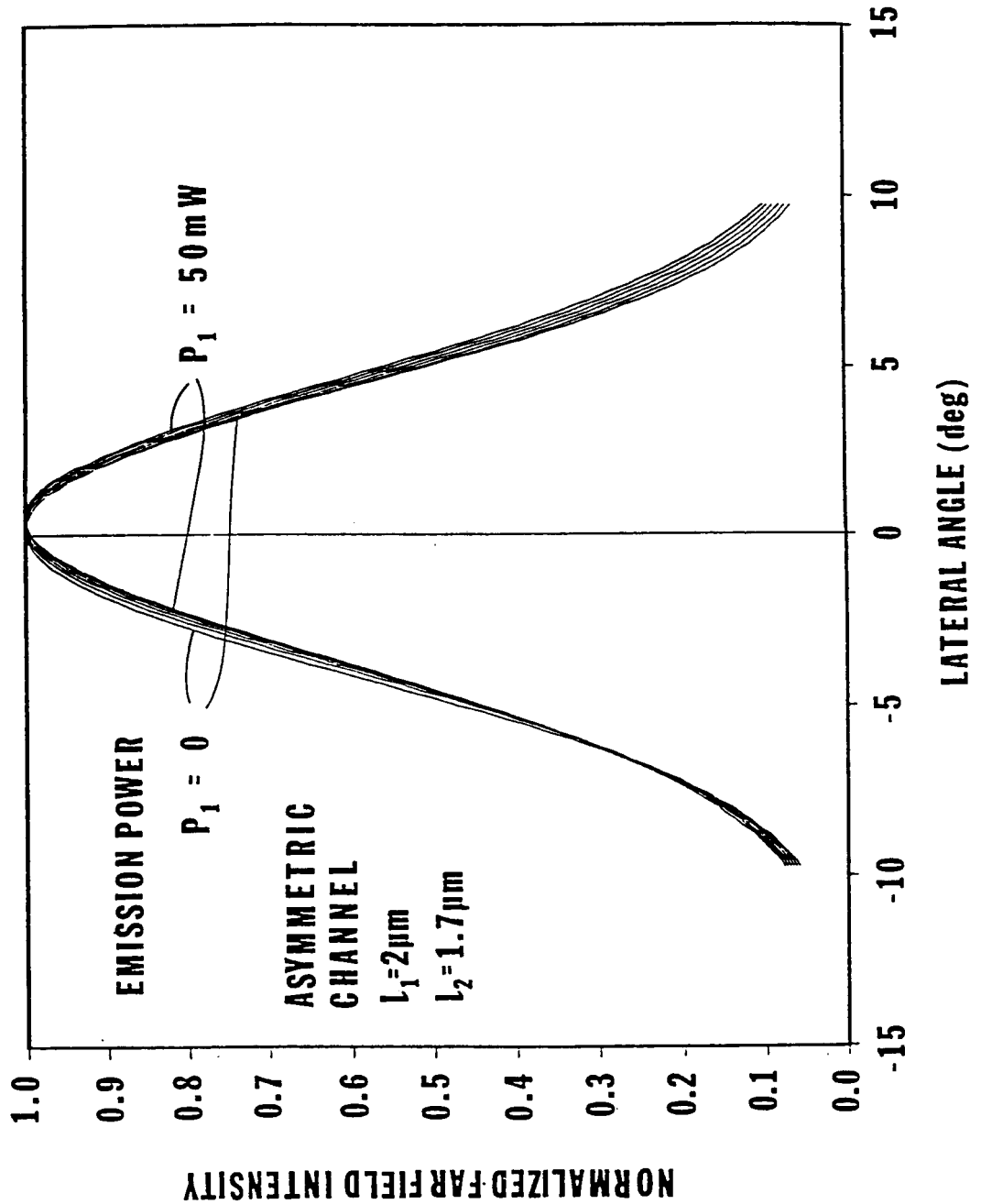
NORMALIZED FAR FIELD INTENSITY
1.0
0.9
0.8
0.7
0.6
0.5
0.4
0.3
0.2
0.1
0.0
-15
-10
-5
0
5
10
15
LATERAL ANGLE (deg)
EMISSION POWER
P1 = 0
P1 = 50 mW
ASYMMETRIC
CHANNEL
l1=2μm
l2=1.7μm

Fig. 4(d)

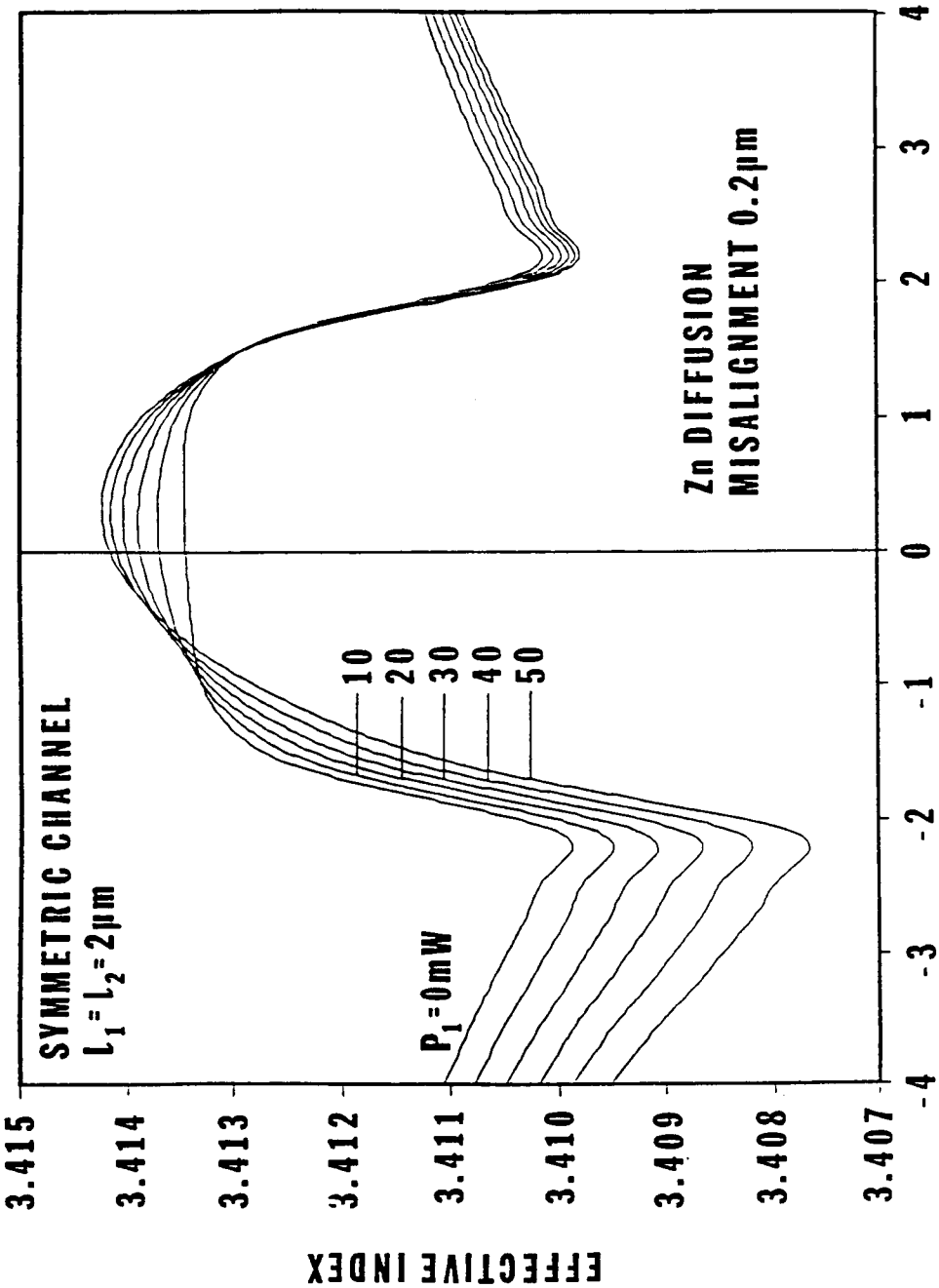

Fig. 5(a)

Fig. 5. Calculated a) lateral effective index profiles, b) lateral gain profiles in the active layer, c) near field intensity distributions, and d) far field intensity patterns for a symmetric CSP-DH structure with a misaligned 4 μm wide Zn diffusion front for output powers of 0, 10, 20, 30, 40, and 50 mW. The Zn diffusion is centered at y = - 0.2 μm.

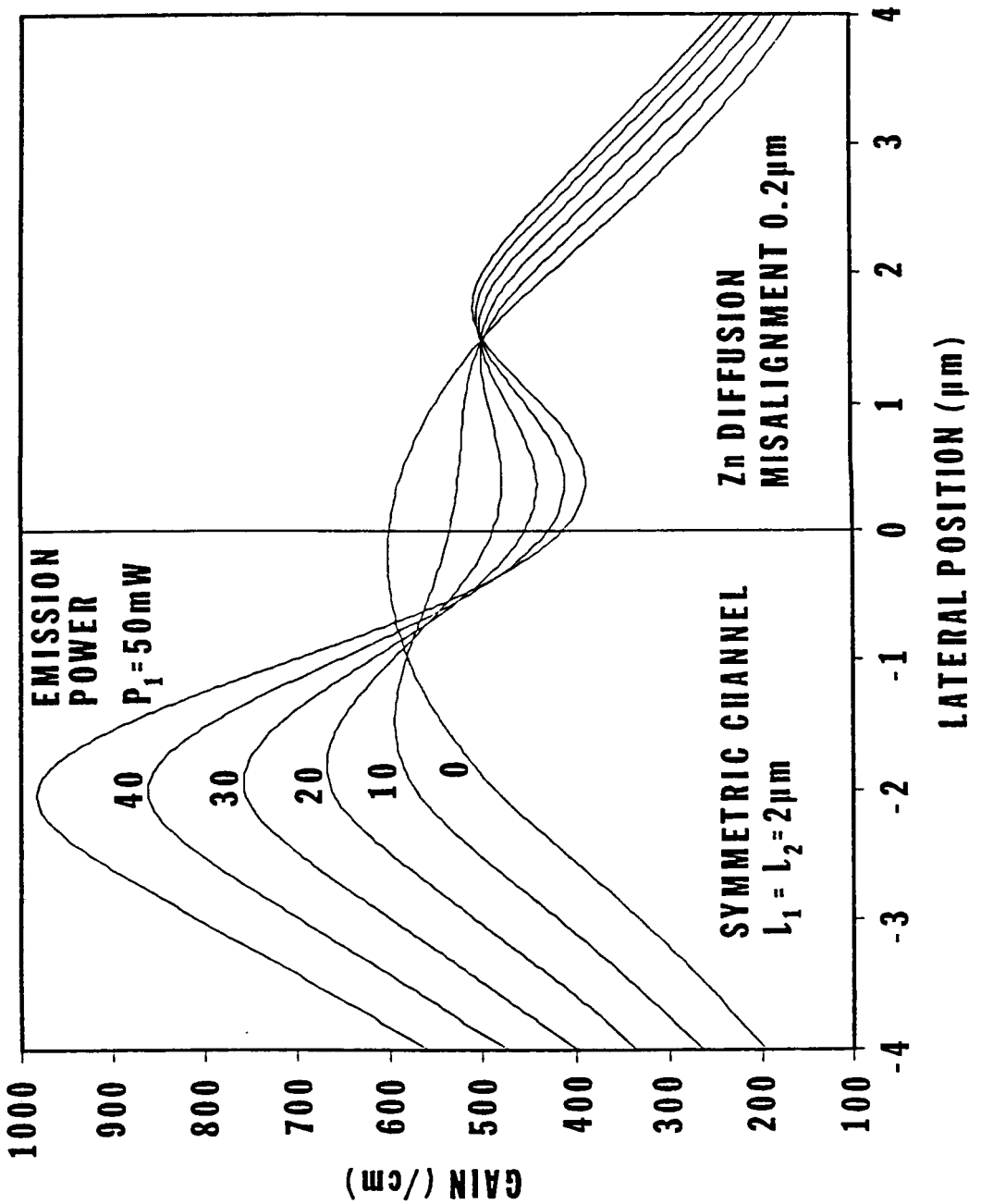
EMISSION POWER
P_1=50mW
40
30
20
10
0
SYMMETRIC CHANNEL
$L_1 = L_2$=2μm
Zn DIFFUSION
MISALIGNMENT 0.2μm
GAIN (/cm)
LATERAL POSITION (μm)
1000
900
800
700
600
500
400
300
200
100
-4
-3
-2
-1
0
1
2
3
4

Fig. 5(b)

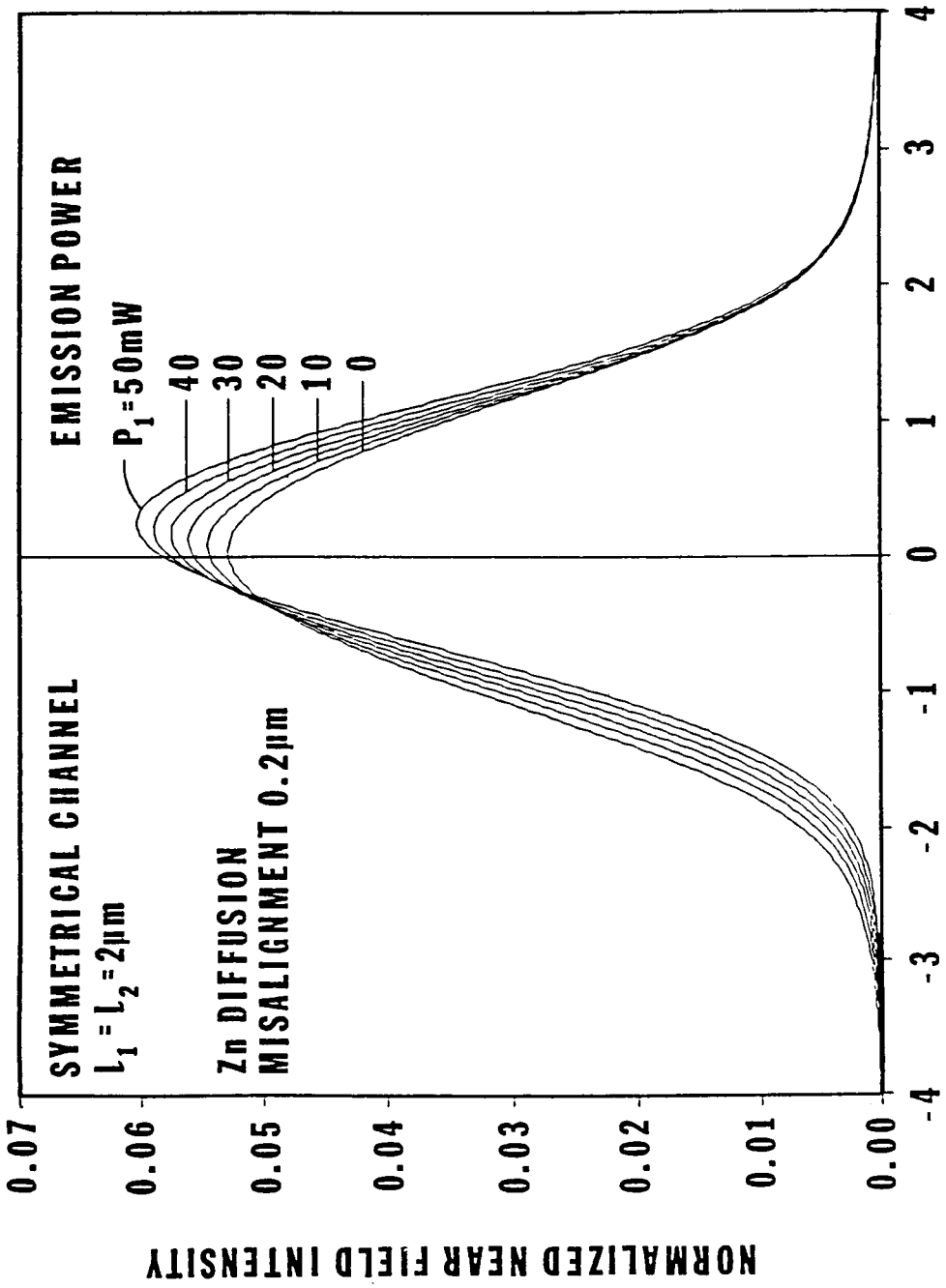
SYMMETRICAL CHANNEL
$L_1 = L_2 = 2\mu m$
Zn DIFFUSION
MISALIGNMENT 0.2μm
EMISSION POWER
P_1=50mW
40
30
20
10
0
NORMALIZED NEAR FIELD INTENSITY
LATERAL POSITION (μm)
0.07
0.06
0.05
0.04
0.03
0.02
0.01
0.00
-4
-3
-2
-1
0
1
2
3
4

Fig. 5(c)

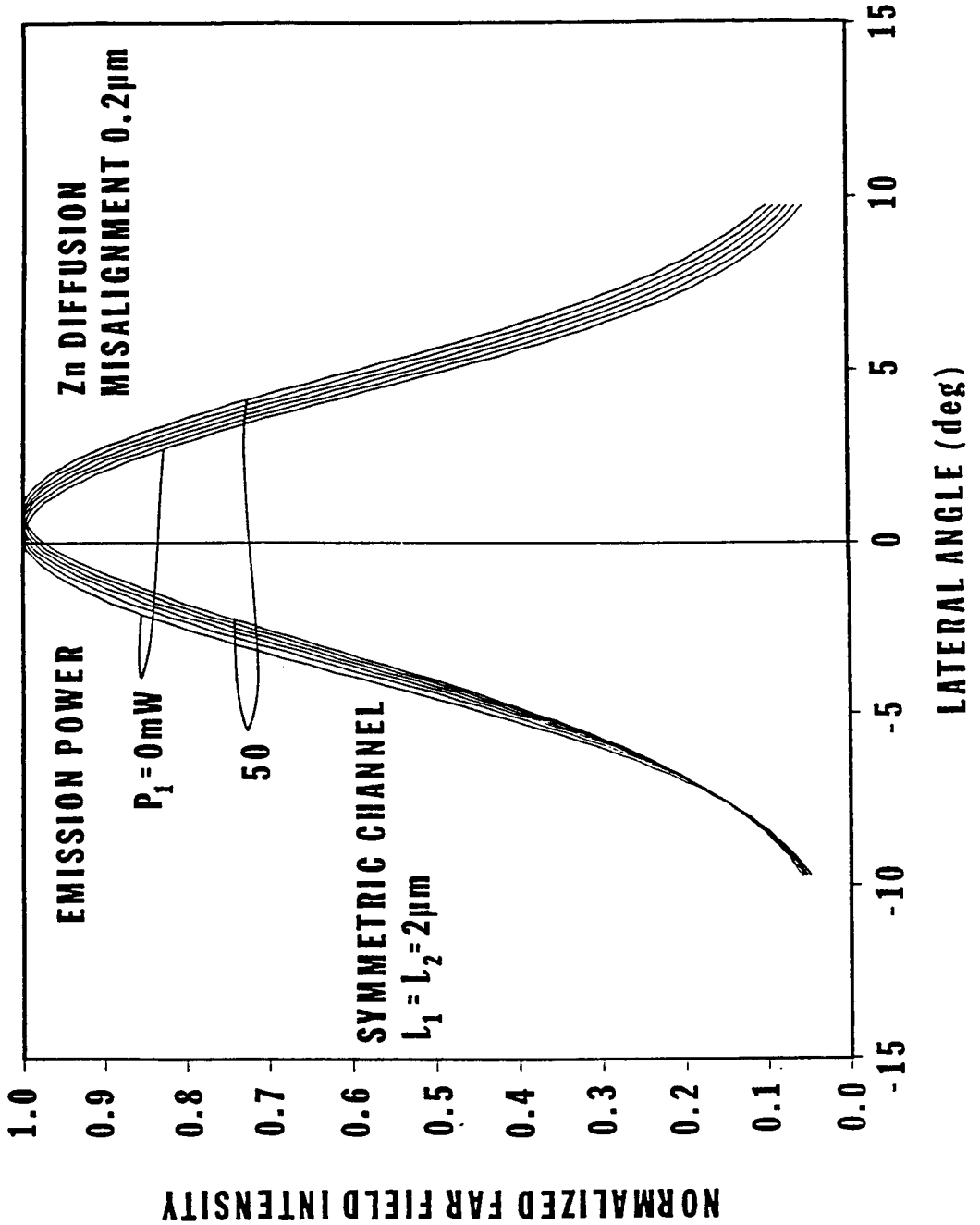
Zn DIFFUSION
MISALIGNMENT 0.2μm
EMISSION POWER
P1 = 0mW
50
SYMMETRIC CHANNEL
L1 = L2 = 2μm
NORMALIZED FAR FIELD INTENSITY
LATERAL ANGLE (deg)
1.0
0.9
0.8
0.7
0.6
0.5
0.4
0.3
0.2
0.1
0.0
-15
-10
-5
0
5
10
15

Fig. 5(d)

50 mW as shown in Fig. 4(c). The corresponding far-field radiation patterns are shown in Figs. 3(d) and 4(d). Note that for the symmetric structure, the far-field peak is stable with drive while for the asymmetric structure, it shifts as much as 0.5^{o} at 50 mW. Far-field shifts occur because the gain induced refractive index perturbation is relatively large compared to the "built-in" effective index profile of the CSP laser. On the other hand, if the "built-in" effective index is large compared to the gain-induced index perturbations, the near- and far-fields should be relatively stable with drive. In both the symmetric and asymmetric channel cases, the FWHP of the far-field pattern increases because of self focusing effects of the near field.

Figs. 5, 6, and 7 illustrate the effects of misalignment of the Zn diffused region relative to the center of the channel. In Fig. 5, the 4 μm wide diffusion front is displaced 0.2 μm along the negative y direction, resulting in about a 0.25 μm shift in the near field intensity peak as the laser power increases from threshold to 50 mW with a corresponding shift of about 0.75^{o} in the far field pattern peak. To illustrate the effects of increased misalignment the same 4 μm wide Zn diffused region is displaced a 0.5 μm to the left of the channel in Fig. 6. In this device, the total emission power of the fundamental mode could not be increased above approximately 30 mW at current levels above 125 mA. At higher drive currents, the device would very likely oscillate in a high-order lateral mode (which we have observed experimentally) although we have not examined higher order mode mixing in our numerical computations. Nevertheless, single mode operation cannot be obtained at powers above the 30 mW level. The major reason for this power limitation is that the gain distribution, Fig. 6(b), becomes highly asymmetrical. The major increase in the gain distribution occurs at $y \sim -2$ μm where the gain level reaches 1400 cm^{-1}. The peak optical field in the laser shifts towards the positive y direction, reducing the interaction of the lasing mode with the gain and preventing saturation of the the spontaneous emission. The near field peak shifts about 0.6 μm while the corresponding far-field peak moves about

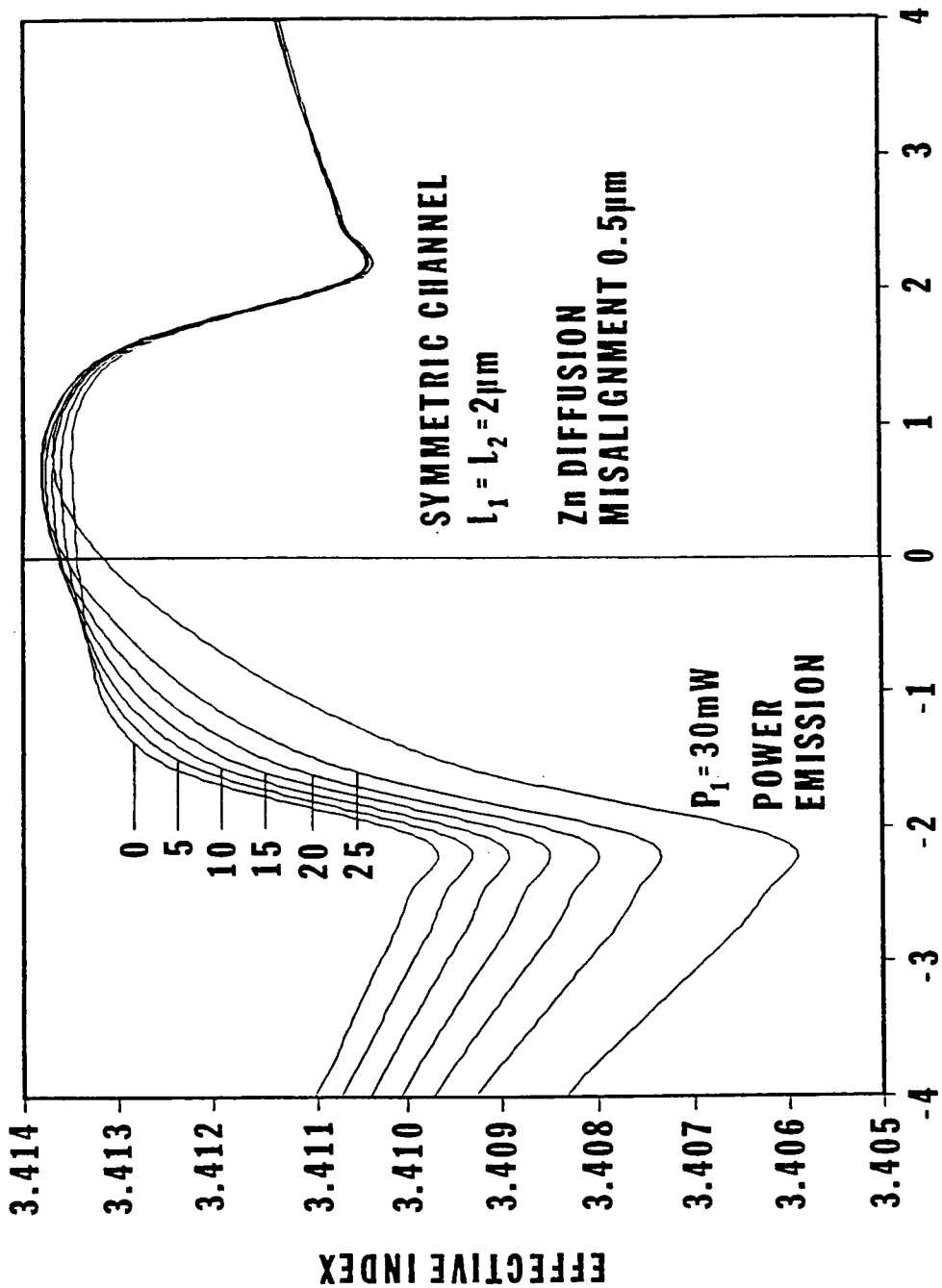

Fig. 6(a)

Fig. 6. Calculated a) lateral effective index profiles, b) lateral gain profiles in the active layer, c) near field intensity distributions, and d) far field intensity patterns for a symmetric CSP-DH structure (l_1 = 2.0 μm and l_2 = 2.0 μm) with a misaligned 4 μm wide Zn diffusion front for output powers of 0, 5, 10, 15, 20, 25, and, 30 mW. The Zn diffusion is centered at x = -0.5 μm.

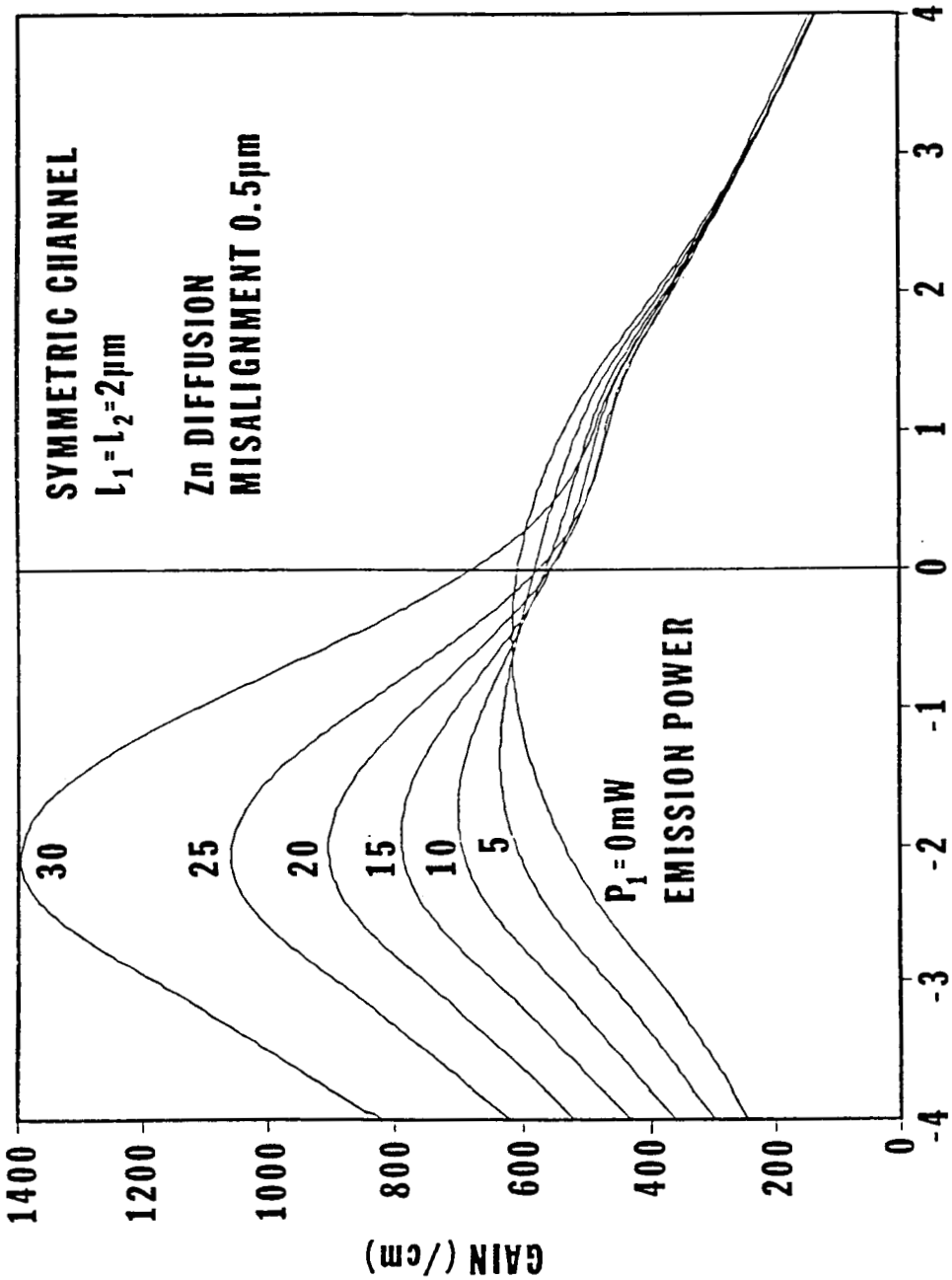
SYMMETRIC CHANNEL
$l_1 = l_2 = 2\mu m$
Zn DIFFUSION
MISALIGNMENT 0.5μm
30
25
20
15
10
5
$P_1 = 0mW$
EMISSION POWER
GAIN (/cm)
1400
1200
1000
800
600
400
200
0
-4
-3
-2
-1
0
1
2
3
4
LATERAL POSITION (μm)

Fig. 6(b)

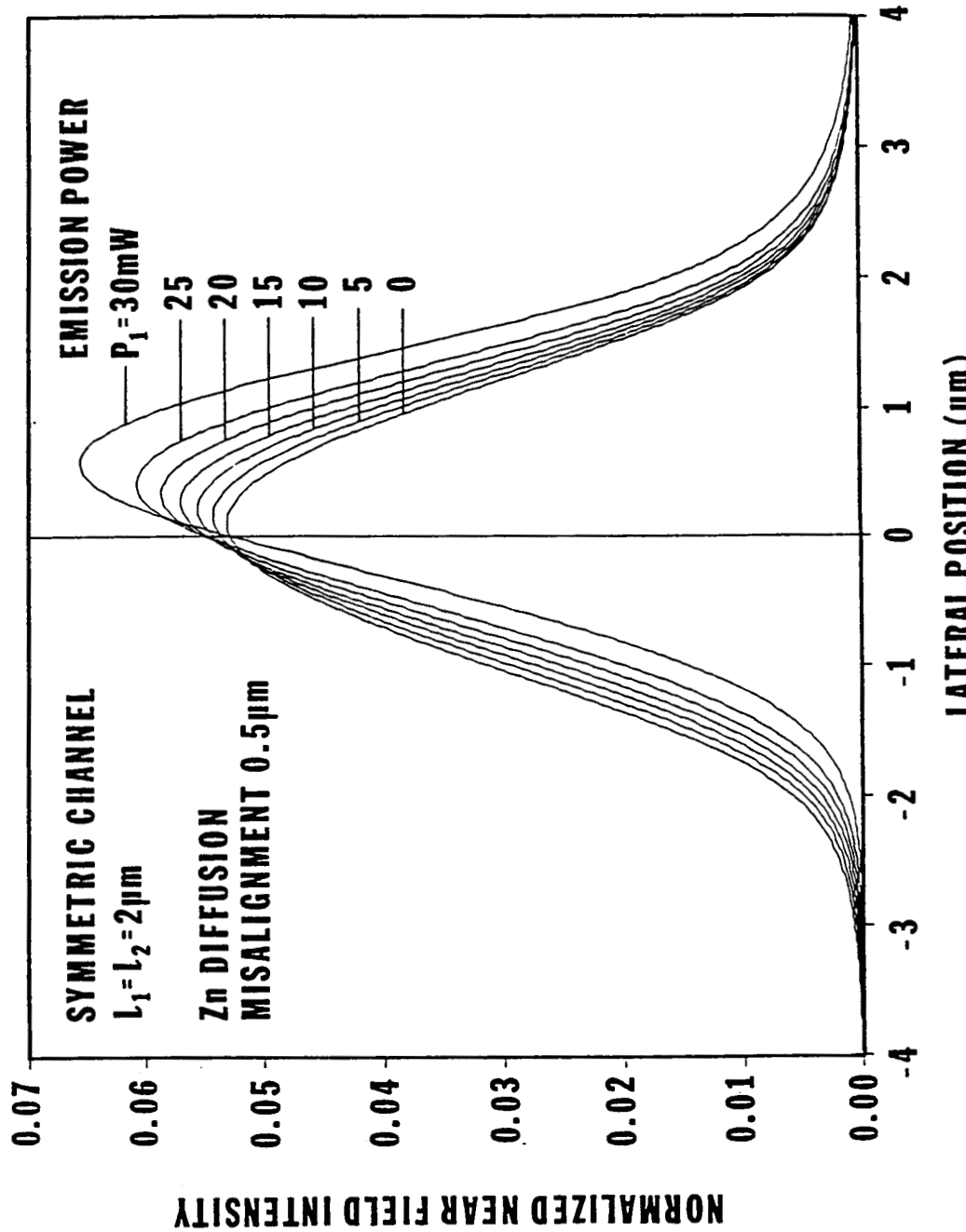
SYMMETRIC CHANNEL
$L_1=L_2=2\mu m$
Zn DIFFUSION
MISALIGNMENT 0.5μm
EMISSION POWER
$P_1=30mW$
25
20
15
10
5
0
NORMALIZED NEAR FIELD INTENSITY
LATERAL POSITION (μm)
0.00
0.01
0.02
0.03
0.04
0.05
0.06
0.07
-4
-3
-2
-1
0
1
2
3
4

Fig. 6(c)

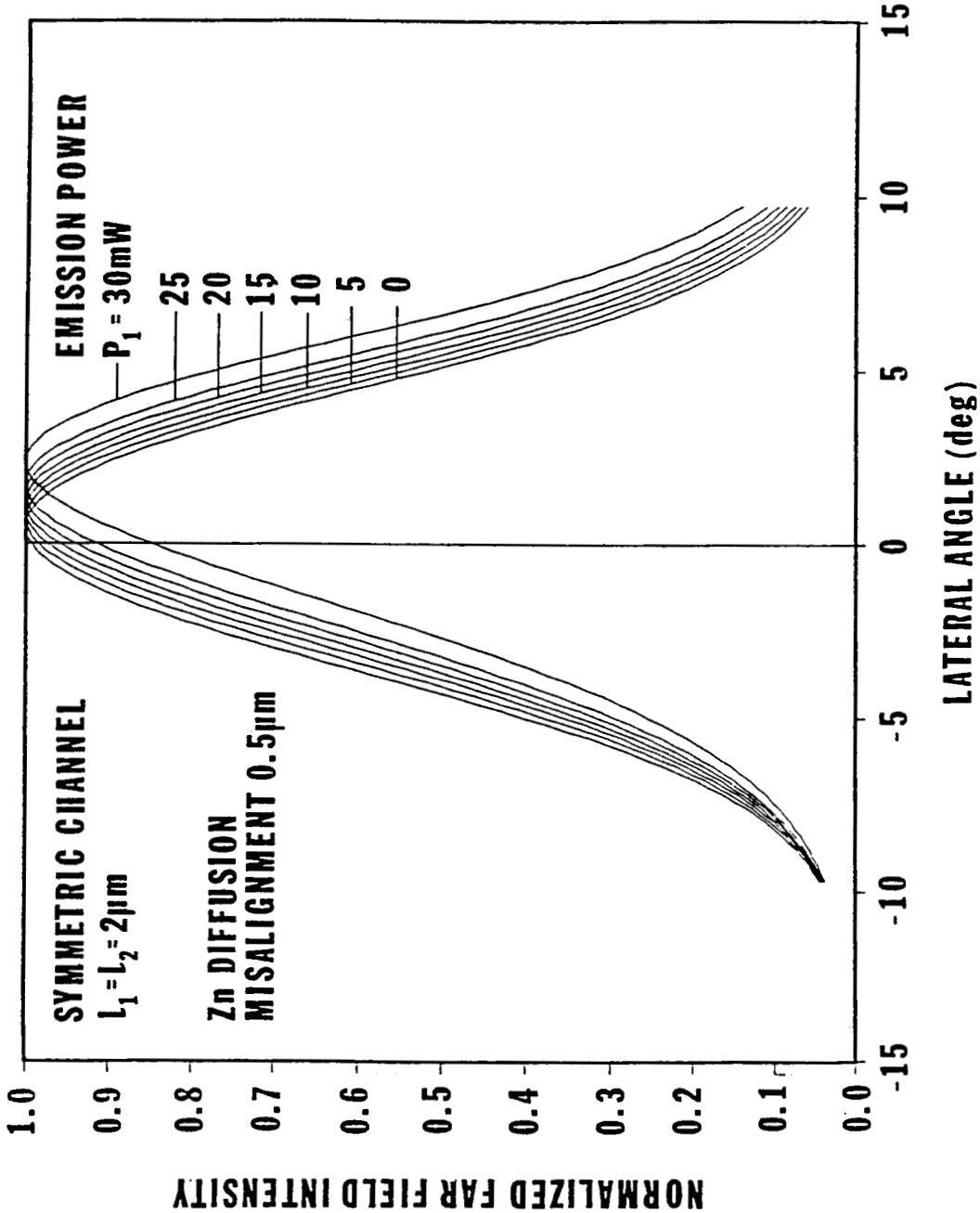
SYMMETRIC CHANNEL
$l_1 = l_2 = 2\mu m$
Zn DIFFUSION
MISALIGNMENT 0.5μm
EMISSION POWER
P_1 = 30mW
25
20
15
10
5
0
NORMALIZED FAR FIELD INTENSITY
LATERAL ANGLE (deg)
1.0
0.9
0.8
0.7
0.6
0.5
0.4
0.3
0.2
0.1
0.0
-15
-10
-5
0
5
10
15

Fig. 6(d)

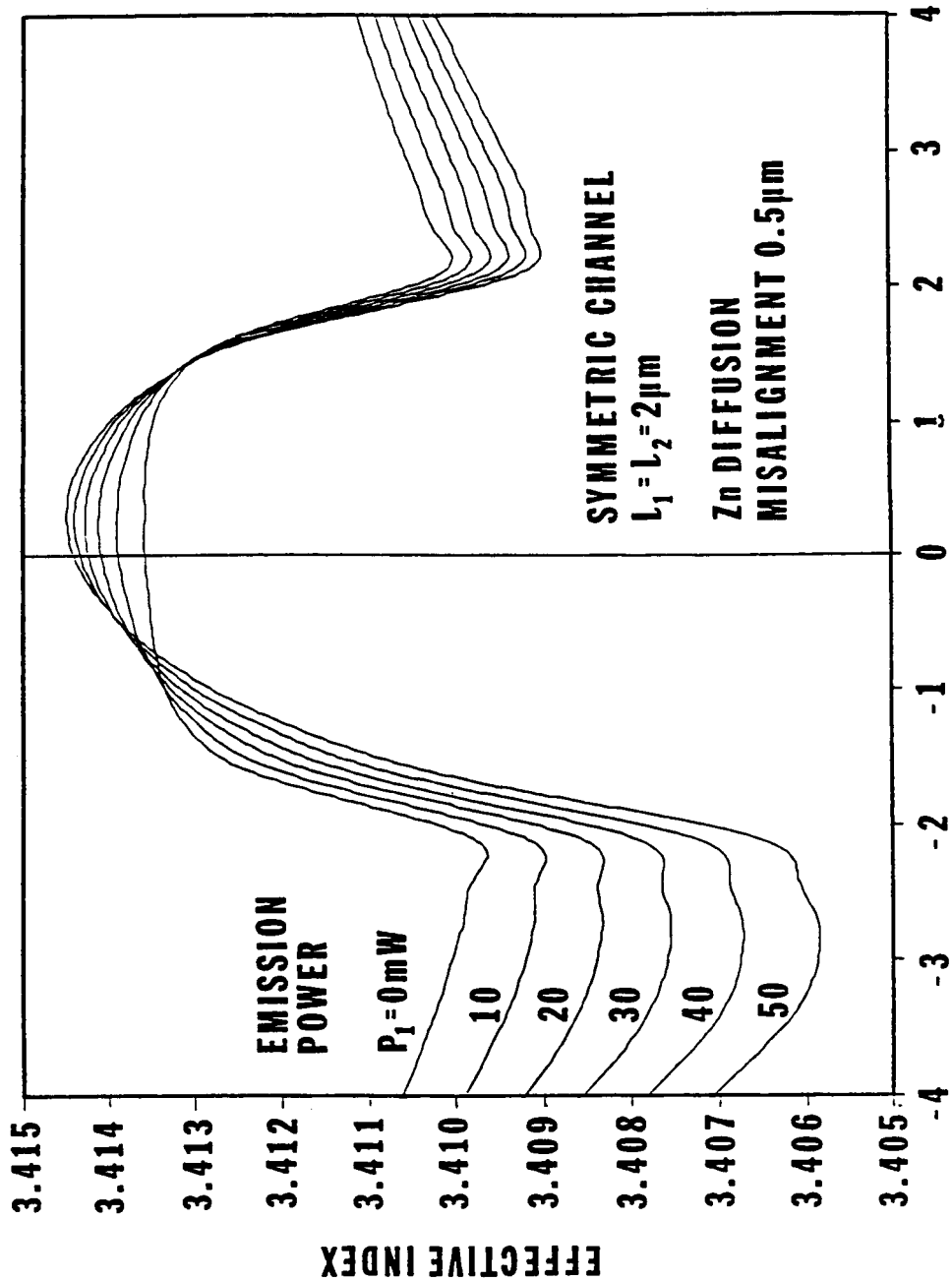

Fig. 7(a)

Fig. 7. Calculated a) lateral effective index profiles, b) lateral gain profiles in the active layer, c) near field intensity distributions, and d) far field intensity patterns for a symmetric CSP-DH structure (L_1 = 2.0 μm and L_2 = 2.0 μm) with a 6 μm wide Zn diffusion front for output powers of 0, 10, 20, 30, 40, and 50 mW. The Zn diffusion is centered at y = - 0.5 μm.

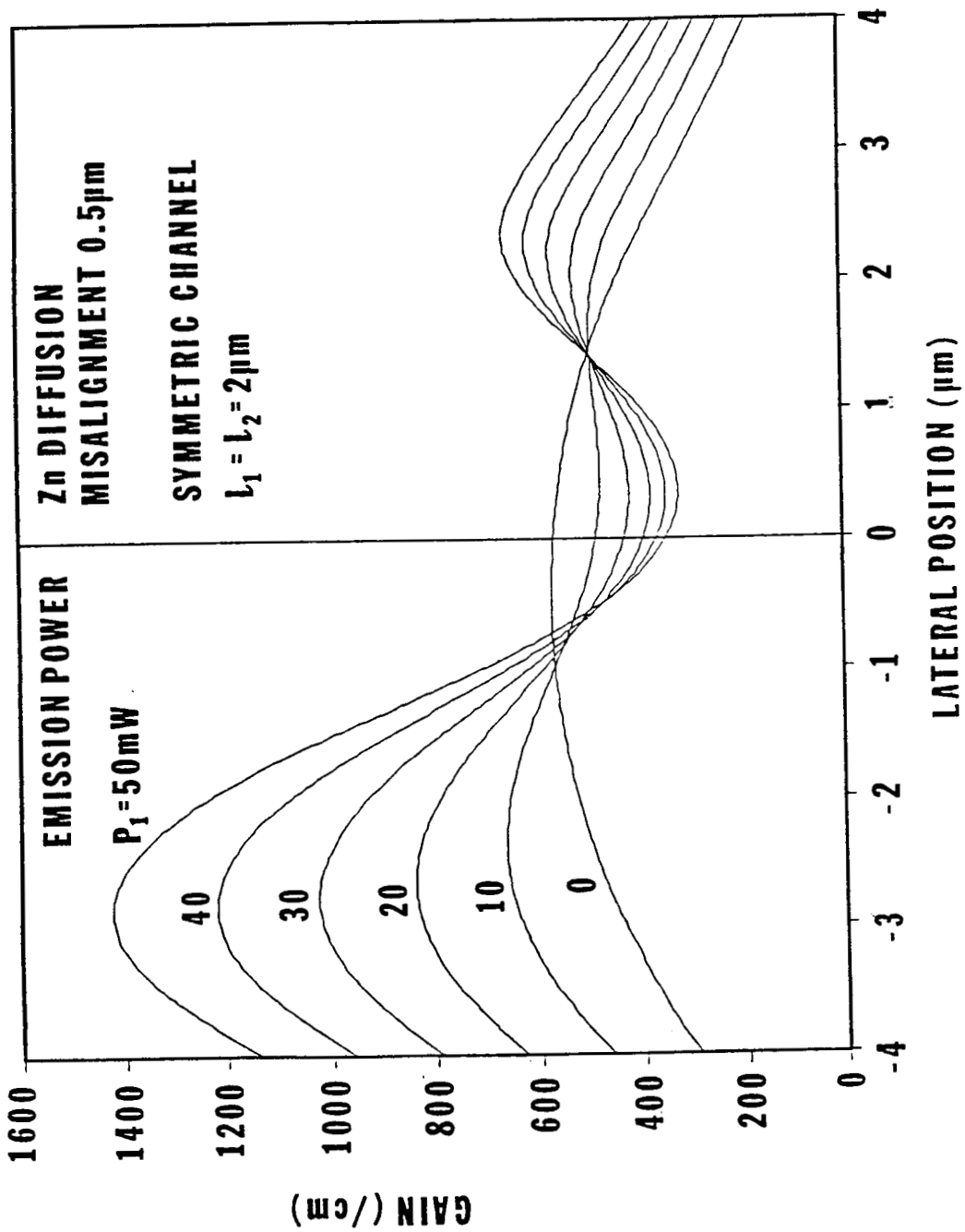
EMISSION POWER
P_1=50mW
40
30
20
10
0
Zn DIFFUSION
MISALIGNMENT 0.5μm
SYMMETRIC CHANNEL
$L_1 = L_2$= 2μm
GAIN (/cm)
LATERAL POSITION (μm)
1600
1400
1200
1000
800
600
400
200
0
-4
-3
-2
-1
0
1
2
3
4

Fig. 7(b)

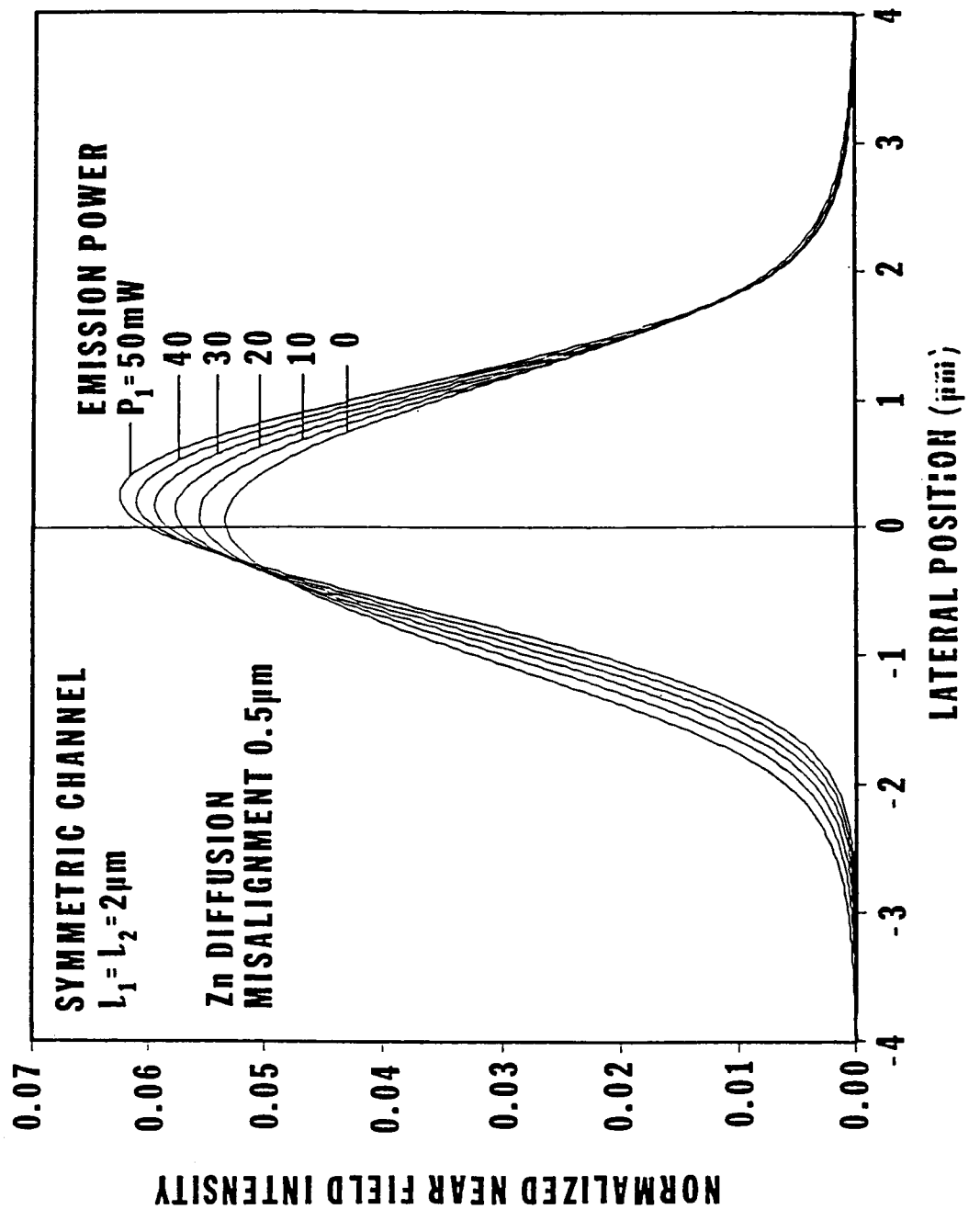
SYMMETRIC CHANNEL
$L_1 = L_2 = 2\mu m$
Zn DIFFUSION
MISALIGNMENT 0.5μm
EMISSION POWER
$P_1 = 50mW$
40
30
20
10
0
NORMALIZED NEAR FIELD INTENSITY
LATERAL POSITION (μm)
0.07
0.06
0.05
0.04
0.03
0.02
0.01
0.00
-4
-3
-2
-1
0
1
2
3
4

Fig. 7(c)

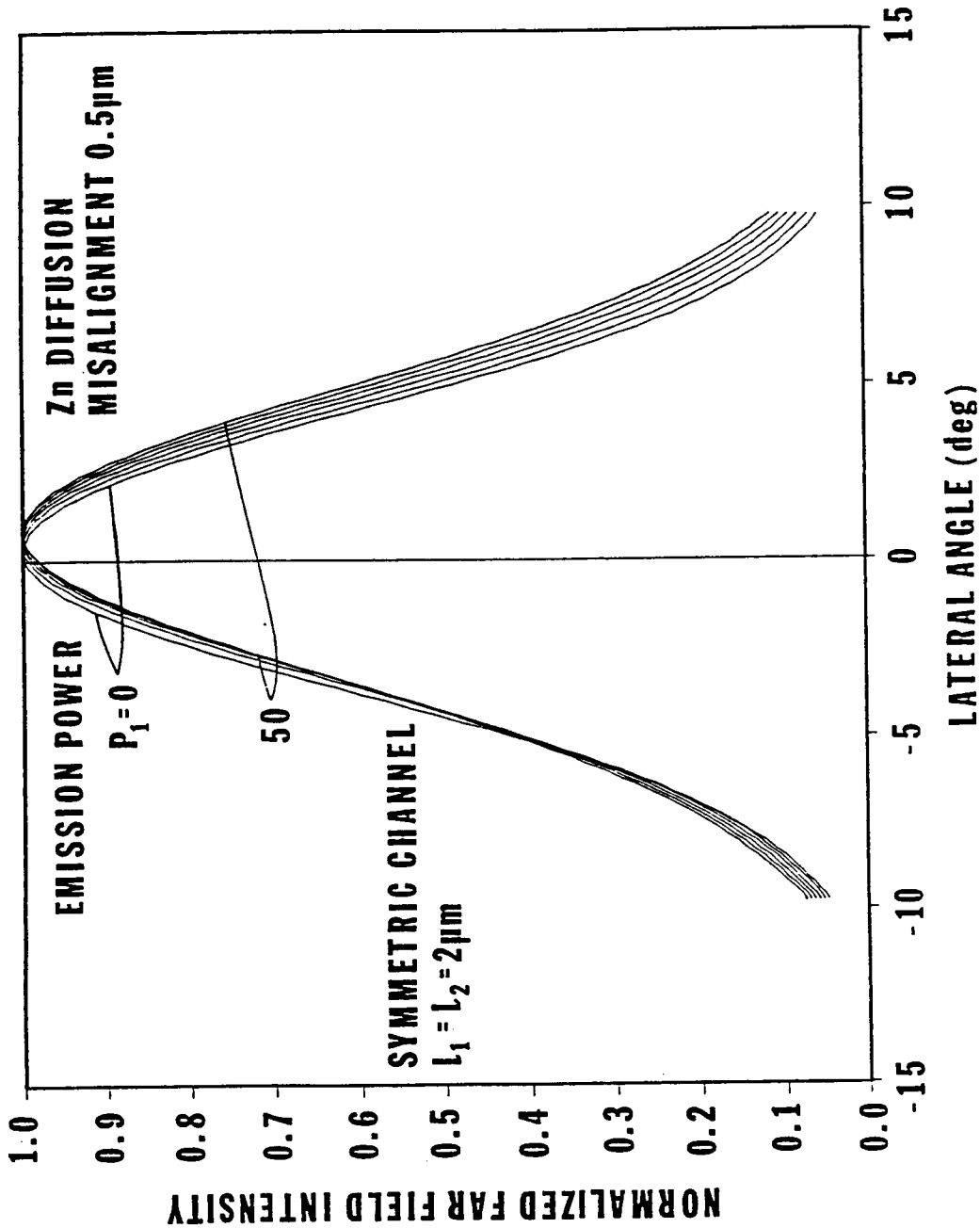
Zn DIFFUSION
MISALIGNMENT 0.5μm
EMISSION POWER
P1=0
50
SYMMETRIC CHANNEL
L1=L2=2μm
NORMALIZED FAR FIELD INTENSITY
LATERAL ANGLE (deg)
1.0
0.9
0.8
0.7
0.6
0.5
0.4
0.3
0.2
0.1
0.0
-15
-10
-5
0
5
10
15

Fig. 7(d)

2.5° as the output power increases from threshold to 30 mW for this case. In order to temper the effects of misalignment, we widened the Zn front to 6 μm.

Fig. 7 shows the effects of a 0.5 μm displacement of the wider Zn region in the negative y direction. In this case, the near field peak moves approximately 0.25 μm and the lateral far-field peak shifts about 0.8° between 0 and 50 mW of emission power, which is comparable to the field shifts shown in Fig. 5. Therefore, the effect of a 0.2 μm misalignment of a 4 μm diffusion front is comparable to a 0.5 μm misalignment of a 6 μm diffussion front, both over 4 μm wide channels.

In Fig. 8 (a), the calculated values of the optical emission from the front facet (front facet reflectivity $R_1 = 0.32$, rear facet reflectivity $R_2 = 0.85$) for the four cases described in Figs. 3, 4, 5, and 7 as a function of the device drive current whose distribution is given by Eq. (7) is shown. In the computations, we have assumed the internal quantum efficiency is unity and there is no loss of carriers transversing heterojunctions. Therefore, the current axis can be scaled to account for known leakage in realistic devices. Both the threshold currents and slope efficiencies are different for the different cases. For the symmetric case $I_{th} = 22$ mA while it is approximately 24 mA for the asymmetric one. Note that increasing the Zn diffusion front from 4 μm to 6 μm result in only a slight decrease in external differential quantum efficiency. Fig. 8 (b) shows an experimental P-I curve of a typical CSP laser with minimal asymmetries and with geometry, composition, and facet coatings comparable to the numerical examples. Experimentally, thresholds as low as 37 mA were measured.

The resulting emission power versus drive current for the case discussed in Fig. 6 (0.5 μm displacement of a 4 μm diffusion front) is shown in Fig. 9 which shows saturation of the output power as the peaks of the near field intensity and the lateral gain distribution are increasingly physically displaced with increasing drive current.

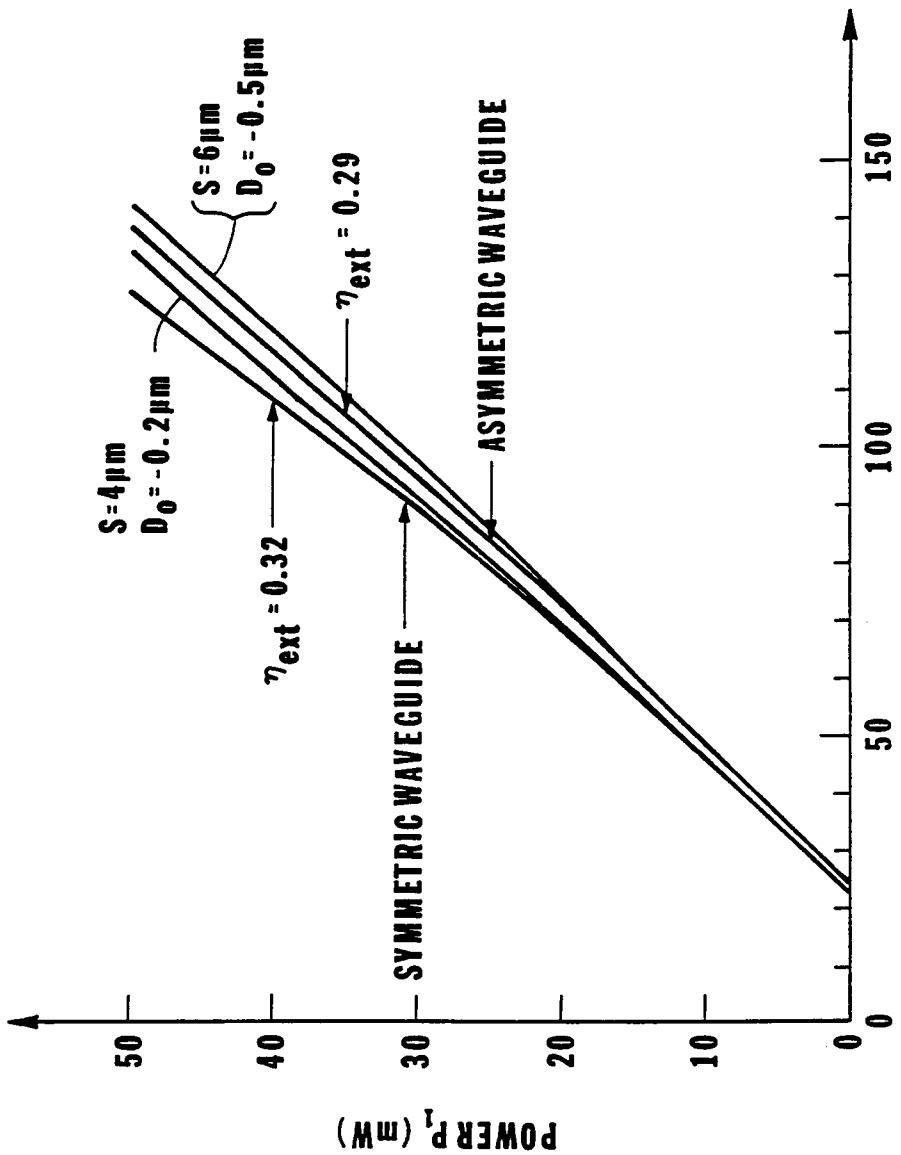

Fig. 8(a)

Fig. 8. a) Calculated power versus current curves for a CSP-DH structure with 1) a symmetric (l_1 = 2.0 μm and l_2 = 2.0 μm) channel, symmetric 4μm wide diffusion front (....); 2) an asymmetric (l_1 = 2.0 μm and l_2 = 1.7 μm) channel, symmetric 4μm wide diffusion front (....); 3) a symmetric (l_1 = 2.0 μm and l_2 = 2.0 μm) channel, misaligned 4μm wide diffusion front centered at y = -0.2 μm (....); and 4) a symmetric (l_1 = 2.0 μm and l_2 = 2.0 μm) channel, misaligned 6 μm wide diffusion front centered at y = -0.5 μm (....). The device geometry is shown in Fig.1 and the numerical parameters given in Table 1. b) Experimentally measured power versus current curve for a CSP-DH laser.

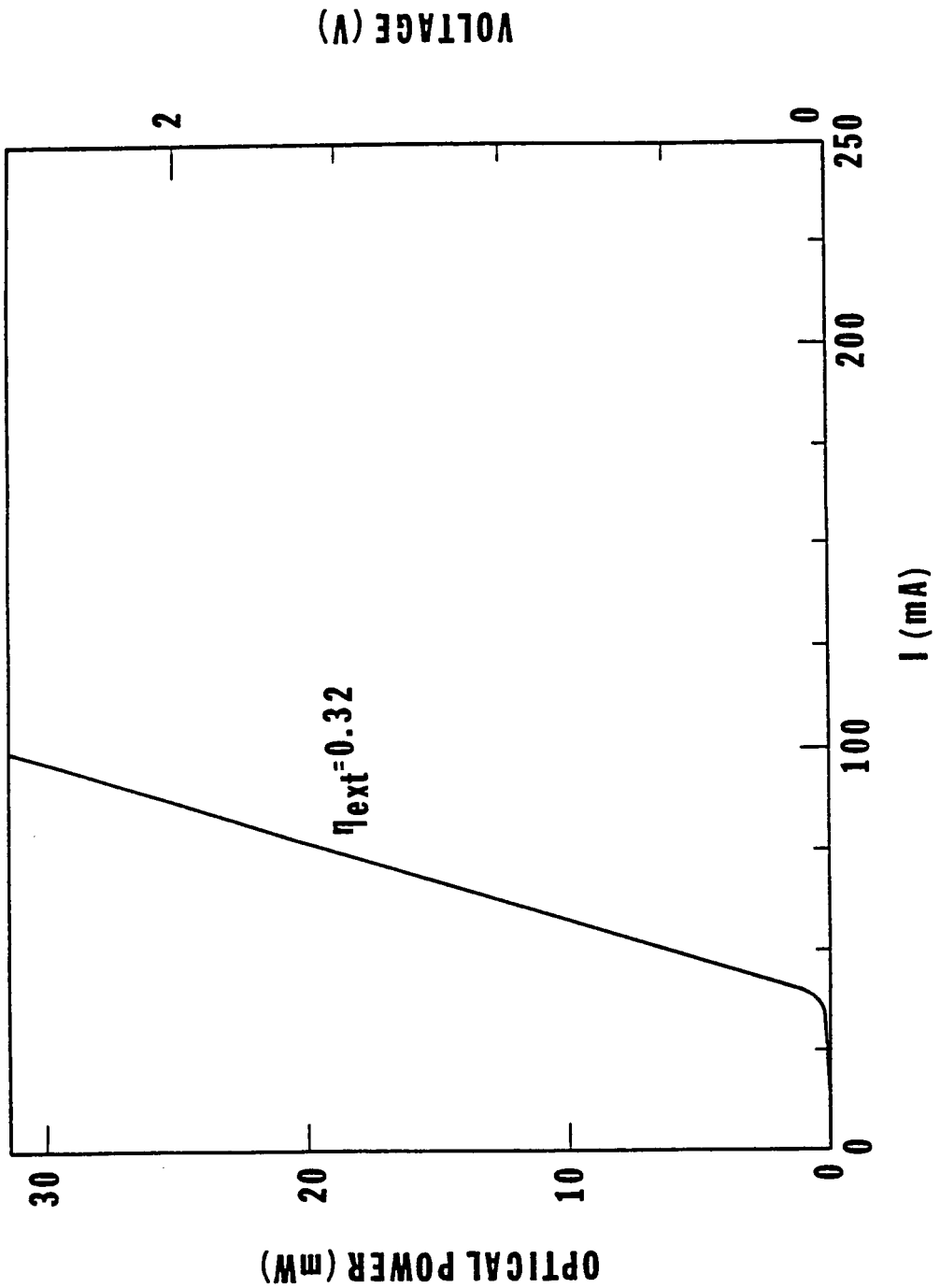
VOLTAGE (V)
2
0
250
200
100
I (mA)
η_{ext}=0.32
30
20
10
0
0
OPTICAL POWER (mW)

Fig. 8(b)

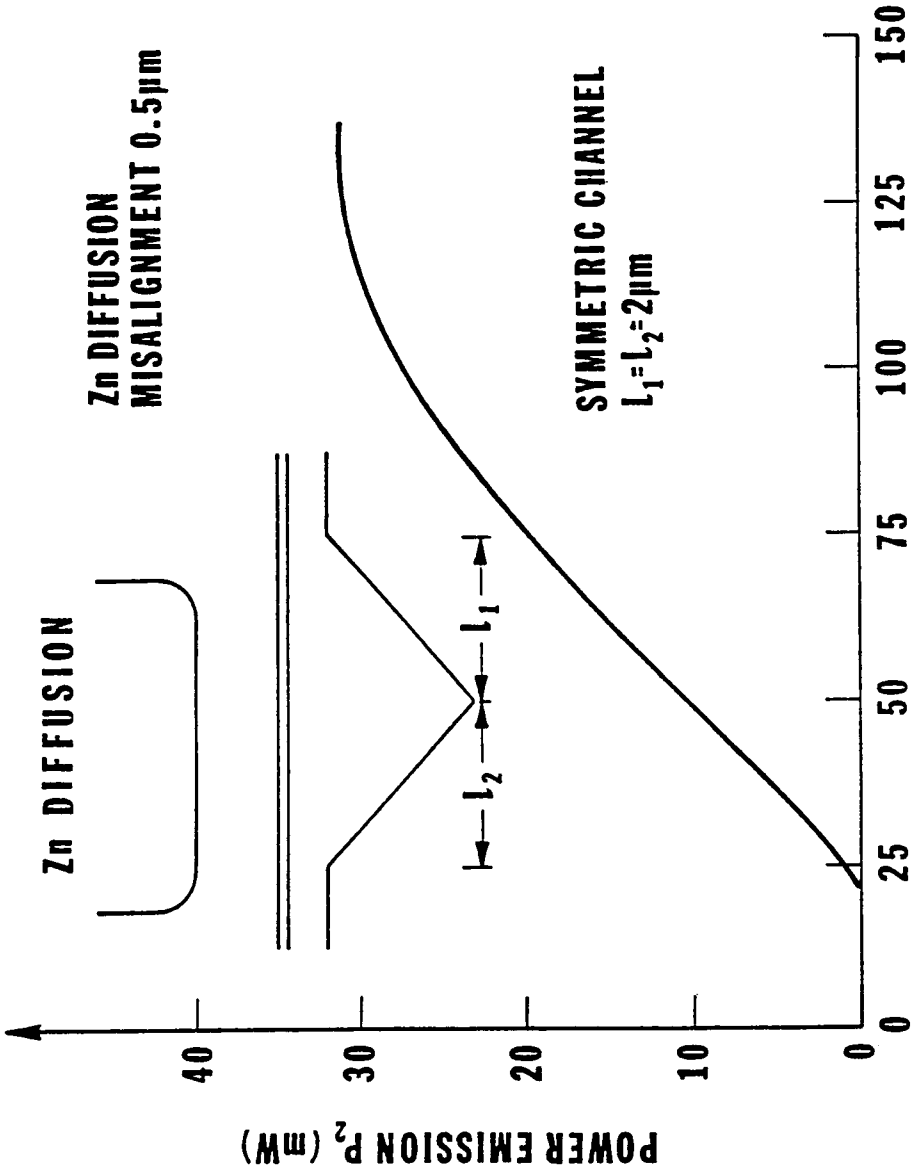

Fig. 9. Calculated power versus current curves for a CSP-DH structure with a symmetric (l_1 = 2.0 μm and l_2 = 2.0 μm) channel, and a 4 μm wide diffusion front which is offset from the channel by 0.5 μm.

CONCLUSION

A comprehensive model of the CSP-DH laser structure fabricated with sloping v-groove channels is developed. The laser characteristics are computed using a self-consistent calculation of the optical field and of the electron/hole distribution in the active layer of the laser. These are the first detailed computations that show how small asymmetries due to device fabrication can significantly affect the optical and electrical properties of the CSP-DH laser.

Many applications of semiconductor lasers require both near- and far-field stability with drive current. Asymmetries in device structures studied in this paper show that near field movements as much as one μm and far field pattern shifts as much as 3^{o} can occur.

The most serious asymmetry introduced here occurs because of Zn diffusion misalignment. The effect of misalignments on the performance can be minimized by making the Zn diffusion region wider than the channel at the expense of only a slight decrease of efficiency. Additionally, these calculations show the neccessity of precisely positioning the Zn diffusion region even when the diffusion front is wider than the channel. CSP-DH lasers fabricated with blocking layers [19-21] have self-aligned current confinement and are not vulnerable to Zn diffusion misalignment. However, nonuniformities in the blocking layers will have the same effect as Zn diffusion misalignment.

The effects of asymmetries of the type discussed here are particularly pronounced when the CSP-DH type lasers are designed to have a weak lateral index guiding mechanism. Weak index guiding produces optical modes with broad lateral near fields that have a low peak optical intensity for a given power level. However, strong index-guided structures, while less sensitive to power dependent field shifts, require small spot sizes with

corresponding higher peak power densities to maintain single lateral mode operation. High-power lasers with weak index guided structures require device geometries with minimal asymmetries in order to produce lasers with characteristics that are insensitive to drive current.

Acknowledgements

We are indebted to N. Dinkel for the growth of the lasers, E. DePiano, D. Tarangioli, and M. Harvey for laser processing, and to M. Ettenberg, J. Hammer, B. Hershenov and S. Palfrey for a critical review of the manuscript. This work was supported in part by the National Aeronautics and Space Administration under contract number NAS1-17441.

REFERENCES

1. J. Buus, "A model for the static properties of DH lasers," IEEE J. Quan Electron., Vol. QE-15, pp. 734-739, Aug. 1979.

2. R. Lang, "Lateral transverse mode instability and its stabilization in stripe geometry injection lasers," IEEE J. Quan. Electron., Vol. QE-15, pp. 718-726, Aug. 1979.

3. W. Streifer, D. R. Scifres and R. D. Burnham, "Above-threshold analysis of double-heterojunction diode lasers with laterally tapered active regions," Appl. Phys. Lett., Vol. 37, pp. 877-879, Nov. 15, 1980.

4. W. Streifer, D. R. Scifres and R. D. Burnham, "Channelled substrate non planar laser analysis, Part II: Lasers with tapered active regions," IEEE J. Quan. Electron., Vol. QE-17, pp. 1521-1530, 1981.

5. W. Streifer, D. R. Scifres and R. D. Burnham, "Channelled substrate non planar laser analysis, Part I: for modulation," IEEE J. Quan. Electron., Vol. QE-17, pp. 736-744, 1981.

6.) M. Ueno, R. Lang, S. Matsumoto, H. Kawano, T. Furuse and I. Sakuma, "Optimum designs for InGaAsP/InP (λ = 1.3 μm) planoconvex waveguide lasers under lasing conditions," IEE Proc., Vol 129, Pt I, pp. 218-228, Dec. 1982.

7. S. Wang, C. Y. Chen, A. S. Liao and L. Figueroa, "Control of mode behavior in semiconductor lasers," IEEE J. Quan. Electron., Vol. QE-17, pp. 453-468, April 1981.

8. K. A. Shore, "Above-threshold current leakage effects in stripe-geometry injection lasers," Opt. and Quantum Electron., 15, pp. 371-379, 1983.

9. G. P. Agrawal, "Lateral analysis of quasi-index guided injection lasers: transitions from gain to index guiding," IEEE J. Lightwave Technol., LT-2, pp. 537-543, Aug. 1984.

10. J. Buus, "Principles of semiconductor laser modelling," IEE Proc. J., Vol. 132, pp. 42-51, Feb. 1985.

11. B. Goldstein, M. Ettenberg, N. A. Dinkel, and J. K. Butler, "A high-power channeled-substrate-planar AlGaAs laser," Appl. Phys. Lett. 47, pp. 655-657, Oct. 1, 1985.

12. J. K. Butler and D. Botez, "Mode characteristics of nonplanar double-heterojunction and large-optical-cavity laser structures," IEEE J. Quan. Electron., Vol QE-18, pp. 952-961, June, 1982.

13. J. K. Butler and D. Botez, "Lateral mode discrimination and control in high-power single-mode diode lasers of the large-optical-cavity (LOC) type," IEEE J. Quan. Electron., Vol. QE-20, pp. 879-891, Aug. 1984.

14. J. Manning and R. Olshansky, "The Carrier-Induced Index Change in AlGaAs and 1.3 μm InGaAs Diode Lasers," IEEE J. Quan Electron., QE-19, 10, pp. 1525-1530, October 1983.

15. V. Asder, J. Christiansen, and R. D. Russel, "COLSYS - a collocation code for boundary value problems," Codes for Boundary Value Problems, B. Childs et. al. Eds., Lecture Notes in Computer Science, 76, New York: Springer-Verlag, 1979.

16. W. B. Joyce, "Role of the conductivity of the confining layers in DH-laser spatial hole burning effects," IEEE J. Quan. Electron., QE-18, pp. 2005-2009, December 1982.

17. H. Yonezu, I. Sakuma, K. Kobayashi, T. Kamejima, M. Ueno, and Y. Nannichi, "A GaAs/AlGaAs double heterostructure planar stripe laser," Japan J. Appl. Phys., vol. 12, pp. 1585-1592, 1973.

18. F. Stern, "Calculated spectral dependence of gain in excited GaAs," J. Appl. Phys., Vol. 47, pp. 5382-5386, Dec. 1976.

19. S. Yamamoto, N. Miyauchi, S. Maei, T. Morimoto, O. Yamamoto, S. Yano, and T. Hijikata, "High output power characteristics in broad-channeled substrate inner stripe lasers," 46, pp. 319-321, Feb. 15, 1985.

20. T. Shibutani, M. Kume, K. Hamada, H. Shimizu, K. Itoh, G. Kano, and I. Teramoto, "A Novel High-Power Laser Structure with Current-Blocked Regions near Cavity Facets," IEEE J. Quan. Electron., to be published.

21. K. Uomi, S. Nakatsuka, T. Ohtoshi, Y. Ono, N. Chinone, and T. Kajimura, "High-power operation of index-guided visible GaAs/GaAlAs multiquantum well lasers," Appl. Phys. Lett. 45 (8), 15 October 1984 pp. 818-821.

FIGURE CAPTIONS

1. The CSP-DH laser structure; a) idealized model, b) scanning electron micrograph illustrating channel assymetries, and c) scanning electron micrograph illustrating misalignment of the zinc diffusion with the channel.

2. Flow chart summarizing the numerical calculations for laser oscillation above threshold.

3. Calculated a) lateral effective index profiles, b) lateral gain profiles in the active layer, c) near field intensity distributions, and d) far field intensity patterns for a symmetric CSP-DH structure (l_1 = 2.0 μm and l_2 = 2.0 μm) with a 4 μm wide Zn diffusion front for output powers of 0, 10, 20, 30, 40, and 50 mW.

4. Calculated a) lateral effective index profiles, b) lateral gain profiles in the active layer, c) near field intensity distributions, and d) far field intensity patterns for an asymmetric CSP-DH structure (l_1 = 2.0 μm and l_2 = 1.7 μm) with a 4 μm wide Zn diffusion front for output powers of 0, 10, 20, 30, 40, and 50 mW.

5. Calculated a) lateral effective index profiles, b) lateral gain profiles in the active layer, c) near field intensity distributions, and d) far field intensity patterns for a symmetric CSP-DH structure with a misaligned 4 μm wide Zn diffusion front for output powers of 0, 10, 20, 30, 40, and 50 mW. The Zn diffusion is centered at y = - 0.2 μm.

6. Calculated a) lateral effective index profiles, b) lateral gain profiles in the active layer, c) near field intensity distributions, and d) far field intensity patterns for a symmetric CSP-DH structure (l_1 = 2.0 μm and l_2 = 2.0 μm) with a misaligned 4 μm wide Zn diffusion front for output powers of 0, 5, 10, 15, 20, 25, and, 30 mW. The Zn diffusion is centered at y = - 0.5 μm.

7. Calculated a) lateral effective index profiles, b) lateral gain profiles in the active layer, c) near field intensity distributions, and d) far field intensity patterns for a symmetric CSP-DH structure (L_1 = 2.0 μm and L_2 = 2.0 μm) with a 6 μm wide Zn diffusion front for output powers of 0, 10, 20, 30, 40, and 50 mW. The Zn diffusion is centered at y = - 0.5 μm.

8. a) Calculated power versus current curves for a CSP-DH structure with 1) a symmetric (l_1 = 2.0 μm and l_2 = 2.0 μm) channel, symmetric 4μm wide diffusion front (....); 2) an asymmetric (l_1 = 2.0 μm and l_2 = 1.7 μm) channel, symmetric 4μm wide diffusion front (....); 3) a symmetric (l_1 = 2.0 μm and l_2 = 2.0 μm) channel, misaligned 4μm wide diffusion front centered at y = -0.2 μm (....); and 4) a symmetric (l_1 = 2.0 μm and l_2 = 2.0 μm) channel, misaligned 6 μm wide diffusion front centered at y = -0.5 μm (....). The device geometry is shown in Fig. 1 and the numerical parameters given in Table 1. b) Experimentally measured power versus current curve for a CSP-DH laser.

9. Calculated power versus current curves for a CSP-DH structure with a symmetric (l_1 = 2.0 μm and l_2 = 2.0 μm) channel, and a 4 μm wide diffusion front which is offset from the channel by 0.5 μm.

TABLE HEADING

Table I CSP modelling parameters

Appendix C

Reprinted from SPIE Vol. 756—Optical Technologies for Space Communication Systems
© 1987 by the Society of Photo-Optical Instrumentation Engineers, Box 10, Bellingham, WA 98227-0010 USA

0.87 μm CSP DIODE LASERS FOR SPACEBORNE COMMUNICATIONS*

D. B. Carlin, G. N. Pultz, and B. Goldstein

RCA Laboratories
Princeton, NJ 08540

Abstract

Index-guided channeled-substrate-planar (CSP) AlGaAs diode lasers are being developed for reliable, high-power operation for use as sources in spaceborne optical communications sytems. Although most work on this AlGaAs structure has been aimed at optimizing preformance at output wavelengths less than 8400 Å, emission in the 8700 Å regime is also of interest. In particular, such wavelengths are required for use in the Direct Detection Laser Transceiver (DDLT), to be incorporated into NASA's Advanced Communications Technology Satellite (ACTS), in order to avoid absorption of the light by the atmosphere when communicating with ground-based terminals. Lowest order spatial mode and substantially single longitudinal mode output has been observed in 0.87 μm CSP devices in excess of 50 mW cw and 100 mW 50% duty-cycle, with rms phase-front aberrations measured to be ≅ λ/40.

Introduction

The development of diode laser technology has been stimulated by the obvious advantages of compact, efficient, potentially reliable and inexpensive sources for free space communications applications. The relatively short emission wavelength available from AlGaAs diode lasers allows the use of transmission optics of modest dimensions, thereby reducing the mass of spaceborne optical communications subsystems and, therefore, the mass of the satellite host which must be launched into orbit. The generation of well-collimated beams, with the use of narrow passband filters at the receiver, allows reduction of the probabilities of interference, jamming, or data interception. The high frequency of optical radiation allows communications at data rates far in excess of those achievable using rf and microwave systems. These characteristics make diode laser based optical communications systems of potential importance in both government and civilian free space communciations links.

NASA's Advanced Communications Technology Satellite (ACTS) is designed to incorporate optical transceivers to demonstrate satellite-to-ground and satellite-to-satellite communications using state-of-the-art diode lasers. ACTS will host a laser communications package (LCS) designed to demonstrate laser communications links using both heterodyne and direct detection techniques. Lincoln Laboratories has the prime responsibility for developing the LCS package, which includes the heterodyne detection experiment, the acquisition and tracking subsystems, and the interfaces with the satellite. Perkin-Elmer has been chosen to develop the optical systems required for the LCS. The data transmission optics are designed to operate at wavelengths between 8634 and 8734 Å, in part to avoid absorption of the signal by water vapor in the atmosphere.

NASA's Goddard Space Flight Center has recently solicited proposals for the fabrication of a Direct Detection Laser Transceiver (DDLT)[1] that can be integrated into the LCS package to allow a comprehensive set of direct detection optical communications experiments. The output beams of pairs of diode lasers will be combined using dichroic filters in order to achieve the total optical power required for all modes of system operation. The Goddard Space Flight Center has also been supporting the development of channeled-substrate-planar (CSP) AlGaAs diode lasers, operating in the required wavelength range for the LCS, at RCA Laboratories. The performance goals for the laser when used in the DDLT include reliable single spatial and longitudinal mode operation to at least 60 mW at a variety of modulation rates with a minimum device lifetime of 2000 hours. These formidable requirements are difficult to achieve even at wavelengths of 8000 to 8500 Å, the spectral regime in which most development of index-guided high-power AlGaAs devices has concentrated historically. Because the device must be altered to achieve the long wavelengths required for the DDLT, added development of the device is required.

0.87 μm CSP Laser Structure

CSP diode lasers are commercially available at moderately high output power levels (≤ 30 mW cw) at wavelengths between 8000 and 8500 Å. Devices of this type have achieved remarkable cw output performance at these wavelengths in the laboratory, including single spectral mode behavior to 90 mW, single spatial mode operation to 150 mW, and total emission to 190 mW[2]. In order to emit at wavelengths greater than 8500, however, the standard design of this device, fabricated by liquid phase epitaxy (LPE), must be altered.

Shown in Figure 1 is a schematic of a CSP structure designed to operate near 0.87 μm. The 800 Å-thick active layer is undoped GaAs. The emitting wavelength of pure GaAs is ≅ 8800 Å; a residual concentration of aluminum is present, however, which slightly reduces the wavelength, as required by the DDLT specifications. For lasers operating near 0.83 μm, this layer is typically $Al_{0.06}Ga_{0.94}As$. The n and p-confining layers of the long wavelength structure are composed of $Al_{0.27}Ga_{0.73}As$, a lower aluminum concentration than that in the

* Work supported in part by NASA under contract NAS1-17441.

standard CSP structure in order to effect an index of refraction step of the correct magnitude to confine the tranverse (perpendicular to the junction plane) spatial mode. The thickness of the p-confining layer is 1.5 μm while that of the n-confining layer is 0.3 μm away from the substrate. The channel in the substrate is ≅ 4.5 μm wide and ≅ 1.5 μm deep, formed in the $(01\bar{1})$ direction on a Si-doped n-type (100) GaAs substrate. The cap layer of n-GaAs is penetrated by a deep zinc diffusion, which is aligned over the channel, to produce the current confinement of the device. The contact metallizations are Ti-Pt-Au on the p-side and Au-Ge on the n-side of the device.

The effective index of refraction of the waveguide structure varies across the lateral dimension of the laser (parallel to the junction). The real part of the index is about 5×10^{-3} higher in the center of the device, immediately above the channel, than it is in the planar sections of the structure on either side of the channel regions. Since, in the latter regions, the GaAs substrate is only 0.3 μm from the active layer, modes propagate into the substrate and significant absorption of the laser light occurs due to the slightly smaller bandgap substrate material. Both of these effects, which are inherent to the structure and do not vary significantly with injection current, act to strongly confine the spatial mode of the laser in the channel region.

Laser Performance

Figure 2 shows the power-versus-current characteristics for a long wavelength CSP device under cw and 50% duty-cycle operating conditions. The rear facet of the laser is coated with a 90% reflectivity dilectric stack; the emitting facet has a 10% reflectivity coating. The lateral and transverse far-field intensity profiles are shown in Figure 3 under cw conditions at 25 and 50 mW and in Figure 4 under 50% duty-cycle modulated operation to 50 and 100 mW levels. Lowest order spatial mode operation is seen up to output powers approaching 100 mW 50% duty-cycle; a second spatial mode appears at that output level in the device shown. Spectra of the emission from this same device are shown at 50 mW cw and 100 mW 50% duty-cycle in Figures 5 and 6, respectively. The device operates in a single longitudinal mode under cw conditions. Approximately 75% of the energy is in the primary longitudinal mode, centered at 8640 Å for the device shown, under 50% duty-cycle modulation (bias current set to 90% of threshold).

Significant signal loss in a free-space communications link may result from aberrations in the collimated diode laser output beam. These aberrations may be due to the optical system forming the beam or atmospheric variations (in links between space and ground terminals), or to the diode laser source itself. Gain-guided devices emit output beams which are characterized as having substantial aberrations. In particular, they exhibit large amounts of astigmatism, which change as the power is varied and during modulated operation. It is, therefore, imperative to use index-guided diode laser sources to achieve diffraction limited performance. The phase fronts of collimated 0.87 μm CSP diode lasers have been experimentally measured using a LADITE computer-controlled Mach-Zehnder interferometer manufactured by Wyko, Inc[3]. Two-dimensional plots of the phase fronts are shown in Figure 7. These plots show the phase of the beam (vertical axis) as a function of location in the lateral (horizontal axis) and transverse (into the page) far-fields at four different output power levels up to 100 mW cw. The total rms phase aberrations measured less than ≅ λ/40 under all conditions, well below the level at which aberrations significantly decrease beam quality.

The DDLT must modulate the amplitude of the transmitted signal at data rates of up to 220 Mb/s. The laser itself does not limit system performance in this case; transition times on the order of a nanosecond are readily achieved[4]. For example, the measured response of a 60 mW peak power CSP diode laser to a 500 Mb/s Manchester encoded input signal is shown in Figure 8.

The emission wavelength of each diode laser source in the transmitter must remain within the bandpass, nominally 20 Å, of the dichroic filters used to combine two of the sources at any time. The lasers are also specified to operate predominantly in a single longitudinal mode. Figure 9 shows the time evolution of the spectrum of two CSP lasers designed to operate near 8650 Å. The laser shown in the left portion of the figure has been operating at 35 mW cw in a single longitudinal mode for over 1,000 hours with negligible wavelength drift. The laser is maintained at a constant heat-sink temperature of 25 (±1) °C. Similar results are shown in the right part of the figure for a laser operating at 50 mW 50 % duty-cycle for 700 hours thus far. More complete data is available for shorter wavelength CSP devices, as shown in Figure 10. The spectra of these two lasers show single longitudinal mode operation within the 20 Å bandpass tolerance of the dichroic filters 14,000 hours in both cases. These lifetests are continuing.

Conclusion

Development of these devices is continuing. Particular emphasis is now being placed on understanding the degradation mechanisms of the structure in order to assure high output power performance over the life of the ACTS mission. These investigations should result in a proven source for the DDLT experiment as well as offer improvements which can be applied to CSP lasers operating at shorter wavelengths.

Acknowledgments

The development of CSP lasers has been supported, in part, by NASA's Langley Research Center and Goddard Space Flight Center under contract number NAS1-17441. This work is a collaborative effort on the part of

ORIGINAL PAGE IS
OF POOR QUALITY

the Optoelectronics Research Laboratory at RCA Laboratories, directed by B. Hershenov. The authors particularly thank D. J. Channin and N. W. Carlson for contributing measurements and understanding of systems performance, and J. C. Connolly, L. Elbaum, N. A. Dinkel, D. B. Gilbert, J. J. Hughes, M. G. Harvey, and T. R. Stewart for their technical assistance in fabricating and characterizing the devices. The authors also appreciate the continued support and guidance of M. Ettenberg and R. A. Bartolini.

References

[1]RFP5-90143/237 NASA/Goddard Space Flight Center, Greenbelt, MD, July 15, 1986.

[2]B. Goldstein, M. Ettenberg, N. A. Dinkel, and J. K. Butler, "A high-power channeled-substrate-planar AlGaAs diode laser," *Appl. Phys. Lett.* 47, 655, 1 October, 1985.

[3]N. W. Carlson, V. J. Masin, G. A. Evans, B. Goldstein, and J. K. Butler, "Phase front measurements of high-power diode lasers," CLEO'86, paper TuQ-6, San Francisco, CA, 10 June, 1986.

[4]D. B. Carlin, B. Goldstein, and D. J. Channin, "High-power diode lasers for optical communications applications," MILCOM'85, paper 4.4, Boston, MA, October 20, 1985.

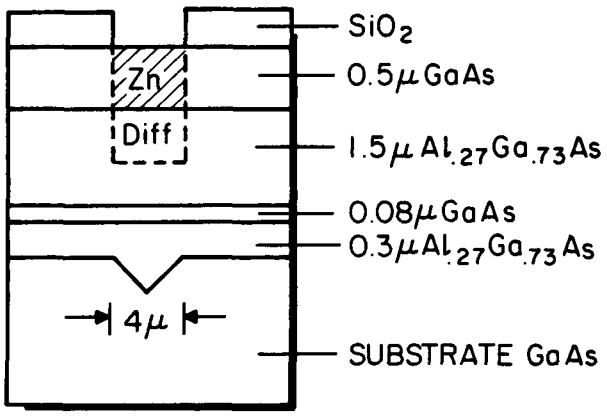

Figure 1. Structure of the CSP diode laser designed for emission at 0.87 μm.

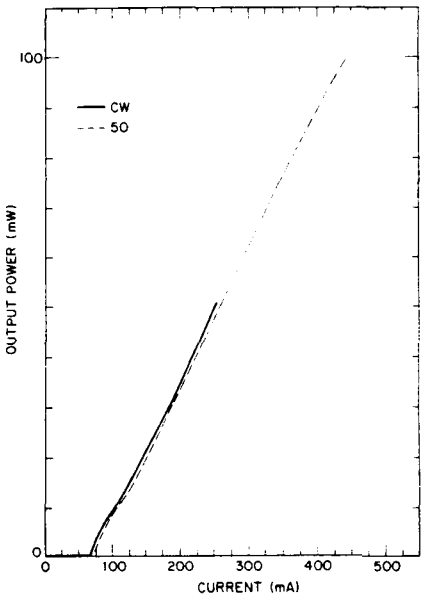

Figure 2. Power-versus-current characteristics of a 0.87 μm CSP.

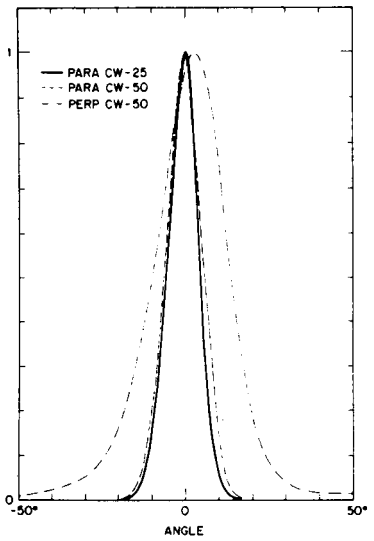

Figure 3. Lateral and transverse far-field intensity profiles at 25 and 50 mW cw.

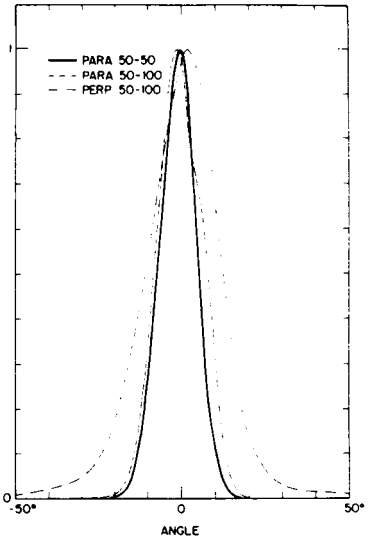

Figure 4. Lateral and transverse far-field intensity profiles at 50 and 100 mW 50% duty cycle.

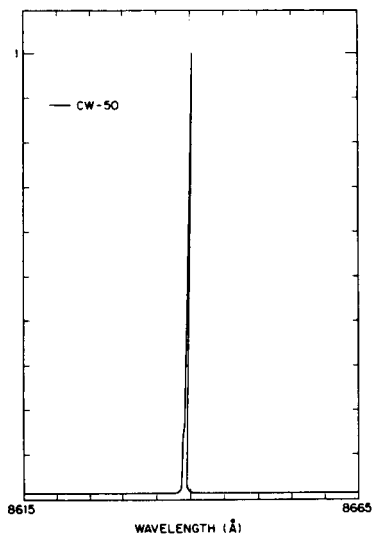

Figure 5. Spectrum of a DDLT CSP diode laser at 50 mW cw.

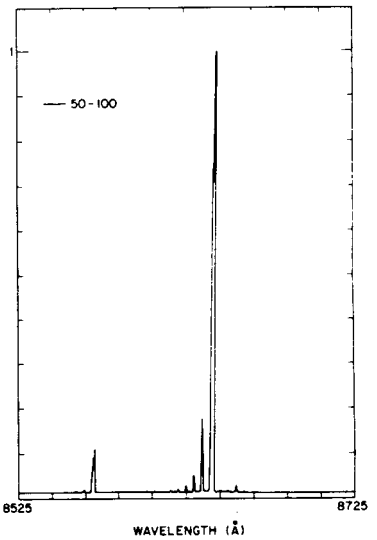

Figure 6. 100 mW 50% duty-cycle spectrum.

ORIGINAL PAGE IS
OF POOR QUALITY

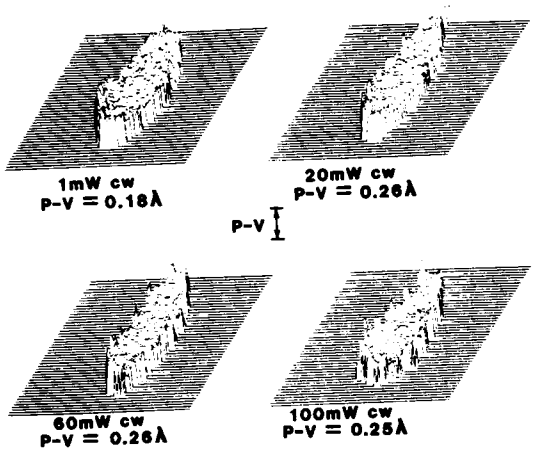

Figure 7. Two-dimensional phase fronts of a collimated CSP far-field.

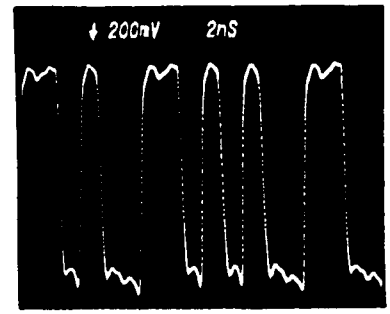

Figure 8. Modulated 500 Mb/s Manchester encoded laser output at 60 mW peak power.

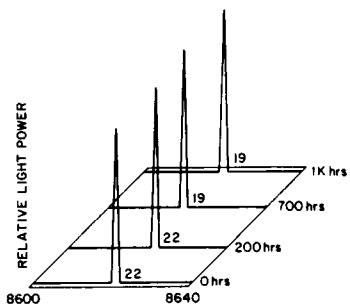

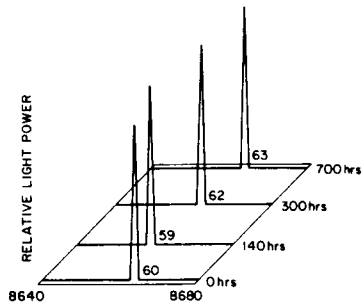

Figure 9. Time evolution of the spectra of two 0.87 μm CSP devices, one operating at 35 mW cw (left) and the other at 50 mW 50% duty-cycle (right) showing single longitudinal mode output.

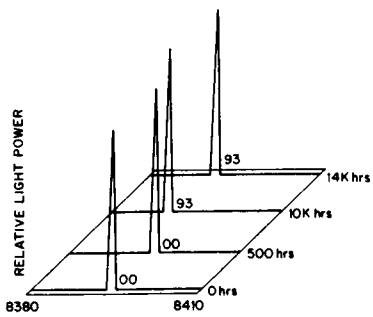

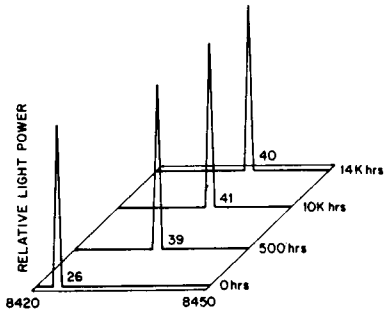

Figure10. Time evolution of the spectral of two "standard" CSP devices, operating near 0.84 μm showing single longitudinal mode behavior to 14,000 hours at 20 mW cw at 30°C.

Appendix D

Reprinted from SPIE Vol. 740—Laser Diode Optics
© 1987 by the Society of Photo-Optical Instrumentation Engineers, Box 10, Bellingham, WA 98227-0010 USA

Phase Front Characterization Of The Outputs Of Diode Lasers

N.W. Carlson, V.J. Masin, and D.B. Carlin

RCA Laboratories
Princeton, NJ 08543-0432

Abstract

The phase front deviations present in the output radiation patterns of a variety of AlGaAs diode lasers has been experimentally determined in order to assess their utility as optical sources in diffraction-limited applications. Experimental interferometric characterizations have shown that the output of index-guided devices have smaller aberrations than do gain-guided laser structures.

Introduction

Diode lasers are becoming the preferred source for many types of diffration-limited optical applications, including optical data storage and free-space communications.[1,2] The efficiency of such optical systems is limited by the losses between the transmitting laser and the detector. Aberrations in the output wavefront of the diode laser may have a significant deleterious effect on system performance, depending on the size and nature of the aberrations and the particular system under consideration. It is, therefore, important to characterize the aberrations of the output wavefront fully in order to predict system performance. In addition, an understanding of the nature of the aberrations present may allow modifications of the laser structure designed to improve output beam quality.

The output radiation from a diode laser in such systems is generally collected and collimated by an appropriately designed optical system. In an ideal case, the phase fronts of the collimated beam are plane waves, resulting in diffraction-limited performance. Aberrations in either the optics or the diode laser output itself will cause deviations from plane waves in the phase fronts of the collimated beam, thereby reducing the peak intensity of the far-field radiation pattern, an important characteristic for many systems (free-space communications in particular). The ratio of the reduced peak intensity of a focussed beam degraded by aberrations to the peak intensity of a focussed beam formed from collimated plane waves is called the Strehl intensity. This intensity, I_p, is given by:

$$I_p = {}^1/_{A^2} \left| \int_A e^{2\pi i \phi(x,y)/\lambda} \, dx \, dy \right|^2 \qquad (1)$$

where $\phi(x,y)$ is the phase aberration at the exit pupil of the collimator measured in units of the wavelength of light, λ, and A is the area of intersection of the wavefront and the collimation aperture. A Strehl intensity ≥ 0.8, corresponding to the $\lambda/4$ Rayleigh criterion for focus aberrations, is usually considered to be acceptable performance for "diffraction-limited" optical systems.[3,4] For relatively small phase aberrations, the above equation can be approximated by:

$$I_p \equiv 1 - [2\pi \Delta\phi_{rms}/\lambda]^2 \qquad (2)$$

where $\Delta\Phi_{rms}$ is the root mean square phase front aberration. The Strehl intensity as a function of rms phase aberration for uniform illumination of the entrance pupil of the system is plotted in Figure 1, over the range for which approximation (2) is valid ($I_p > 0.1$). From the figure it can be seen that a Strehl intensity of 0.8 corresponds to a rms wavefront aberration of $\lambda/14$.

Phase Front Measurement Technique

A LADITE[5,6] computer-controller Mach-Zehnder interferometer, manufactured by the Wyko Corporation, was used to measure the output wavefront from a variety of AlGaAs diode lasers emitting in the 0.81 to 0.87μm regime. This device measures the properties of a collimated beam. The aberrations of the collimation optics must therefore be negligible compared with those of the diode. In fact, the wavefronts of the collimating optics used in these investigations were independently measured to be $\leq \lambda/13$ rms. In addition, a differential measurement technique[7] was employed in which changes in the wavefront as a function of operation conditions is determined. The computer subtracts the phase fronts of the diode laser as measured at two different output powers; the difference represents the power-dependent component of the phase front. The use of this technique can detect changes as small as $\lambda/50$.

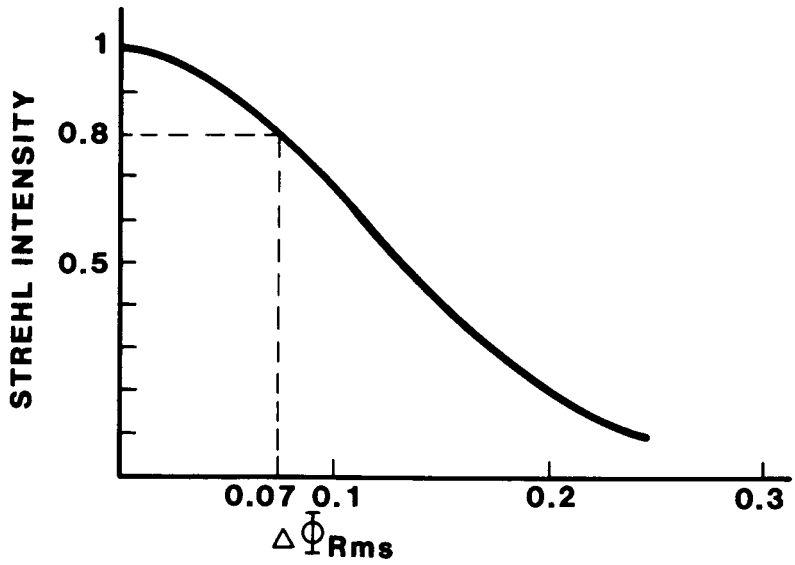

Figure 1. Approximate Strehl intensity as a function of rms phase aberration for uniform illumination.

Diode Laser Phase Fronts

Of the applications currently envisioned, the needs of free-space communications place some of the most formidable requirements on diode laser characteristics and are, therefore, driving the development of the technology. For this application, not only must the device emit extremely high output power (≥100mW) in a stable, single-lobed aberration-free beam, but it must continue to perform reliably for many thousands of hours due to the remote location of the system. In addition, coherent detection schemes under development place the added burden of stable, single longitudinal mode operation over the life of the mission. Several different types of AlGaAs diode laser structures are being developed in order to attain the output characteristics required. Both individual emitters and linear arrays of closely coupled phase-locked lasers are being developed. These emitter structures may confine the lateral spatial mode (parallel to the junction plane) by either the injection current distribution, in gain-guided devices, or by an index of refraction variation built into the laser waveguide, in index-guided structures. Therefore, the output wavefronts from several types of AlGaAs diode lasers were measured in order to assess their utility in diffraction-limited systems.

Figure 2 shows the phase fronts of four types of AlGaAs lasers: a single element index-guided channeled substrate planar (CSP) laser (upper left); a single element gain-guided 5μm-wide contact stripe planar double heterojunction (DH) device (upper right); a four-element index-guided phase-locked array of CSP lasers (lower left); and a ten-element 10μm-wide stripe gain-guided planar DH array (lower right). The collimation of the output beams of the individual emitters was effected by an objective of 0.615 NA. The CSP shows rms wavefront aberrations of $\approx \lambda/40$ whereas the phase front of the gain-guided DH is characterized by aberrations of $\approx \lambda/7$, primarily due to astigmatism. Use of the latter would clearly degrade the performance of a system incorporating diffraction-limited optics. Detailed studies of CSP devices have shown negligible wavefront aberrations at cw output powers up to 100 mW and pulsed operation to 120 mW.[8]

ORIGINAL PAGE IS
OF POOR QUALITY

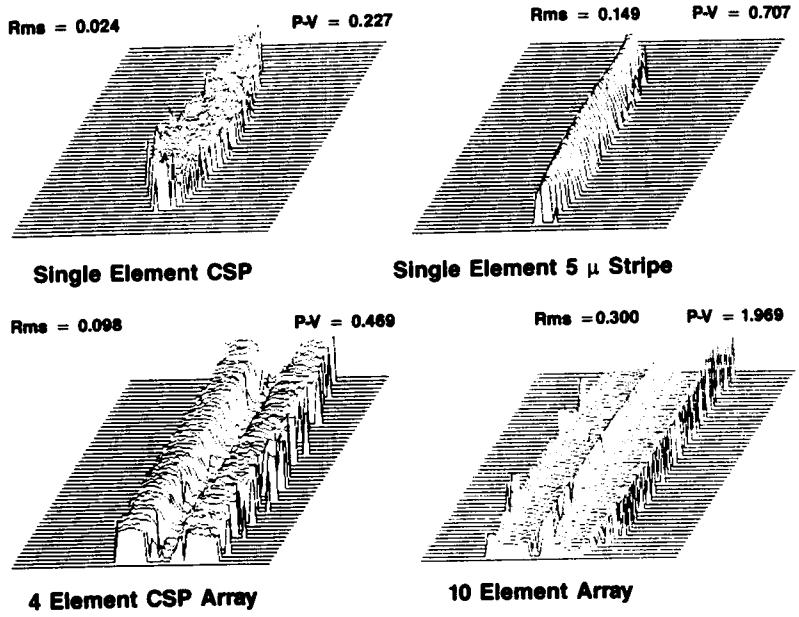

Figure 2. Three-dimensional perspective plots of phase front measurements of four types of AlGaAs diode laser; a single element index-guided CSP (upper left); a single element gain-guided 5μm-wide stripe DH (upper right); a four element dual-lobed output index-guided CSP phase-locked array (lower left); and a ten element gain-guided array of phase-locked DH lasers (lower right). The horizontal axis is in the lateral direction (parallel to the junction plane) of the laser far-field emission. The peak-to-peak and rms deviations of the phase are noted for each case.

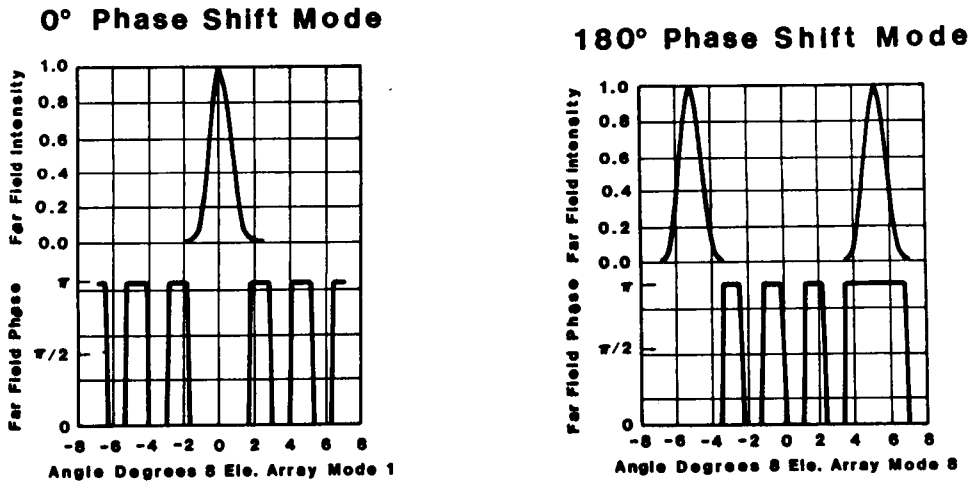

Figure 3. Theoretical far-field intensity (upper curves) and phase (lower curves) distributions of 0° phase-shift, single-lobed array output (left) and 180° phase-shift, double-lobed emission (right).

The phase-locked arrays, shown at the bottom of Figure 2, were collimated using a 0.25NA objective, as it was not possible to obtain good fringe patterns with faster lenses. In addition, the software of the LADITE sometimes has difficulty following abrupt, large phase differences such as are typified by the differences in phase between lobes of many phase-locked arrays. Both devices shown in the figure emitted multiple-lobed far-field patterns. Indeed, forcing phase-locked arrays to emit in a stable, single-lobed pattern is the primary focus of current research in the area.[9] It is clear from the figure that the aberrations of both phase-locked arrays are greater than that of their single element counterparts. Again, however, the index-guided device is substantially better than the gain-guided structure.

Because of the difficulty in evaluating the output of arrays directly with high-quality collimators, a second, indirect approach was taken. The emission from a phase-locked array can be described as the far-field radiation pattern of the individual emitter comprising the building block of the array multiplied by the emission pattern due to the geometrical distribution of emitters within the array.[10] Figure 3 shows theoretical calculations of the 0° phase shift single-lobed far-field mode (mode 1) and the 180° phase shift double-lobed far-field mode (mode 8) emitted by an eight element CSP phase-locked array having 2μm-wide channels separated by 4μm between array elements. The lateral far-field intensity profiles and phase distributions of these modes are shown in the upper and lower parts of the figure, respectively. The phase variation across each lobe of a double-lobed array is expected to be small; the geometrical array phase distribution is a binary function, having values of either 0 or π, and the phase of the CSP emission (full-width at half-maximum typically 8°) varies slowly over the $\approx 1°$ width of the array lobes. Experimentally, the collimated output of an eight element CSP array, emitting twin diffraction-limited lobes, was masked so that only one lobe entered the interferometer. The phase front of this array lobe is shown in Figure 4. Wavefront aberrations are negligible as expected, measuring $\lambda/70$ rms. Thus, each lobe of a strongly coupled out-of-phase array can be used separately as an optical source in diffraction-limited systems. The two separated far-field lobes showed straight, highly contrasting fringes when interfered with each other, a strong indication that the array was emitting predominantly in a single array mode. One might infer that the output of a strongly locked, 0° phase-shift array, if such a device could be made to operate stably, would also be characterized by negligible aberrations.

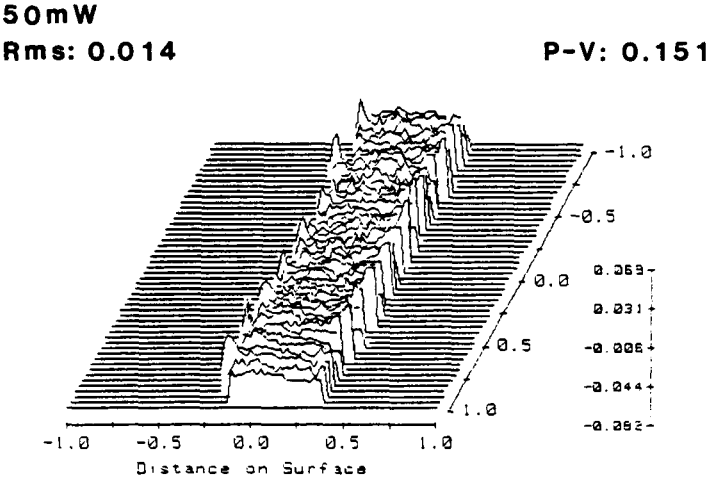

Figure 4. Map of the wavefront of one lobe of a strongly coupled eight element CSP phase-locked array formed by 2μm-wide channels separated by 4μm. Each lobe had a full-width at half-maximum equal to that calculated for an array of these dimensions.

Conclusion

The phase front aberrations present in the outputs of a number of types of AlGaAs diode lasers under a wide range of operating conditions have experimentally determined using a Mach-Zehnder interferometer. In general, we have found that gain-guided devices, both in individual emitter and phase-locked array geometries, are characterized by significantly larger rms phase front deviations and, therefore, lower Strehl intensities, than are their index-guided counterparts.

ORIGINAL PAGE IS
OF POOR QUALITY

Acknowledgments

The authors thank B. Goldstein and N.A. Dinkel for supplying the diode lasers used in this work and C.J. Kaiser and D.B. Gilbert for assistance in characterizing the devices. The authors also are grateful to G.A. Evans, S.L. Palfrey, and D.J. Channin for their thoughtful advice and to R.A. Bartolini and M. Ettenberg for their continued support of this work.

References

1. J.D. Barry, "Design and System Requirements Imposed By The Selection of GaAs/GaAlAs Single Mode Laser Diodes For Free Space Optical Communications," IEEE J. Quantum Electronics, QE-20,478, 1984.
2. G.A. Evans and M. Ettenberg, "Semiconductor Laser Sources for Satellite Communications," in Laser Satellite Communications, ed. M. Katzman, to be published.
3. M. Born and E. Wolf, Principles of Optics, 5th edition, Oxford: Pergammon Press, 1975.
4. W.T. Welford, Aberrations of the Symmetrical Optical Systems, Academic Press, 1974.
5. K.M. Leung and S.R. Lange, "Wavefront Evaluation On Laser Diodes Using a Phase Measurement Interferometer," Proc. SPIE, Vol. 429,27, 1983.
6. J. Hayes and S.R. Lange, "A Heterodyne Interferometer For Testing Laser Diodes," Proc. SPIE, Vol. 429, 22, 1983.
7. N.W. Carlson and V.J. Masin, "Phase Front Measurements of High-Power Diode Lasers For Optical Systems," IEEE J. Quantum Electronics, QE-22, 2079, 1986.
8. D.B. Carlin, G.N. Pultz, and B. Goldstein, "0.87μm CSP Diode Lasers For Spaceborne Communications," to be published Proc. SPIE, Vol. 756, 1987.
9. D. Botez and D.E. Ackley, "Phase-locked Arrays of Semiconductor Diode Lasers," IEEE Circuits and Devices Magazine, 8, January, 1986.
10. N.W. Carlson, J.K. Butler, and V.J. Masin, "Coupled Mode Analysis of Wavefront Properties of Phased Array Diode Lasers, Electronic Letters 22, 1327, 1986.

Appendix E

476 IEEE JOURNAL OF QUANTUM ELECTRONICS, VOL. QE-23, NO. 5, MAY 1987

A Ten-Element Array of Individually Addressable Channeled-Substrate-Planar AlGaAs Diode Lasers

D. B. CARLIN, B. GOLDSTEIN, J. P. BEDNARZ, M. G. HARVEY, AND N. A. DINKEL

Abstract—**A monolithic array of ten individually addressable channeled-substrate-planar diode lasers, each emitting 30 mW CW in a single spatial mode, has been developed with particular application to high data rate multichannel optical recording systems.**

MONOLITHIC arrays of individually addressable high power diode lasers are being developed, specifically as sources for multiple channel, high data rate optical memories. The simultaneous storage of independent data streams on multiple, parallel tracks allows commensurately multiplied transfer rates for both data recording and retrieval, a necessary attribute for some high performance systems. Previous work reported three-channel data storage [1] using an array of CDH-LOC (constricted double heterojunction, large optical cavity) devices [2] focused on an archival recording media. These lasers emitted up to 20 mW CW and 40 mW 50 percent duty cycle in a single spatial mode. The recent emergence of erasable magnetooptic recording media, however, has imposed additional output power demands on the diode lasers used in recording systems. In order to achieve complete erasure in a single pass, the laser must emit continuously at roughly the same power as is normally required in a 50 percent duty cycle pulsed mode of operation for recording. In addition, many applications under consideration require an increased number of contiguous diode lasers in order to achieve data transfer rates of hundreds of Mbits/s. We report the fabrication of arrays of CSP (channeled-substrate-planar) AlGaAs diode lasers with higher CW output power in a single spatial mode as well as improved device-to-device uniformity (compared to the CDH-LOC device) for use in such high performance multichannel optical recording systems.

Individual CSP diode lasers have recently been reported that emit up to 150 mW CW in a single spatial mode [3]. We have incorporated this structure in an array geometry, as shown in the schematic drawing in Fig. 1, which depicts three elements of a multielement array. The arrays are fabricated by standard multibin liquid phase epitaxy techniques as ten-diode units. Light is generated in a thin (≈ 800 Å thick) active layer of undoped $Al_{0.06}Ga_{0.94}As$ sandwiched between cladding layers of p-doped and n-doped $Al_{0.33}GA_{0.67}As$, typically 1.8 and 0.5 μm thick, respectively. The injection current is confined both by a narrow contact stripe in the p-side metallization, defined by openings in an SiO_2 insulation film deposited on the GaAs cap layer, and by the diffusion of a zinc finger partially through the p-cladding layer. The lasers are separated by 150 μm, a distance that is photolithographically defined by the mask pattern used to etch the channels and contact stripes. This distance is a compromise between the desire to pack as many lasers as possible into the field of view of the opitcal recording system and the need to minimize crosstalk between the diode elements. Electrical crosstalk between elements is eliminated by the formation of 50 μm wide channels between the elements. These channels are ion milled through the p-contact metallization (comprised of Ti-Pt-Au) and the active layer of the CSP structure. Each array is 1.95 mm in width and 100 μm in thickness, and is cleaved to have a cavity length of 200 μm and coated to produce 90 percent reflectivity on the back facet and 10 percent reflectivity on the front or emitting facet. The array is attached to a thermoelectrically cooled submount that provides individual electrical contact to each of these lasers while maintaining the device in a suitable mechanical and thermal environment. The p side of the chip is soldered to a metallized electrode pattern deposited on a beryllia substrate.

Fig. 2 shows the optical output power versus input current (P-I) characteristics for a ten-element array with each laser operating to at least 30 mW CW. Threshold currents range from 76 to 92 mA and differential quantum efficiencies are 38-56 percent for the lasers in this array. Fig. 3 shows the lateral far-field intensity profiles for each of the ten lasers at 30 mW CW. These show single-lobed fundamental spatial mode operation, necessary for use in diffraction-limited systems such as are embodied by high performance optical recorders. The full widths at half maximum (FWHM) of the far fields are also reasonably uniform, ranging from 7.8 to 9.5°; FWHM's of the transverse far fields are about 30°. For optical data recording applications, the longitudinal mode spectrum is not particularly critical as the lasers are used as a highly localized source of heat. The operating wavelengths must, however, fall within the wavelength bandwidth of the optics. The CW spectra of each of the ten lasers, operating individually, in this particular array are shown in Fig. 4. The mean output wavelength is 8340 Å. Array elements 1 and 2 are characterized by emission in several Fabry-Perot modes, with primary output wavelengths of 8271 and 8289 Å, respectively. Elements 3-10 each emit predominantly in a single longitudinal mode; these are more closely grouped in wavelength, ranging from 8319 to 8372

Manuscript received September 2, 1986; revised December 19, 1986. This work was supported in part by the NASA Langley Research Center under Contract NAS1-17441.

The authors are with the RCA laboratories, Princeton, NJ 08543.

IEEE Log Number 8613516.

0018-9197/87/0500-0476$01.00 © 1987 IEEE

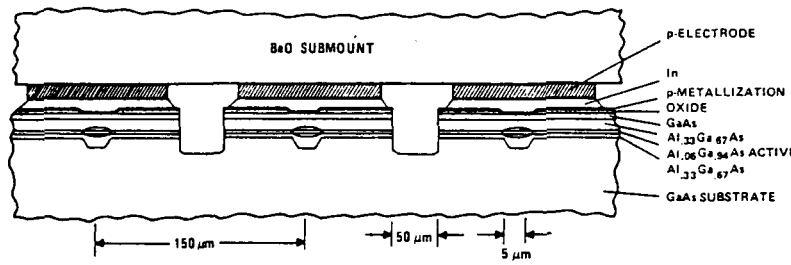

Fig. 1. Schematic drawing of three elements of an individually addressable multidiode CSP array bonded to metallized electrodes on a beryllia submount.

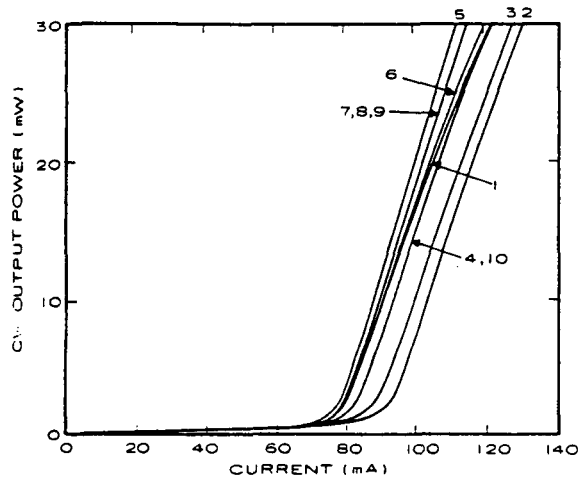

Fig. 2. Power versus current characterisitcs of the lasers in a ten-element array.

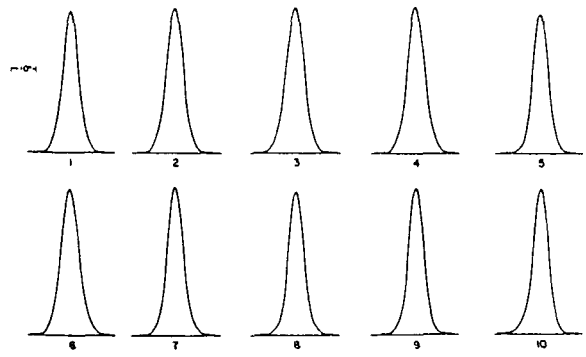

Fig. 3. Lateral far-field intensity profiles of a ten-element array, with each laser operating at 30 mW CW.

Å. The variations in output spectra are probably due both to nonuniform thermal contact between the p side of the chip and the substrate and inhomogeneities in the composition of the LPE grown material. Arrays of this type have been used in prototype optical memories to record, erase, and retrieve multiple, distinctly different channels of data at varied rates up to 39 Mbits/s per channel.

Acknowledgment

The authors acknowledge C. J. Kaiser, J. J. Hughes, W. F. Reichert, and G. A. Alphonse for their technical contribution to this work, D. T. Tarangioli, D. P. Marinelli, J. B. Berkshire, E. DePiano, and D. A. Truxal for their assistance in processing the laser arrays, and R. A. Bartolini, M. Ettenberg, and B. Hershenov for their continued support and guidance of this program.

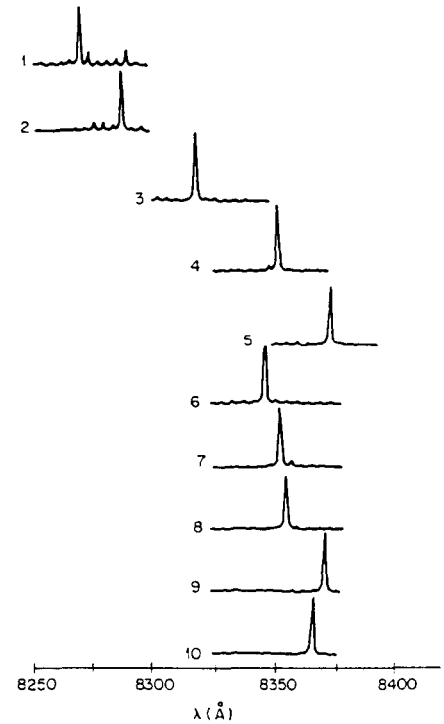

Fig. 4. CW spectra of array elements 1 (top)-10 (bottom).

References

[1] D. B. Carlin, J. P. Bednarz, C. J. Kaiser, J. C. Connolly, and M. G. Harvey, "Multichannel optical recording using monolithic arrays of diode lasers," *Appl. Opt.*, vol. 23, pp. 3994–4000, Nov. 15, 1984; "Erratum," pp. 4613–4619, Dec. 15, 1984.

[2] D. Botez, J. C. Connolly, D. B. Gilbert, M. G. Harvey, and M. Ettenberg, "High-power individually addressable monolithic array of constricted double heterojunction large-optical-cavity lasers," *Appl. Phys. Lett.*, vol. 41, pp. 1040–1042, Dec. 1, 1982.

[3] B. Goldstein, M. Ettenberg, N. A. Dinkel, and J. K. Butler, "A high-power channeled-substrate-planar AlGaAs laser," *Appl. Phys. Lett.*, vol. 47, pp. 655–657, Oct. 1, 1985.

NASA National Aeronautics and Space Administration

Report Documentation Page

1. Report No.	2. Government Accession No.	3. Recipient's Catalog No.
NASA CR-4119		

4. Title and Subtitle

AlGaAs Heterojunction Lasers

5. Report Date

February 1988

6. Performing Organization Code

7. Author(s)

B. Goldstein, G. N. Pultz, D. B. Carlin, S. E. Slavin, and M. Ettenberg

8. Performing Organization Report No.

RCA-PRRL-87-CR-1

10. Work Unit No.

506-44-21-01

9. Performing Organization Name and Address

RCA Laboratories
Princeton, New Jersey 08543-0432

11. Contract or Grant No.

NAS1-17441

13. Type of Report and Period Covered

Contractor Report
(6-28-85 - 6-27-86)

12. Sponsoring Agency Name and Address

National Aeronautics and Space Administration
Washington, DC 20546

14. Sponsoring Agency Code

15. Supplementary Notes

NASA Langley Technical Monitor: H. Hendricks
FINAL REPORT

16. Abstract

The characterization of 8300 Å lasers has been considerably broadened, especially in the area of beam quality. Modulation rates up to 2 Gbit/sec at output powers of 20 mW were observed, waveform fidelity was fully adequate for low BER data transmission, and wavefront measurements showed that phase aberrations were less than $\lambda/50$.

Also, individually addressable arrays of up to ten contiguous diode lasers have been fabricated and tested. Each laser operates at powers up to 30 mW cw in single spatial mode.

Shifting the operating wavelength of our basic CSP laser from 8300 Å to 8650 Å was accomplished chiefly by the addition of Si to the active region. Output power has reached 100 mW single mode, with excellent far-field wave-front properties. Operating life is currently $\sim$1000 hours at 35 mW cw.

In addition, laser reliability, for operation at both 8300 Å and 8650 Å, has profited significantly from several developments in our processing procedures.

17. Key Words (Suggested by Author(s))	18. Distribution Statement
High power diode lasers, semiconductor lasers, phase-locked arrays, nonabsorbing mirrors	Unclassified - Unlimited Subject Category 36

19. Security Classif. (of this report)	20. Security Classif. (of this page)	21. No. of pages	22. Price
Unclassified	Unclassified	486	A21

NASA-Langley, 1988

For sale by the National Technical Information Service, Springfield, Virginia 22161-2171